Photophysics of Biological and Synthetic Multichromophoric Systems

Spectroscopic Investigations of Bacterial Light-Harvesting Complexes and of Carbonyl-Bridged Triarylamine Derivatives

Der Universität Bayreuth
zur Erlangung des Grades eines
Doktors der Naturwissenschaften (Dr. rer. nat.)
vorgelegte Abhandlung

von

Sebastian Reinhardt Beyer

aus

Konradsreuth

1. Gutachter: Prof. Dr. Jürgen Köhler

2. Gutachter: Prof. Dr. G. Matthias Ullmann

Tag der Einreichung: 27. 4. 2015

Tag des Kolloquiums: 16. 7. 2015

»Und was ist es nun, was du zu geben hast? Was ist es, das du gelernt hast, das du kannst?«

»Ich kann denken. Ich kann warten. Ich kann fasten.«

HERMANN HESSE, Siddhartha

» And what is it now what you've got to give? What is it that you've learned, what you're able to do?«

» I can think. I can wait. I can fast.«

Abstract

Multichromophoric systems play a major role in natural photosynthetic processes. They are the basic building blocks for the absorption of light and the subsequent energy transfer within photosynthetic organisms. Optimized by evolutionary selection processes, they constitute an ideal blueprint for artificial, nature-inspired multichromophoric light-harvesting systems. This thesis investigates the energy transfer and the photophysical properties of different multichromophoric systems:

- Reaction centre light-harvesting complex I (RC-LH1), a natural light-harvesting complex from purple bacteria,
- a hybrid system built from a spherical gold nanoparticle (AuNP) and a light-harvesting complex II (LH2), another light-harvesting complex from purple bacteria,
- two novel artificial light-harvesting systems, based on carbonyl-bridged triarylamines (CBTs)

Different methods of optical spectroscopy and optical microscopy have been used to investigate these systems.

The first part of this work discusses the results of time-resolved optical spectroscopy in a picosecond-range on isolated RC-LH1 from *Rhodopseudomonas palustris*. Their fluorescence decay was recorded dependent on the excitation fluence and the repetition rate of the excitation laser. Both parameters were varied over three orders of magnitude. We observed three components in the decays with characteristic decay times of 40, 200 and 600 ps, respectively, that occurred in different amplitude ratios, dependent on the excitation parameters. A first suggestion that the decay times are an indicator of the redox state of the so called “special pair” (P) within the RC could be underpinned by two reference experiments. In those experiments, the redox state of P

was influenced by a reducing agent or an oxidising agent, respectively, by stepwise increasing its concentration while the fluence and the repetition rate stayed fixed. Thus the decay times of 40, 200 and 600 ps could be assigned to different species of RC-LH1 with their special pair in the neutral state P, with the special pair in the reduced state P^+ and with the reaction centre lacking or dysfunctional, respectively. Using these results as well as values from the literature we were able to design a detailed kinetic model of the energy transfer pathways in RC-LH1. The fluorescence decays of RC-LH1 could then be simulated by a global master equation approach based on a microstate description. Due to an excellent agreement between experiment and simulation this model allows to predict the relative populations of the aforementioned species for given excitation parameters as well as to predict the relative population of carotenoid triplet states on the LH1 rings.

In the second part of this work, a fluorescence microscope with single molecule sensitivity was used to show the plasmonic fluorescence enhancement of LH2 from *Rhodobacter sphaeroides* by spherical AuNP. The fluorescence intensities of single LH2 were measured in presence and in absence of AuNP, with the excitation wavelength in resonance and off resonance of the AuNP's plasmon. Using a home-built evaluation algorithm the intensities of more than 4000 single LH2 could be retrieved. From these intensities, extensive distributions that show the relative frequencies of the different intensity values for all the aforementioned excitation conditions could be gained. When excited in resonance with the plasmon of the AuNP, the intensity distribution of the LH2 in presence of AuNPs as a whole shifted to higher intensity values as compared to the case in absence of AuNPs. The mean value of the intensity distribution in presence of the AuNP was about a factor of 2 higher than that of the intensity distribution in absence of the AuNP. When excited off the plasmon resonance, the intensity distributions of LH2 were almost identical in presence as well as in absence of AuNPs. These observations show the plasmonic origin of the fluorescence enhancement of LH2 and point towards a small spatial distance between LH2 and AuNP, which might indicate an adsorption of LH2 to the spherical AuNP. In a

reference experiment a spacer layer of a thickness of 20 nm was introduced between AuNP and LH2. In this configuration, no fluorescence enhancement could be detected even at excitation of LH2 within the plasmon resonance. The result from this reference experiment thus defined a maximum distance between AuNP and LH2 of 20 nm when no spacer layer is present. Model calculations underpinned our observations and gave a direct hint towards an adsorption of LH2 to the AuNPs.

The third part of this work is concerned with the extensive optical characterisation of two novel organic light-harvesting systems. Two derivatives of carbonyl-bridged triarylamines (CBTs) were investigated with absorption spectroscopy, photoluminescence (PL) emission and PL-excitation spectroscopy (all steady-state) as well as time-resolved emission spectroscopy on picosecond timescales. Both compounds consist of a CBT core that is decorated with either three peripheral naphthalimide (NI) molecules or three peripheral 4-(5-hexyl-2,2'-bithiophene)-naphthalimide (NIBT) molecules. These compounds are abbreviated as CBT-NI and CBT-NIBT, respectively. Additionally isolated CBT, NI and NIBT were investigated as reference compounds as well as mixtures of CBT with NI or NIBT, respectively, that were not covalently bound. For all compounds, we recorded the absorption spectra from the near ultraviolet to the near infrared range, the PL emission spectra in dependence of the excitation wavelength – which at the same time gave access to the PL-excitation spectra – as well as the PL quantum yield and the PL lifetime. For the mixtures of the isolated compounds the same parameters were recorded except for the PL quantum yield and the PL lifetime. The data showed that CBT-NI works as an energy funnel. Photoluminescence always occurred from the CBT core, no matter whether the excitation was tuned to the spectral region of the CBT core or the peripheral NI. For CBT-NIBT, the reverse behaviour could be observed. No matter which absorption band was excited, only PL from the NIBT periphery could be observed. In contrast to the concentrator abilities of CBT-NI, CBT-NIBT represents an energy distributor.

In summary this thesis presented three multichromophoric systems that act as examples to **understand** natural light-harvesting systems, to **manipulate** them and to **imitate** them. The experiments on RC-LH1 from *Rhodopseudomonas palustris* allow a deeper understanding of the energy transfer pathways within this system. The model derived from these experiments enables us to make detailed predictions of the photophysical behaviour of RC-LH1 dependent on the excitation parameters. The study on AuNP-LH2 hybrids represents a statistically solid proof-of-principle that shows the plasmonic fluorescence enhancement of single bacterial light-harvesting complexes by well-defined nanostructures. It gives a good example on how natural light-harvesting systems can be manipulated. The imitation and advancement of natural light-harvesting concepts is realised in the study of the two derivatives of CBT. The extensive optical characterisation of these novel compounds shows their potential as building blocks for molecular electronics, organic photovoltaics and as a promising model system for molecular energy transfer.

Zusammenfassung

Multichromophore Systeme spielen eine tragende Rolle in natürlichen Photosyntheseprozessen. Sie sind die Kernbausteine zur Absorption von Licht und dem anschließenden Energietransfer innerhalb photosynthetischer Organismen. Durch evolutionäre Selektionsprozesse optimiert, bilden sie eine ideale Blaupause für künstliche, von der Natur inspirierte multichromophore Lichtsammelsysteme. Die vorliegende Arbeit untersucht den Energietransfer und die photophysikalischen Eigenschaften verschiedener multichromophorer Systeme:

- Reaktionszentrum-Lichtsammelkomplex I (RC-LH1), ein natürlicher Lichtsammelkomplex aus Purpurbakterien,
- ein Hybridsystem bestehend aus einem sphärischen Gold-Nanopartikel (AuNP) und Lichtsammelkomplex II (LH2), ebenfalls ein Lichtsammelkomplex aus Purpurbakterien,
- zwei neuartige künstliche Lichtsammelsysteme, basierend auf Carbonyl-verbrückten Triarylaminen (CBTs).

Zur Untersuchung dieser drei Systeme wurden verschiedene Methoden der optischen Spektroskopie und Mikroskopie verwendet.

Der erste Teil der Arbeit behandelt die Ergebnisse zeitaufgelöster optischer Spektroskopie auf Pikosekunden-Zeitskalen an isolierten RC-LH1 von *Rhodopseudomonas palustris*. Deren Fluoreszenzzerfall wurde in Abhängigkeit von der Anregungsfluenz und der Wiederholrate des anregenden gepulsten Laserlichtes gemessen. Beide Parameter wurden dabei über drei Größenordnungen variiert. In den Zerfällen wurden drei Komponenten beobachtet mit charakteristischen Zerfallszeiten von 40, 200 und 600 ps, die je nach Anregungsparameter in verschiedenen Amplitudenverhältnissen zueinander auftreten. Eine anfängliche Vermutung, die Zerfallszeiten hingen mit dem Redox-Zustand des im RC befindlichen „special pair“

(P) zusammen, konnte mit zwei Referenzexperimenten untermauert werden. In diesen Referenzexperimenten wurde bei jeweils fester Fluenz und Wiederholrate sukzessive die Konzentration eines Reduktions- bzw. Oxidationsmittels erhöht und so der Redox-Zustand von P beeinflusst. Es ergab sich daraus die Zuordnung der Zerfallszeiten von 40, 200 und 600 ps zu verschiedenen Spezies von RC-LH1 mit neutralem special pair P, mit dem special pair im reduziertem Zustand P^+ und mit fehlendem oder dysfunktionalem Reaktionszentrum. Aus diesen Ergebnissen und verfügbaren Literaturwerten wurde ein detailliertes kinetisches Modell der Energietransferwege in RC-LH1 entworfen. Über einen globalen Mastergleichungs-Ansatz basierend auf einer Mikrozustandsbeschreibung wurden die Fluoreszenzzerfälle von RC-LH1 simuliert. Dank einer hervorragenden Übereinstimmung von Experiment und Simulation erlaubt dieses Modell, Vorhersagen sowohl über die relative Population der drei oben genannten Spezies bei gegebenen Anregungsparametern zu treffen, als auch die relative Population an Carotenoid-Triplettzuständen auf den LH1-Ringen zu bestimmen.

Im zweiten Teil der Arbeit wurde ein Fluoreszenzmikroskop mit Einzelmolekülsensitivität eingesetzt um die plasmonische Fluoreszenzverstärkung von LH2 der Spezies *Rhodobacter sphaeroides* durch sphärische AuNP nachzuweisen. Die Fluoreszenzintensitäten einzelner LH2 wurden dazu in An- als auch in Abwesenheit von AuNP gemessen und dies jeweils bei einer Anregungswellenlänge innerhalb und außerhalb der Plasmonresonanz der AuNP. Durch die Anwendung eines selbst entwickelten automatisierten Auswertungsalgorithmus konnten die Intensitäten von mehr als 4000 einzelnen LH2 aufgenommen werden und daraus umfangreiche Verteilungen, welche die relativen Häufigkeiten der verschiedenen Intensitätswerte zeigen, für all die oben genannten Anregungsbedingungen gewonnen werden. Bei Anregung der LH2 in Resonanz mit der Plasmonschwingung konnte eine Verschiebung der gesamten Intensitätsverteilung hin zu höheren Werten beobachtet werden wenn AuNP anwesend waren, bezogen auf die Intensitätsverteilung bei Abwesenheit der AuNP. Der Mittelwert der Intensitätsverteilung bei Anwesenheit der AuNP lag um Faktor 2 höher als der Mittelwert der Intensitätsverteilung bei Abwesenheit der AuNP.

Bei Anregung der LH2 außerhalb der Plasmonresonanz waren die Intensitätsverteilungen bei An- und Abwesenheit der AuNP nahezu identisch. Diese Beobachtungen zeigen den plasmonischen Ursprung der Fluoreszenzverstärkung von LH2 und deuten außerdem auf eine geringe räumliche Distanz zwischen LH2 und AuNP hin, möglicherweise auch auf eine Adsorption der LH2 an die sphärischen AuNP. In einem Referenzexperiment wurde darum eine 20 nm dicke Abstandsschicht zwischen AuNP und LH2 eingebracht. In dieser Konfiguration konnte auch bei Anregung der LH2 innerhalb der Plasmonresonanz keine Fluoreszenzverstärkung mehr beobachtet werden. Der maximale Abstand zwischen AuNP und LH2 ohne Abstandsschicht konnte so zu 20 nm bestimmt werden. Modellrechnungen untermauerten die Beobachtungen aus den Experimenten und lieferten einen direkten Hinweis auf eine Adsorption der LH2 an die AuNP.

Der dritte Teil der Arbeit befasst sich mit der umfangreichen optischen Erstcharakterisierung zweier neuartiger organischer Lichtsammelsysteme. Zwei Derivate von Carbonyl-verbrückten Triarylaminen (CBTs) wurden mit Methoden der steady-state Absorptions-, Emissions- und Photolumineszenz (PL)-Anregungsspektroskopie sowie zeitaufgelöster optischer Emissions-Spektroskopie auf Pikosekunden-Zeitskalen untersucht. Bei den beiden Verbindungen handelt es sich jeweils um einen CBT-Kern der entweder mit drei peripheren Naphthalimid (NI)-Einheiten oder drei peripheren 4-(5-hexyl-2,2’-bithiophen)-naphthalimid (NIBT)-Einheiten bestückt ist. Die beiden Verbindungen werden als CBT-NI, beziehungsweise CBT-NIBT bezeichnet. Als Referenzverbindungen wurden zusätzlich isolierte CBT, NI und NIBT untersucht, sowie Mischungen aus CBT und nicht kovalent-angebundenen NI, beziehungsweise NIBT. Für alle Verbindungen wurden die Absorptionsspektren vom nahen ultravioletten bis in den nahen infraroten Spektralbereich, die Emissionsspektren in Abhängigkeit von der Anregungswellenlänge – und somit simultan die PL-Anregungsspektren – sowie die PL-Quantenausbeute und die PL-Lebenszeit bestimmt. Für die Mischungen der isolierten Verbindungen wurden die gleichen Parameter bestimmt, mit Ausnahme der PL-Quantenausbeute und der PL-

Lebenszeit. Aufgrund der Datenlage aus den oben genannten Experimenten konnte für CBT-NI das Verhalten eines Energietrichters nachgewiesen werden. Ganz gleich, ob eine Anregung in den Spektralbereich des CBT-Kerns oder der peripheren NI erfolgte, konnte ausschließlich PL aus dem CBT-Kern beobachtet werden. Für das Verhalten von CBT-NIBT ergab sich der umgekehrte Fall. Egal in welcher Absorptionsbande die Anregung erfolgte, konnte nur Emission aus der NIBT-Peripherie nachgewiesen werden. Im Gegensatz zu den Konzentrator-Eigenschaften von CBT-NI, stellt CBT-NIBT somit einen Energie-Distributor dar.

In dieser Arbeit wurden drei multichromophore Systeme vorgestellt, die Beispiele darstellen natürliche Lichtsammelsysteme zu verstehen, sie zu manipulieren und sie zu imitieren. Die Untersuchungen an RC-LH1 von *Rhodopseudomonas palustris* ermöglichen ein tiefergehendes Verständnis der Energietransferwege innerhalb des Systems. Darüber hinaus können mit dem aus den Experimenten abgeleiteten Modell detaillierte Vorhersagen des photophysikalischen Verhaltens von RC-LH1 in Abhängigkeit der Anregungsparameter getroffen werden. Die Studie an AuNP-LH2 Hybriden stellt einen statistisch belastbaren Proof-of-Principle dar, der die plasmonische Fluoreszenzverstärkung einzelner bakterieller Lichtsammelkomplexe durch wohldefinierte Nanostrukturen belegt und gibt ein gutes Beispiel wie natürliche Systeme manipuliert werden können. Die Imitation und Weiterentwicklung natürlicher Lichtsammelkonzepte sind in den beiden Derivaten von CBT realisiert. Die umfangreiche optische Charakterisierung dieser neuartigen Verbindungen zeigt ihr Potential als Bausteine für die molekulare Elektronik, die organische Photovoltaik und als vielversprechendes Modellsystem für molekularen Energietransfer.

Contents

1. Introduction

Every day, the equivalent of 9300 EWh (1 EWh $= 10^{18}$ Wh) reaches the surface of the earth in the form of solar radiation [1]. In comparison, the estimated worldwide consumption of primary energy lies at about 0.15 EWh for the whole year of 2013 [2]. If we were able to harvest all of the incoming solar energy over the whole surface of the earth, it would take us about 1 hour and 24 minutes to satisfy mankind's need for energy for complete 2013. As this scenario is far from reality, it might also be sufficient to completely cover an area of the size of Bavaria and Austria with commercially available solar cells[1].

These two provocative order of magnitude calculations nicely illustrate the importance of solar energy in the future mix of renewable energy sources. Its strong influence is also reflected in the nearly exponential growth, the global photovoltaics market has seen over the last 10 years, when considering the annually installed capacities measured in electrical power output [3].

One of the main problems of photovoltaic energy conversion, which also becomes apparent in the calculations above, is its high consumption of space. Conceptual studies and, in part, recent application consider the integration of photovoltaic systems into buildings to avoid the use of valuable farming land. Thus, in the long term, the only way to keep photovoltaics competitive is to increase the light harvesting efficiency of the solar cells and to reduce the surface area needed for their operation. Recent polycrystalline single-junction silicon solar cells feature efficiencies over 20% [4], which is already close to the maximum theoretical value of about 31%, as predicted by Shockley and Queisser [5]. Novel concepts like dye sensitized or perovskite based solar cells [6,7] or concentrated photovoltaics in combination with multi-junction solar cells

[1] Assuming a flux of solar radiation of about 500 W/m^2, collected at an efficiency of 20% over a total area of 154000 km^2.

show promising results in bypassing the Shockley-Queisser limit, but are still far from broad commercial application. To make sure, that the development of photovoltaics can keep the pace of the last ten to fifteen years, it is of crucial importance to not only evolve those 'next generation' solar cells but to maintain a constant effort in understanding the fundamental processes that drive solar energy conversion.

To that end we are well advised to make use of the efforts nature undertook to evolve photosynthetic concepts. If we were able to fully understand the mechanisms of the photosynthetic apparatus of bacteria, algae or plants, we could exploit them to develop a future generation of photovoltaic devices. This work presents three individual experimental approaches to **understand** natural photosynthetic concepts, to **modify** them and to **imitate** them by the design of a novel multichromophoric light-harvesting system. All three approaches use different methods of optical spectroscopy to investigate the electronic properties of multichromophoric systems and to reveal their energy transfer characteristics:

- Time-resolved fluorescence spectroscopy on the picosecond range is a powerful tool to study the energy transfer dynamics in multichromophoric systems. It can be used to unravel the complex interplay between the light-harvesting I ring (LH1) and the reaction centre (RC), which together constitute the RC-LH1 (or core) complex. RC-LH1 is a membrane protein and represents one of the main building blocks of the photosynthetic membrane of purple bacteria. Understanding how the LH1 ring and the RC interact in isolated core complexes might enable us to draw conclusions on the function of whole patches of photosynthetic membranes and subsequently on the complete photosynthetic apparatus of purple bacteria.

- Single molecule microscopy is an ideal tool to gather information on a system without the drawbacks of ensemble averaging. This work will discuss a high-throughput variant of single molecule microscopy that was used to study hybrid nanostructures composed of spherical gold nanoparticles (AuNPs) and light-

harvesting complex II (LH2), which is a photosynthetic membrane protein from purple bacteria. This technique allows to show the plasmonic fluorescence enhancement of LH2 by the AuNPs and to draw conclusions beyond the mere proof-of-principle that would have been obscured when investigated with an ensemble technique. The results from this study open the way for a systematic and more complex tuning of LH2 fluorescence by plasmonic nanostructures.

- To characterise the electronic properties and energy transfer capabilities of entirely new multichromophoric systems, a combination of spectroscopic techniques is suited best. Using steady-state absorption spectroscopy, photoluminescence (PL) emission and PL excitation spectroscopy as well as time-resolved PL emission spectroscopy on a picosecond timescale, a broad overview over the properties of a multichromophoric system can be gained. The compounds investigated in this work are two novel light-harvesting systems inspired by nature. They both consist of a carbonyl-bridged triarylamine (CBT) core that is either decorated with three naphthalimide (NI) molecules or with three naphthalimide-bithiophene (NIBT) molecules in its periphery. To achieve a concise understanding of these compounds, their isolated building blocks, CBT, NI and NIBT, respectively, were included in the investigation as reference compounds. The results from this study show both light-harvesting systems to be promising candidates for the use in organic photovoltaics or as building blocks for molecular electronics.

This work is organised as follows: In Chapter 2, a short overview will be given over all three systems under investigation and the theoretical background on energy transfer in multichromophoric systems as well as on plasmon-emitter interaction will be discussed. In Chapter 3 the experimental techniques and setups used in the different studies will be summarized. The energy transfer dynamics of RC-LH1 from *Rhodopseudomonas palustris* will be the subject of Chapter 4. Picosecond optical spectroscopy was used to access the fluorescence response of isolated RC-LH1 within a wide parameter range. In

Chapter 5 hybrid nanostructures composed of spherical gold nanoparticles and LH2 complexes from *Rhodobacter sphaeroides* will be investigated by means of high throughput single molecule spectroscopy. Chapter 6 deals with a novel class of artificial light-harvesting molecules. They are composed of a carbonyl-bridged triarylamine core that carries either naphthalimide molecules or naphthalimide-bithiophene molecules in its periphery. The extensive basic spectroscopic characterization of both novel compounds as well as three corresponding reference compounds will be discussed.

2. Energy Transfer in Multichromophoric Systems

This chapter gives a brief overview of the multichromophoric systems under investigation in Chapters 4-6. It will discuss the theoretical background on electronic excitations and energy transfer in multichromophoric systems, as well as the background on plasmon-induced fluorescence enhancement.

2.1. Natural and Artificial Light-Harvesters

2.1.1. Reaction Centre Light-Harvesting Complex 1

Nature has found countless ways to make use of the solar radiation reaching the surface of the earth. Almost all forms of life we know eventually depend on the intake of solar energy and its subsequent conversion to stable chemical equivalents. This gives rise to the question, how we can use this concept for the benefit of mankind and still our species' ever growing hunger for energy. Thus, a great effort in biological research has always been to understand how plants and bacteria realize this process in photosynthesis [8].

One class of bacteria that has been under close investigation since the early days of photosynthesis research are purple nonsulfur bacteria. These organisms evolved a variant of photosynthesis that is, unlike that of plants, anoxygenic [9], *i.e.* these organisms do not oxidise water to molecular oxygen. The natural light-harvesting system discussed in Chapter 4 is one building block of the photosynthetic apparatus of these bacteria. It is a membrane protein called reaction centre light-harvesting complex 1 (RC-LH1) [10]. It functions as an antenna for light that converts absorbed photons into molecular excitations and uses the latter to drive a charge separation, which in turn powers the further elements of the photosynthetic apparatus [11]. A sketch of RC-LH1 is given in Figure 2.1b.

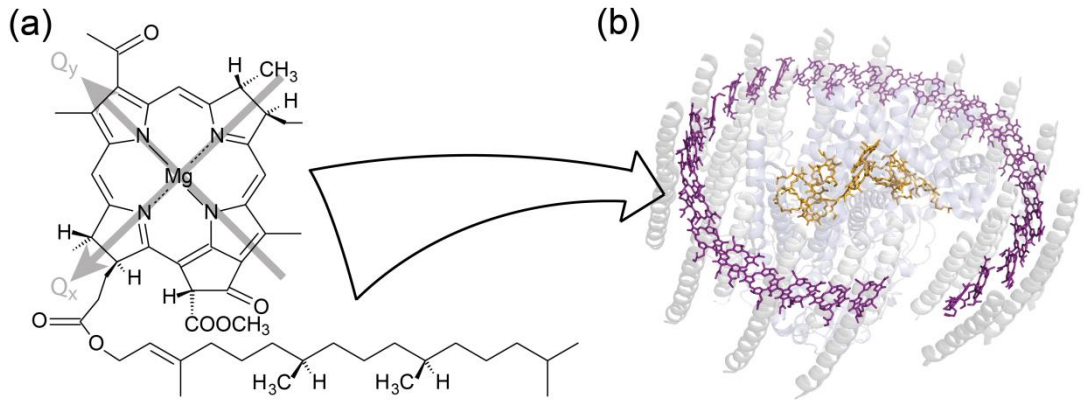

Figure 2.1: a) Structure of bacteriochlorophyll *a* (BChl *a*) according to [8]. The main transition dipole moments (Q_x, Q_y) are indicated as grey arrows. For further details see section 4.1.3. b) Sketch of the RC-LH1 complex from *Rhodopseudomonas palustris*. The BChl *a* molecules of the LH1 complex are depicted in purple while BChl *a* and bacteriopheophytin molecules of the RC are held in orange. The α- and β-helices as well as the protein shell of the RC are given in transparent light and dark grey as well as transparent blue, respectively, to allow a view on the pigments. The structure was redrawn from PDB entry 1PYH [12].

Briefly, RC-LH1 can be separated into the light-harvesting complex 1 (LH1) that serves as the antenna, and the reaction centre (RC), which serves as a transducer and facilitates charge separation. Both subunits consist of a shell of polypeptides that are the housing for multiple pigments, each. The arrangement of those pigment molecules inside the shell defines their functionality. While LH1 relies solely on bacteriochlorophyll *a* (BChl *a*, see Figure 2.1a) and a small number of carotenoid (Car) molecules to install a highly efficient energy transfer system, the RC uses a mix of BChl *a*, bacteriopheophytin (BPhe), ubiquinone (Q) and Car molecules to realize a charge separating system [13]. Both protein subunits and their detailed function will be discussed in Chapter 4. Understanding the structure-function relationship in RC-LH1 on the one hand, and its resulting concept of evolutionary optimized energy transfer on the other, holds great promise for future manmade applications. Our pursuit of novel light-harvesting techniques will greatly benefit, if we agree to **learn from Nature** and adapt concepts that have proven successful in natural selection.

2.1.2. AuNP-LH2 Hybrid Nanostructures

The second system, which will be discussed in Chapter 5, in part also derives from the photosynthetic apparatus of purple bacteria. Light-harvesting complex 2 (LH2) is a membrane protein found in the photosynthetic apparatus of purple bacteria, just as RC-LH1. The structure of LH2 is conceptually very similar to the LH1 complex, but it serves exclusively as an antenna and lacks the RC subunit [11,14]. LH2 has a ring-like shell of polypeptides that houses two different pools of circularly arranged BChl *a* molecules, which are sketched in Figure 2.2a.

The first pool consists of a set of widely spaced and weakly coupled BChl *a* (Figure 2.2, orange), whereas the second pool of pigments consists of a set of closely spaced BChl *a* molecules (Figure 2.2, purple) that form an excitonically coupled system. Embedded into the protein matrix we also find Car molecules (Figure 2.2, green) that absorb light in the green spectral region and which are in close contact to both BChl *a*

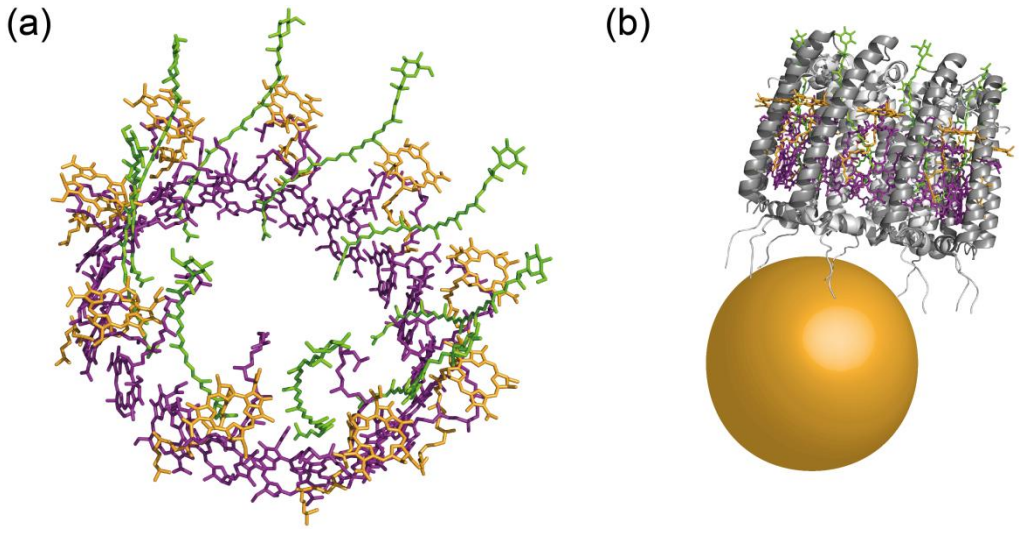

Figure 2.2: a) Pigment pools of the LH2 complex from *Rhodopseudomonas (Rps.) acidophila*. The BChl *a* of the strongly coupled pigment pool are shown in purple, while those of the weakly coupled pool are shown in orange. Car molecules are depicted in green. The protein shell of LH2 was omitted for reasons of clarity. b) LH2 complex from *Rps. acidophila* interacting with a spherical gold nanoparticle, thus forming an AuNP-LH2 hybrid nano structure. Structures of LH2 were redrawn from PDB entry 1NKZ [14].

pigment pools. The whole LH2 complex serves as an energy funnel. Photons absorbed by any of the three pigment pools' absorption bands are converted into molecular excitons and are transferred to the lowest lying exciton state of the highly coupled BChl *a* pool on a picosecond timescale with a quantum efficiency that can be close to 1, depending on the respective bacterial species [8,15]. Despite this high internal quantum efficiency, the drawback of LH2 is its comparatively low absorption cross section. This complicates single molecule optical spectroscopy in particular and gives rise to the question: Can we improve the absorption cross section of LH2?

One possibility to increase the absorption cross section of LH2 is to exploit plasmonic effects, that can be monitored by fluorescence enhancement [16,17]. Nanometre scaled metal structures are known to feature plasmons. These collective oscillations of the metal's electrons can be excited by the absorption of photons. Under certain conditions the plasmon's energy can be transferred to a close lying chromophore and enhance its absorption [18,19]. In Chapter 5 a hybrid nanostructure will be discussed[2], where a spherical gold nanoparticle (AuNP) is used to enhance the absorption of a LH2 complex (see Figure 2.2b). This gives an example of how man can **manipulate Nature** to tailor evolutionary proven concepts to his needs.

2.1.3. Derivatives of Carbonyl Bridged Triarylamine

Two entirely artificial light-harvesting systems will be studied in Chapter 6. They are both based on a carbonyl bridged triarylamine (CBT) core, a flat and triangular molecule (see Figure 2.3, enclosed by the green background) [21]. For both systems under investigation, the CBT core has been decorated with three identical chromophores that are covalently bound to the "corners" of the triangular core. The first system uses naphthalimide (NI) molecules in its periphery and is abbreviated as CBT-NI, its structure is shown in Figure 2.3a. The second system has three 4-(5-hexyl-2,2'-bithiophene)-naphthalimide (naphthalimide-bithiophene, NIBT) molecules in its

[2] A part of the experiments presented in Chapter 5 has already been published elsewhere [20] and is only repeated for reasons of clarity. For a detailed description about which sections and figures are considered part of this thesis and which are not please refer to the beginning of Chapter 5.

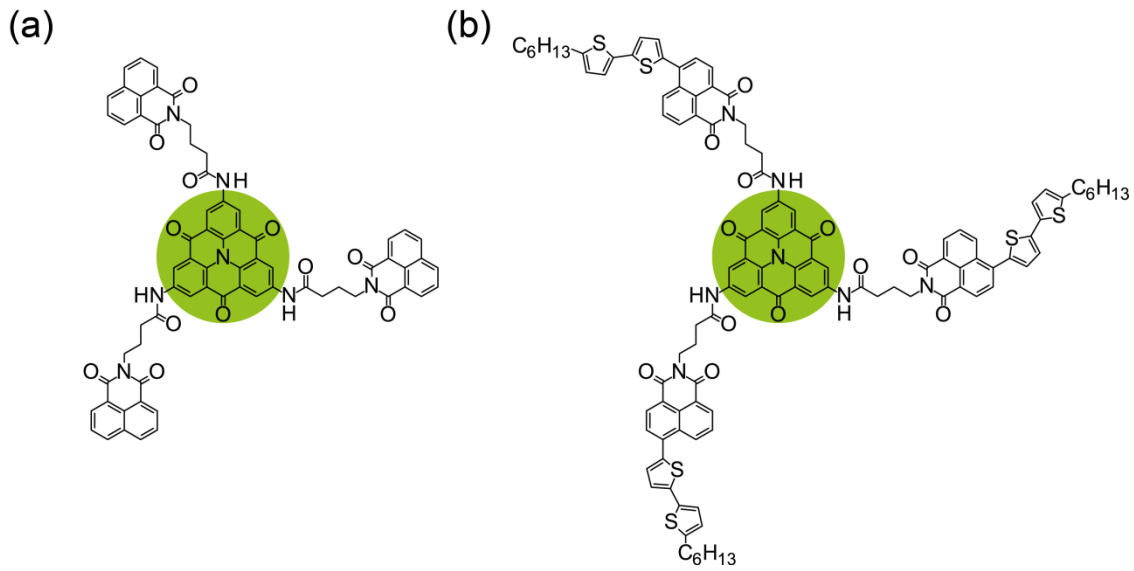

Figure 2.3: Structure of carbonyl bridged triarylamine (green background) with peripheral naphthalimide units (a) as well as peripheral naphthalimide-bithiophene units (b).

periphery and will be referred to as CBT-NIBT (see Figure 2.3b). In CBT-NI, energy absorbed by the periphery is transferred to the CBT core, which effectively increases the absorption cross section of the core and expands the spectral range of its absorption. In contrast to CBT-NI, the energy transfer pathway is reversed in CBT-NIBT. In this molecule, the energy absorbed by the core is distributed to the periphery. This might enable an increased interaction with the surrounding matrix, making CBT-NIBT a possible material for organic photovoltaics. Another promising attribute of both compounds is their tendency to self-aggregation [22–24]. Mediated by a stacking of the planar core molecules [21], CBT-NIBT is able to form monofilaments with a length up to the order of micrometres, which are, at room temperature, able to transfer energy across the full length of the filament [25]. These two artificial compounds will be discussed in detail in Chapter 6 as an example on how manmade structures can **imitate Nature** and which efforts man can undergo to improve on Nature's concepts.

The motif that is common in all three systems described above is their multichromophoric character. They all function via the interaction of organic chromophores (in the case of the AuNP-LH2 hybrid this is expanded by the interaction

with a metal) and show pronounced energy transfer characteristics. Therefore the following sections will give an overview of the concepts of molecular energy transfer and on plasmon-emitter interaction.

The method of choice for the experimental investigation of energy transfer is optical spectroscopy. An overview of the experimental setups and techniques used in this work will be given later in Chapter 3.

2.2. Electronic Excitations in Multichromophoric Systems

An organic chromophore usually shows a multitude of excited singlet, triplet and vibrational states [26] that form a complex framework and make an exact theoretical description rather laborious. In most cases, though, the excited chromophore relaxes into the pure first excited singlet state, from where the deexcitation into the ground state occurs [27]. It is therefore practical to ignore most of the excited states and treat the chromophore as a two-level system that consists of a ground and an excited state. In the following, we will present the mathematical treatment to describe multiple coupled two-level systems [11,28]. This model is suitable to describe the functional mechanisms of the systems discussed in Chapters 4-6.

Let us consider a system of two-level systems $1, 2, 3, \dots, N$. The wave function $|n\rangle$ denotes the situation where the systems do not interact with each other and the *n*-th system is in the excited state while all others are in their ground state. The eigenvalues of the uncoupled two-level systems are given by the energies $E_1 \approx E_2 \approx E_3 \approx \cdots \approx E_N$, with the common average $E_0 = N^{-1} \sum_{n=1}^{N} E_n$. If we now introduce a coupling between the N two-level systems that is small with respect to E_0, the Hamiltonian for the overall system can then be written as [11]

$$\widehat{H} = \sum_{n=1}^{N} (E_0 + \Delta E_n)|n\rangle\langle n| + \frac{1}{2}\sum_{n=1}^{N}\sum_{m\neq n} V_{nm}|n\rangle\langle m|. \qquad 2.1$$

In this notation, we considered the differences in the eigenvalues of the individual systems by a deviation ΔE_n from their common average E_0. This accounts for

differences in the environments of the respective individual systems, which affect their site energies. Commonly this type of disorder is referred to as diagonal disorder. The interaction between two systems n and m is given as $V_{nm}|n\rangle\langle m|$. The values of V_{nm} depend crucially on the geometry of the complete system, as well as the pairwise coupling parameters of the two-level systems. The Hamiltonian as written above does not yet put any constraint on these parameters. As we chose the interaction to be small with respect to E_0, we can use perturbation theory to obtain the new eigenfunctions and eigenvalues of the Hamiltonian described in 2.1.

As a consequence of the coupling, the wave functions $|n\rangle$ are no eigenfunctions of the Hamiltonian $\widehat{H}$. In a system with the above mentioned constraints and where the conditions of the ideal system ($V_{nm} = 0$ for all combinations of n and m) are lifted, the true eigenstates $|e\rangle$ can instead be described as linear combinations of the ideal $|n\rangle$ states:

$$|e\rangle = \sum_n a_n|n\rangle \qquad \text{with } \sum_n|a_n|^2 = 1. \tag{2.2}$$

The coefficients a_n are complex numbers and their square of the absolute value $|a_n|^2$ gives a measure on how strongly the individual $|n\rangle$ states contribute to the eigenstate $|e\rangle$. In an ideal coupled system, where $\Delta E_n = 0$ for all n, $V_{nm} = V_0$ for all combinations of n and m that denote nearest neighbours, $V_{nm} = V_1$ for all combinations of n and m that denote next-nearest neighbours and which fulfils periodic boundary conditions, the new eigenstates of the system can be written as [28]

$$|k\rangle = \frac{1}{\sqrt{N}}\sum_{n=1}^{N} e^{i2\pi k\frac{n}{N}}\,|n\rangle. \tag{2.3}$$

These $|k\rangle$ states are fully delocalized over all N two-level systems and are referred to as Frenkel excitons in molecular physics [11]. In general, the requirements for the ideal system mentioned above cannot be fulfilled and whether the true eigenfunctions $|e\rangle$ are more likely to have the character of $|k\rangle$ states or that of $|n\rangle$ states, depends on the ratio $|V/\Delta E|$ with V and ΔE being the average values of all V_{nm} or ΔE_n, respectively. In the

case, where $|V/\Delta E| \ll 1$, we speak of the weak coupling limit and the true eigenstates are best described as linear combinations of the $|n\rangle$ states as discussed in equation 2.2. This corresponds to an excitation, that is localized on a single two-level system and migration between the individual two-level systems is incoherent and best described by a hopping process. In the opposite limiting case, where $|V/\Delta E| \gg 1$, we speak of the strong coupling limit and the true eigenstates are easier described as linear combinations of the $|k\rangle$ states:

$$|e\rangle = \sum_k b_k |k\rangle \qquad \text{with } \sum_k |b_k|^2 = 1. \tag{2.4}$$

The coefficients b_k are analogous to the a_n coefficients from equation 2.2. In the strong coupling regime, the excitations are delocalized over multiple two-level systems and can migrate between them in a coherent, wave-like manner. The intermediate case, where $|V/\Delta E| \approx 1$ is sometimes termed as partially coherent excitation energy transfer [29]. If we wanted to place the often used Förster approximation inside this framework, it would be situated in a regime that shows an even weaker coupling than the "weak" $|V/\Delta E| \ll 1$ limit [27].

Alongside the new eigenstates, we will also find new eigenvalues for the coupled system, which corresponds to a shift of the energy levels of the individual systems. In the limit of strong coupling, this results in an exciton band structure. Its exact shape depends on the geometry of the system and the type of coupling V_{nm}. As an example, in a linear chain of equivalent two-level systems ($\Delta E_n = 0$ for all n), where only nearest neighbour interactions are taken into account ($V_{nm} = V$ for all combinations of neighbouring n, m), the energies $\epsilon(k)$ of the exciton states follow the relation

$$\epsilon(k) = E_0 + 2V \cos\left(k \frac{2\pi}{N}\right). \tag{2.5}$$

Strongly coupled systems that can be discussed in terms of the description given above, can be found for example in the B875 band of LH1 as discussed in Chapter 4 or in the B850 band of LH2 that will be discussed in Chapter 5.

2.3. Energy Transfer in Multichromophoric Systems

As we saw in the previous section, energy transfer in multichromophoric systems can either occur coherently, incoherently or partially coherent. As coherent energy transfer usually takes place on timescales that are beyond the time resolution of the experiments discussed later on, we will limit the following discussion to the case of incoherent energy migration.

Let us consider a donor molecule D with an excited state that can decay into a continuum of states (for example the vibronic states of the S_0 ground state) as well as an acceptor molecule A in the ground state that can be excited into a continuum of states (see sketch in Figure 2.4). These molecules shall be coupled by an interaction V. As long as the assumptions hold true, that intra molecular relaxation processes are fast compared to the energy transfer between D and A, and that V is weak with respect to the difference in the excited state energies of D and A, the problem can again be treated with perturbation theory. This eventually leads to the application of Fermi's Golden Rule. The rate of energy transfer k_{DA} can then be written as [29]

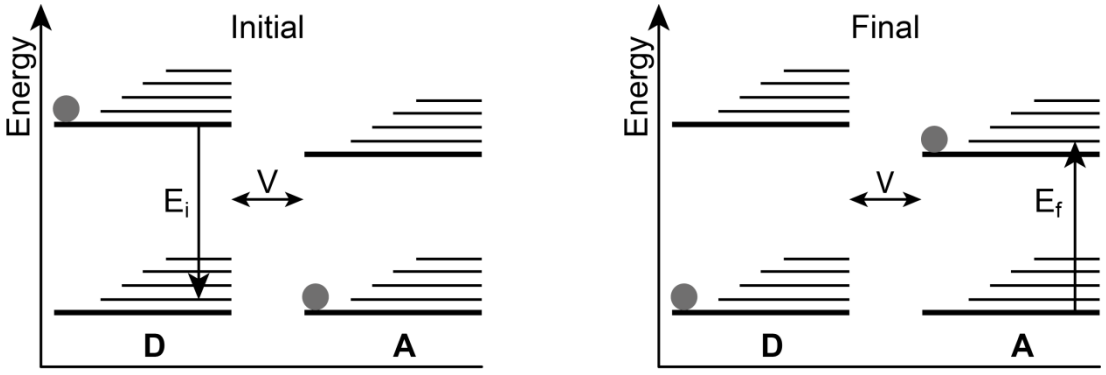

Figure 2.4: Sketch of the incoherent energy transfer in a simple donor-acceptor system. Donor D and acceptor A are coupled by an interaction V. In the initial configuration $|i\rangle$, D is in the excited state, while A is in its ground state, as indicated by the grey spheres. In the final configuration $|f\rangle$, D is in its ground state, while A is in an excited state. Energy transfer is only possible, if $E_i = E_f$. Sketch adapted from [11].

$$k_{DA} = \frac{2\pi}{\hbar} \int dE_i \int dE_f \ \rho(E_i) |\langle f|V|i\rangle|^2 \delta(E_f - E_i). \qquad 2.6$$

In this expression, $|i\rangle$ and $|f\rangle$ denote the wave functions of the state where the donor is excited, while the acceptor is in its ground state and *vice versa*, respectively. $|\langle f|V|i\rangle|^2$ is the matrix element of the coupling, while $\rho(E_i)$ is the density of states of the donor molecule D. The delta function $\delta(E_f - E_i)$ is only then different from zero, when the energy of the electronic transition in the initial state E_i is equal to the one in the final state E_f, which ensures energy conservation.

The version of Fermi's Golden Rule given in Equation 2.6 is very general and does not specify the type of interaction between D and A. In a very coarse approximation that only takes dipole-dipole interaction into account, we end up with the often used Förster approximation. This treatment is only valid, when the spatial separation between D and A is much larger than the size of the interacting dipoles and when the coupling between D and A does not perturb the energetic and dynamic properties of either molecule [30]. In most multichromophoric systems, this is clearly not the case and more advanced approaches for the coupling mechanism have to be considered. Examples are generalized Förster Resonance Energy Transfer [30], multichromophoric Förster Resonance Energy Transfer [31] and Red-field theory [32].

2.4. Exciton-Exciton Interaction

As the studies in Chapters 4-6 deal with multichromophoric systems, we also face the possibility of creating more than one excitation within the same system. As a result, these excitations can interact, resulting in a process called annihilation [33,34]. HOFKENS *et. al* [35] used a picture of one-electron molecular orbitals to demonstrate this process. This picture is an approximation that is often used in solid state physics for extended systems where countless electrons are present. For systems on the molecular scale, such as multichromophoric systems, this approximation does not hold

true and should not be used. The one-electron picture is, nevertheless very instructive and thus we want to use it to explain annihilation.

We consider two close lying chromophores. One of them is in the first excited singlet state S_1, while the other is in the first excited triplet state T_1. It is then possible for the first chromophore to transfer its excitation energy to the second one. There, a higher excited triplet state T_n is created, while the first chromophore returns to its ground state S_0. By internal conversion, the higher excited triplet state T_n decays to T_1. We are then back at the initial situation, but with the difference that one singlet excitation has been annihilated and transformed to heat. This process is called singlet-triplet annihilation (STA). Other possible annihilation processes are singlet-singlet annihilation (SSA), triplet-triplet annihilation (TTA) and triplet-singlet annihilation (TSA), where the triplet state is annihilated and the singlet state persists [36,37].

In the past, extensive and complicated theoretical frameworks were used to describe annihilation in organic molecular crystals [38] or bacterial chromatophores [39]. In Chapter 4, we will show a way to model STA in a simple and efficient way.

2.5. Plasmon-Emitter Interaction

Note: A similar description of plasmon-emitter interaction as presented in this section has already been published in [20]. The discussion as found in this work considers a more general aspect of plasmon-emitter interaction as compared to the discussion there. The section at hand follows the line of argumentation as found in [40].

In Chapter 5 we will discuss the interaction of a gold nanoparticle with a single LH2 complex. The resulting effect, plasmon enhancement, can be explained by classical electrodynamics in analogy to antenna theory [40]. A plasmon is the quasi-particle that results from collective electron density oscillations in a metal. More precisely, we have to make a distinction between surface plasmons, as they can be observed on plane metal surfaces and particle plasmons that exist in small metal nanoparticles [41]. For

reasons of brevity the common term "plasmon" will be used in this work. In noble metal nanostructures, plasmons can be excited by light in the visible to near infrared spectral range. This simplifies the generation of cooperative effects between plasmons and chromophores.

Due to the interaction of a chromophore with a plasmonic structure, the photon emission of the chromophore can be increased, which is commonly referred to plasmon enhancement. The effect can be separated into three contributions. An enhancement of the absorptive rate of the chromophore, an increase in its radiative rate and a loss mechanism that causes electronic excitations of the chromophore to be quenched by the metal structure [18,40]. The enhancement of the absorptive rate can be explained as follows: In the absence of the nanoparticle, the chromophore only witnesses the electric field of the incident light $\vec{E}_0(\vec{r})$ which induces transitions from the chromophore's ground state to an excited state. In the presence of the nanoparticle, we will find an additional electric field $\vec{E}_{scatt}(\vec{r})$ that is due to scattering caused by the nanoparticle and thus the electric field in the presence of the nanoparticle is $\vec{E}_{NP}(\vec{r}) = \vec{E}_0(\vec{r}) + \vec{E}_{scatt}(\vec{r})$. The enhancement factor of the absorptive rate is then [40]

$$P_{abs}(\vec{r}) = \left|\vec{E}_{NP}(\vec{r})\right|^2 / \left|\vec{E}_0(\vec{r})\right|^2. \qquad 2.7$$

The magnitude and orientation of $\vec{E}_{scatt}(\vec{r})$ depends crucially on the size and shape of the nanoparticle, its material (represented by its wavelength dependent dielectric function $\varepsilon(\lambda)$) and the material of its surrounding.

Due to the coupling of the chromophore's states to those of the metal particle we will also find a change in the chromophore's radiative rate k_{rad}, and the possibility to transfer energy from an excited state of the chromophore to the metal particle, represented by k_{loss}. Both rates contribute to the fluorescence quantum yield of the coupled chromophore. In the absence of the nanoparticle the quantum yield is

$$\Phi_F^{(0)} = \frac{k_{rad,0}}{k_{rad,0}+k_{nr,0}}, \qquad 2.8$$

where $k_{rad,0}$ and $k_{nr,0}$ are the radiative and non-radiative decay rates of the uncoupled system, respectively. Under the assumption, that $k_{nr,0}$ remains unaltered by the coupling to the nanoparticle and with the introduction of the additional loss channel the fluorescence quantum yield for the coupled system reads [40]

$$\Phi_F = \frac{k_{rad}}{k_{rad}+k_{nr,0}+k_{loss}} = \frac{k_{rad}/k_{rad,0}}{k_{rad}/k_{rad,0}+ k_{loss}/k_{rad,0}+ \left(1-\Phi_F^{(0)}\right)/\Phi_F^{(0)}}. \qquad 2.9$$

The enhanced radiative rate as well as k_{loss} can be calculated on the basis of the size and shape of the nanoparticle, its materials parameters as well as the distance and mutual orientation between particle and chromophore. As this plays only a minor role in the experiments presented in Chapter 5, we will not go into the details of this calculation. The enhancement factor of the quantum yield is now easily accessible as $P_\Phi = \Phi_F/\Phi_F^{(0)}$ and the overall enhancement of the chromophore's photon emission is given as

$$P_{total} = P_{abs} \cdot P_\Phi. \qquad 2.10$$

For short distances between chromophore and nanoparticle it is possible that k_{loss} becomes large and $P_\Phi < 1$. If P_{abs} cannot compensate for this, the overall enhancement factor will drop below 1, which results in plasmon quenching. An excellent example of the distance dependence of plasmon enhancement and plasmon quenching is given in [18] by ANGER *et al*.

3. Experimental Setups and Techniques

This chapter gives an overview of the experimental techniques used in this work. As all three studies presented here required their own experimental approach, each setup was tailored to fit the prerequisites of the respective system. The methods applied comprise time-resolved ensemble spectroscopy with and without spectral dispersion (both realised by a homebuilt streak camera setup), high throughput single molecule spectroscopy (realised by a homebuilt microscope with single molecule sensitivity), steady state absorption and emission spectroscopy, and atomic force microscopy.

3.1. Time-Resolved Ensemble Spectroscopy

Time-resolved spectra of RC-LH1 complexes and of CBT derivatives were recorded using a streak camera setup. To account for the different emission intensities of both system classes, two different configurations of the setup had to be used. This in turn led to a different depth of information that was available from the experiments and required different post processing methods.

3.1.1. Streak Camera Principle

The basic idea of a streak camera is to translate temporal information into spatial information [42]. The light to be analysed, for example the fluorescence from a sample, is focussed onto a photocathode where photoelectrons are emitted into an evacuated tube. Within this so called streak tube, the electrons are accelerated by the voltage applied to a mesh and travel through the tube along its long axis. Perpendicular to the direction of acceleration, a pair of electrodes (sweep electrodes) applies a deflection potential to the photoelectrons. The deflection potential increases with time, after an initial trigger signal was received, which synchronizes the voltage sweep of the deflection electrodes with the excitation laser pulses that cause fluorescence from the

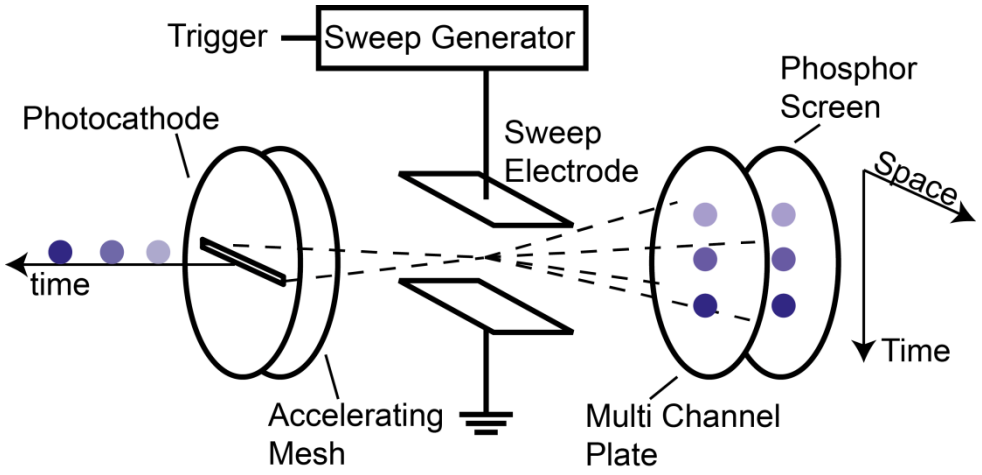

Figure 3.1: Conceptual setup of a streak tube. Incident photons (coloured spheres) hit the photocathode, where electrons are emitted into the evacuated streak tube. Accelerated by a mesh under high voltage, they travel through the streak tube and are deflected by an electric field at the sweep electrodes with a time dependent sweep voltage. At the multichannel plate the incident electrons are multiplied and subsequently hit a phosphor screen where photons are emitted that are detected by a CCD camera. Adapted from **[42]**.

sample. The result is that an earlier photoelectron will be less deflected than a later one. At the end of the streak tube the electrons hit a multichannel plate where they are multiplied and directed onto a phosphor screen. There, the electrons induce phosphorescence and the resulting photons are detected by a CCD camera [43]. The concept of a streak tube is sketched in Figure 3.1.

Through this process, temporal information contained in the stream of incident photons is projected onto the spatial axis along the direction of the deflection potential, while the axis perpendicular to it retains its spatial information. The remaining spatial axis can be used for spectral dispersion, which results in the recording of transient emission spectra, to effectively increase the detection volume or to visualize a spatially progressing process. The first two applications will be presented in sections 3.1.3 and 3.1.4.

The streak camera system used in this work (streak system C5680 with CCD camera Orca-ER C4752, Hamamatsu Photonics) was operated in combination with an imaging

spectrograph (250 IS, Bruker). An automated turret inside the spectrograph allowed easy switching between different dispersive gratings or a mirror for measurements where no spectral dispersion was desired. A temporal resolution below 2 ps was possible for the smallest accessible time window (200 ps). For the time windows used in this work (2 and 5 ns, respectively) a time resolution of 50 ps was common. Through the dispersive gratings, a spectral range from the near ultraviolet to the near infrared was accessible. The photocathode of the streak tube though, puts a constraint on the spectral region that can practically be used. It has a maximum quantum efficiency of around 12% in the region between 280 and 430 nm. Towards higher wavelengths its quantum efficiency steadily drops to 2% at 800 nm and 0.5% at 900 nm [44]. Measuring spectrally dispersed signals in the near infrared region thus requires very long integration times and/or high excitation fluences to compensate for the low detection efficiency.

3.1.2. Light Source

As light source for the ensemble experiments serves a pulsed Ti:Sapphire laser (Tsunami, Spectra Physics) which is pumped by a frequency doubled Nd:YVO_4 laser (Millenia X, Spectra Physics). The Ti:Sapphire laser is equipped with a set of mirrors that enables pulsed operation with laser pulses shorter than 2 ps (full width at half maximum, FWHM) at a repetition rate of 81 MHz with a wavelength that could be varied from 700 to 1000 nm. For all ensemble experiments discussed in this work, the wavelength of the laser was kept at 879 nm.

The light from the Ti:Sapphire laser was fed into a combined pulse picker and frequency doubler unit (see Figure 3.2). Within the picker stage the incoming light is periodically deflected by an acousto-optic modulator (AOM) with a set frequency. The undeflected beam is thereby dumped into a beam stop. The deflected beam is referred to as the picked beam and is used as the excitation beam. In the experiments discussed later, the repetition rate of deflection was set to 8.1 MHz, 810 kHz and 81 kHz,

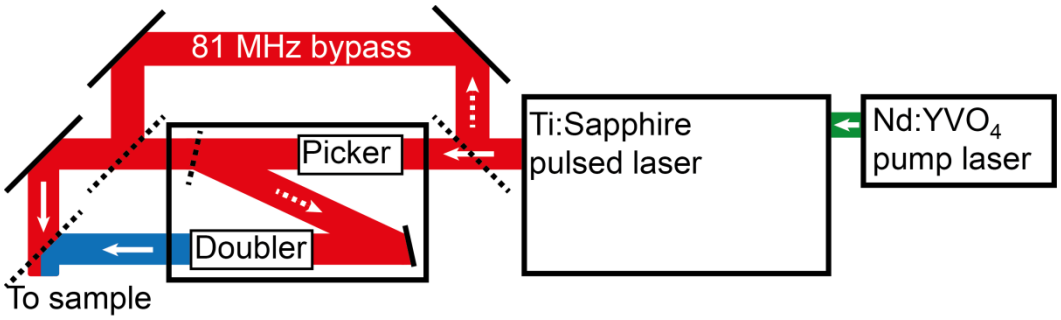

Figure 3.2: Schematic of the excitation light source used in the time-resolved ensemble experiments. The light of a Nd:YVO_4 laser at 514 nm is used to pump a Ti:Sapphire laser that yields light pulses of less than 2 ps (FWHM) at 879 nm with a repetition rate of 81 MHz. This light can either be picked and/or frequency doubled in a picker/doubler unit or bypass this unit via flip mirrors (dotted lines).

respectively. For excitation with the native repetition rate of the laser of 81 MHz the picker/doubler unit could be bypassed via two flip mirrors and the beam was fed into the excitation beam path unpicked.

For excitation in the blue spectral region, an additional frequency doubler stage could be accessed by an additional mirror that could be installed in the beam path behind the picker stage (drawn as a flip mirror in Figure 3.2). Via a temperature stabilized lithium triborate (LBO) crystal the incident light of 879 nm could be frequency doubled to approximately 440 nm. This made blue light with repetition rates of 8.1 MHz, 810 kHz and 81 kHz available. To enable blue light excitation with a repetition rate of 81 MHz the pulse picker's AOM had to be removed and the beam path was realigned to feed the unpicked beam into the doubler unit. In any case the excitation light was eventually reflected towards the excitation beam path with a set of mirrors and focussed into the sample volume.

To ensure reproducible excitation conditions within the sample volume, the beam waist and the Rayleigh length of the excitation beam were determined prior to any other measurement. Therefore, the regular sample holder (rotating cuvette in Figure 3.3 and quartz glass cuvette in Figure 3.4, respectively) was removed and a CCD camera (Orca, Hamamatsu Photonics) that was mounted on a translation stage was installed instead.

By moving the CCD camera in fixed steps along the beam direction, both aforementioned beam parameters could be determined. This in turn gave a measure of the $1/e^2$-diameter of the excitation spot and thus of its area. By measuring the integrated equivalent cw excitation intensity, together with the excitation wavelength and repetition rate of the laser beam, the precise excitation fluence (defined as photons per pulse per area) could be determined. Adjustment of the excitation fluence was possible via a variable neutral density filter (M925B, Newport) that was installed in the excitation beam path.

3.1.3. Streak Setup for RC-LH1 Detection

For the experiments on RC-LH1 from *Rps. palustris* the streak camera setup was used in a mode that effectively increased the detection volume. This step was necessary as RC-LH1 emits mainly above 900 nm, in a spectral region where the streak camera setup has a very low detection efficiency. Furthermore, the range of excitation fluences covered several orders of magnitude and most of them were too low to allow the recording of spectrally dispersed emission from RC-LH1 (see Chapter 4 for details on RC-LH1).

For that reason, an expanded focal volume was used. The parameters of the excitation beam were chosen such, that over a region of about 2 mm along the optical axis, which was centred around the beam waist, the diameter of the beam changed by less than 2 %. This defined the focal volume of the experiments. At very low sample concentrations, as they were used in the experiments, the assumption is justified that the excitation fluence stays constant along the whole 2 mm region of the excitation beam.

For the experiments on RC-LH1 a home-built rotating cuvette with an arm length of 9.5 mm, made from acrylic glass was used as a sample holder. Spinning the cuvette at a frequency of 48 Hz ensured a constant flux of fresh sample, thus avoiding effects of photodegradation.

The fluorescence light from the focal volume was collected in right angle geometry (see Figure 3.3a) and filtered through a dielectric bandpass filter that was centred around 925 nm and had a bandwidth of 40 nm (BP925/40, AHF analysentechnik). At very high excitation fluences saturation of the detector was possible despite the low detection efficiency of the streak camera. To prevent this, neutral density filters were introduced into the detection beam path whenever necessary. Subsequently, the focal volume was imaged onto the entrance slit of the spectrometer with a magnification of 1. The width of the slit was kept at 2 mm to ensure no light from the region of uniform excitation was lost. Within the spectrometer, a mirror in place of a dispersive grating reflected the incident light towards the photocathode of the streak camera system.

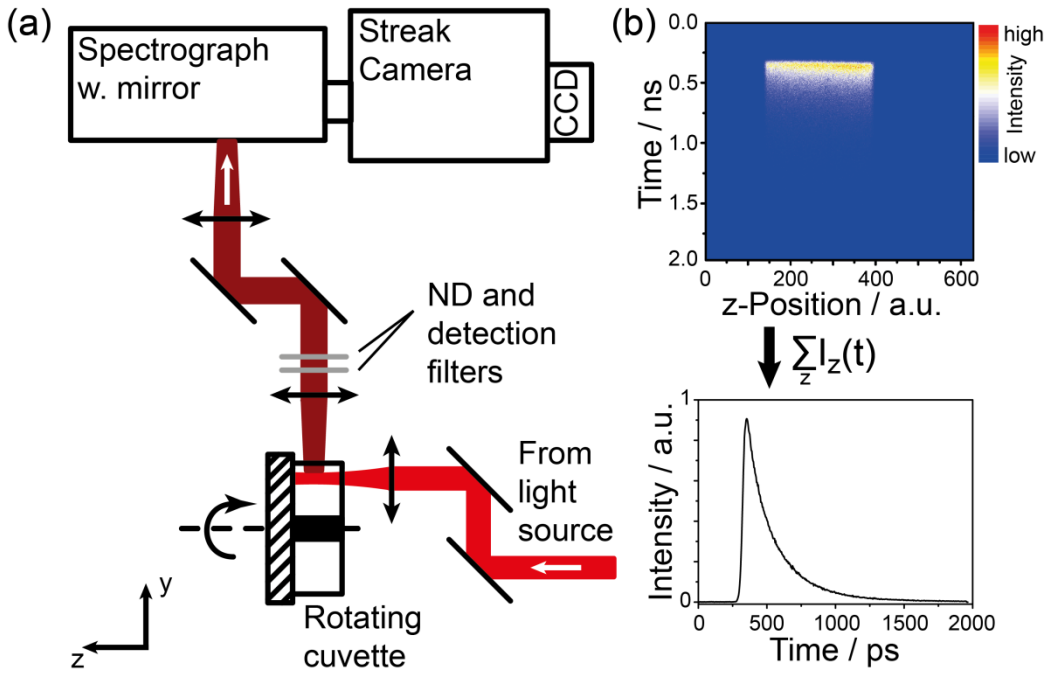

Figure 3.3: a) Schematic of the detection beam path used in time-resolved experiments on RC-LH1. Incident excitation light was focussed into the sample, which is held by a rotating cuvette. Fluorescence light from the sample was collected by an achromatic lens and filtered by a bandpass. ND filters were used if necessary. The filtered light was focussed onto the entrance slit of a spectrograph that reflected the incoming light onto the photocathode of the streak camera with a mirror. Dimensions are not to scale. b) Top: Example of the data acquired with the setup from (a). By correction for arrival times and integration over the data columns a single fluorescence transient was obtained (bottom).

The result was a streak image, where the spatial coordinate of the traveling direction of the excitation beam was retained, while the temporal axis registered the transients along the excitation beam (for an example, see Figure 3.3b, top). The propagation of the excitation beam through the sample introduces a delay in the arrival time of photons from different positions along the beam path that increases the further the beam progresses. To correct the recorded streak image for this delay, the temporal offset between the maxima of the outermost transients was determined. These transients correspond to the positions where the beam enters the sample and where it leaves the sample, respectively. As the delay increases linearly with the spatial coordinate, the delay of every individual transient with respect to the outermost one at the entrance side of the excitation beam could then be calculated and computationally be corrected for by shifting the respective transient along the temporal axis. By subsequent integration over the spatial coordinate, one single fluorescence transient with an appropriate signal-to-noise ratio could be obtained (Figure 3.3b, bottom).

For means of data processing and to determine the temporal resolution of the streak camera system, the instrument response function (IRF), was recorded with excitation light scattered in buffer solution that contained no RC-LH1 complexes. For this measurement the bandpass filter was removed from the detection beam path and an instrument response time of 50 ps (FWHM) could be obtained.

3.1.4. Streak Setup for CBT Derivative Detection

For the experiments on CBT derivatives the streak camera setup could be used in a ‘classical’ configuration. As most of those compounds show a higher fluorescence quantum yield than RC-LH1 and as they fluoresce in a spectral region where the setups sensitivity is rather good, the signal was sufficient to be spectrally dispersed before being focussed onto the streak tube’s photocathode.

The excitation beam was widened up by a telescope and then strongly focussed into the sample volume (see Figure 3.4a). This resulted in a small focal volume and allowed sufficient excitation fluences for the given maximum laser power. Emission from the

focal volume was imaged onto the entrance slit of the spectrometer. Via a dispersive grating (100 g/mm, blazed at 450 nm), the spectrum of the emitted light was focussed onto the photocathode of the streak tube. The slit width was adjusted such, that a spectral resolution better than 2.5 nm was achieved.

For the spectral calibration of the detector unit, the characteristic spectral lines of a Xenon and a Neon pen-ray lamp (both Oriel) were used. To obtain the spectral sensitivity of the streak camera setup the emission spectrum of Coumarin 153 (10 µM Coumarin 153 in Ethanol p.a.) was measured. It was then compared to an emission spectrum of Coumarin 153 that was recorded under the same environmental conditions with a commercial spectrofluorometer (FP-8600, Jasco, see section 3.3) that had already been corrected for spectral sensitivity. This made it possible to correct all

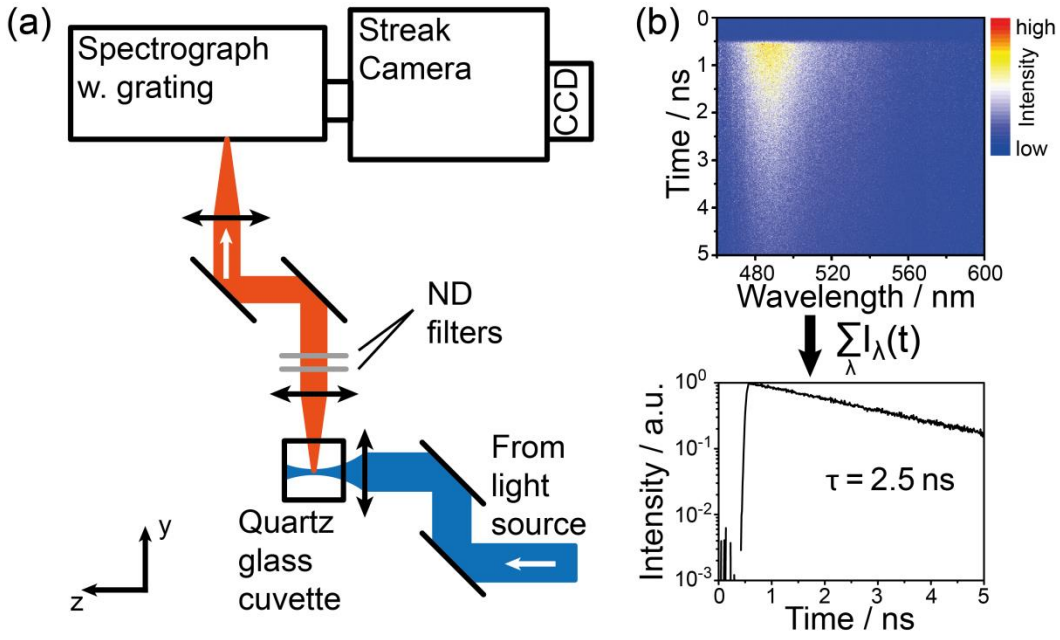

Figure 3.4: a) Schematic of the detection beam path used in time-resolved ensemble experiments on CBT derivatives. Incident excitation light was focused tightly into the sample volume. Fluorescence light from the sample was collected by an achromatic lens and adjusted in intensity with ND filters if necessary. Subsequently it was focused onto the entrance slit of a spectrograph where the signal was spectrally dispersed and focused onto the streak camera's photocathode. Dimensions are not to scale. b) Top: Example for the data acquired with the setup from (a). By integration over the spectral coordinate a single fluorescence transient was obtained (bottom).

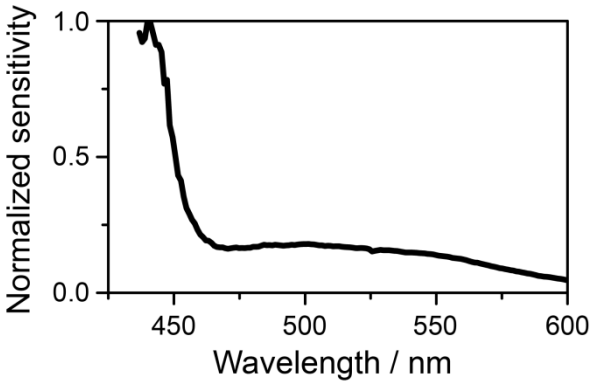

Figure 3.5: Spectral sensitivity of the streak camera setup between 438 and 600 nm. The maximum of the sensitivity curve was normalised to 1. The spectral sensitivity was obtained using a solution of 10 µM Coumarin 153 in Ethanol. For further details see text.

recorded spectra for the spectral sensitivity of the streak camera setup with the help of home-written software and resulted in measurements as shown in Figure 3.4b (top). By integration along the spectral axis, the integrated fluorescence decays of the CBT derivatives under investigation were obtained (for an example see Figure 3.4b, bottom).

Figure 3.5 shows the spectral sensitivity of the streak camera setup between 438 and 600 nm. It was calculated by dividing the spectrum of Coumarin 153 as recorded with the streak setup by the spectrum of Coumarin 153 that had already been corrected for spectral sensitivity. The resulting spectrum was divided by its maximum value to obtain the normalised sensitivity curve.

3.2. Single Molecule Spectroscopy

For the experiments on LH2-AuNP hybrids, a single molecule setup was used, as this approach was most promising for the underlying problem.

The light source for these experiment was either an Ar-Ion laser (Innova 90, Coherent) operated at 514 nm for excitation in the green or a Ti:Sapphire laser (Tsunami, Spectra Physics) run at 788 nm for excitation in the red. Both lasers worked in continuous wave

mode. Before either beam was coupled into the excitation beam path, they were focussed onto a pinhole to ensure a Gaussian beam profile and were subsequently collimated.

In the excitation beam path the laser beam was expanded to a diameter of about 20 mm and the innermost 6 mm of diameter were cut out, using an iris diaphragm (see Figure 3.6a for a sketch of the setup). Later on, this ensured a homogenous excitation intensity across the whole excitation spot in the sample plane (deviations up to 5 % were tolerated). In the case of excitation in the green, the beam passed a laser clean-up filter (HQ500/50, AHF analysentechnik) and was reflected towards a microscope stage via a dichroic beam splitter (530DCXR, AHF analysentechnik). In the case of excitation in the red, the clean-up filter was not necessary and the dichroic beam splitter was replaced by a 50/50 beam splitter. A flippable widefield lens in front of the dichroic beam splitter enabled the switching between confocal and widefield illumination. A

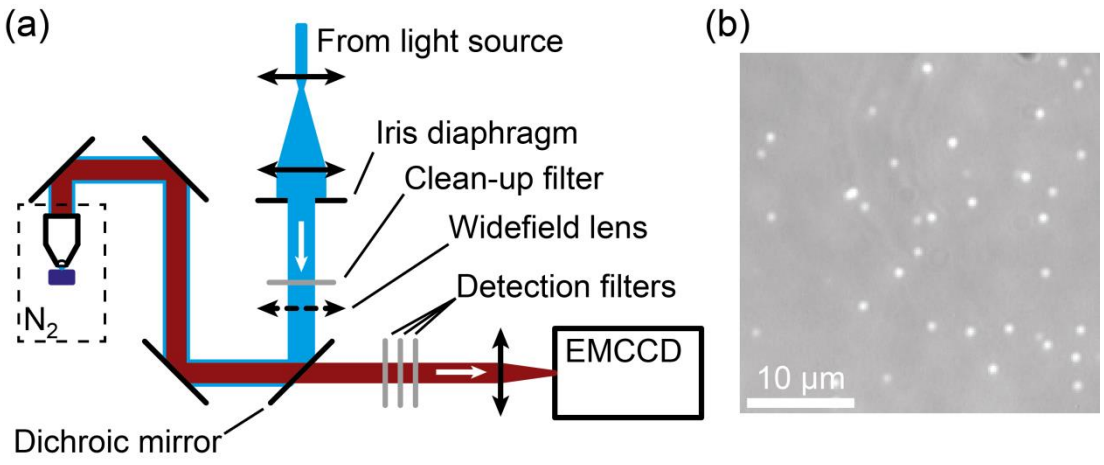

Figure 3.6: a) Schematic of the single molecule setup used for the analysis of AuNP-LH2 hybrids. The light of the excitation laser was expanded and the inner part was cut out by an iris diaphragm to ensure a homogenous excitation profile. The light was reflected towards a microscope objective by a dichroic beam splitter and focussed onto the sample. Fluorescence light was collected through the same objective and focussed onto an electron multiplying CCD camera after spectral filtering. The sample and the microscope objective were housed in a recipient that was flushed with dry nitrogen. Dimensions are not to scale. b) Example of a typical wide-field image recorded with the setup depicted in (a). The emission intensities from individual LH2 complexes from *Rhodopseudomonas acidophila* are clearly visible as bright spots against the background (colour-coded in grey).

microscope objective (S.PlanM60x, Euromax Holland) focussed the excitation light onto the sample, producing a focal spot of 30 µm in diameter. The sample holder and the objective were housed inside a recipient that was flushed with dry Nitrogen gas to minimize the effects of photo-degradation.

The fluorescence from the sample was collected through the same microscope objective used for excitation. After passing the dichroic mirror the remaining excitation light that was reflected by the sample was filtered by three long-pass filters with their spectral edges at 545, 635 and 808 nm (LP545, LP635, LP808, AHF analysentechnik). In the case of excitation in the red, the filters used were an LP808 and 2× LP830 (AHF analysentechnik). The filtered image from the sample was imaged onto an electron multiplying CCD camera (iXon X1214, Andor Technologies). Every image from the camera delivered several well separated intensity spots (for an example, see Figure 3.6b), that each result from the emission of one single LH2 complex.

Home-written software identified individual LH2 complexes in the images, extracted their background-corrected and integrated emission intensities and registered them in the memory of the computer. For a detailed description of the software see [20]. Through automation, the intensities of more than 4200 single complexes contributed to the histograms shown in Chapter 5.

3.3. Steady State Optical Spectroscopy

Steady state absorption spectra were recorded on a commercial Lambda 750 spectrophotometer (Perkin Elmer). The spectral resolution was set to either 1 or 2 nm, depending on the sample, with a scan speed of 274 nm/min. The detection range was set according to sample properties.

Steady state emission spectra were recorded on a commercial FP-8600 spectrofluorometer (Jasco), access to which was kindly provided by the workgroup of Prof. Dr. H-W. Schmidt, University of Bayreuth. The apparatus allowed to

automatically record emission spectra as a function of the excitation wavelength. This gave access to the photoluminescence emission maps presented in Chapter 6. Besides the wavelength dependent emission these maps simultaneously show PL-excitation spectra for varying detection wavelengths. The resulting PL-emission spectra had a spectral resolution of 2 nm while that of the PL-excitation spectra was 5 nm. The instrument's scan speed was kept at 200 nm/min, the detection range was set according to sample properties.

3.4. Atomic Force Microscopy

For the characterisation of thin PVA films, Atomic Force Microscopy (AFM) was used. After preparation, the films were scratched with the back of a scalpel. Care was taken not to scratch the substrate itself in this process. The height of this scratch, and thus of the PVA film, was measured with a commercial atomic force microscope (Nanosurf Easy Scan 2) in non-contact tapping mode. The cantilevers used (Si cantilever, n-type, AppNano) had a nominal tip radius smaller than 10 nm with an eigenfrequency of 145-230 kHz and a spring constant of 20-95 N/m.

4. Natural System: Time-Resolved Fluorescence Spectroscopy on RC-LH1

The work presented in this chapter investigates the energy transfer characteristics of RC-LH1 from *Rhodopseudomonas (Rps.) palustris* by means of time-resolved optical spectroscopy in the picosecond range. A systematic approach in combination with detailed model simulations, allowed deep insight on the dependence of the RC's redox state on the external parameters photon fluence and repetition rate of the excitation laser. The model reproduced the measured fluorescence transients very well and made it possible to predict the relative population of triplet states on the LH1 ring as well as the fraction of closed RCs as a function of the external parameters.

Note: This chapter closely follows and in wide parts cites the publication S. R. Beyer, L. Müller *et al.*, "The Open, the Closed, and the Empty: Time-Resolved Fluorescence Spectroscopy and Computational Analysis of RC-LH1 Complexes from *Rhodopseudomonas palustris*", *The Journal of Physical Chemistry B*, **119**, 1362-1373 (2015) [45]. Model simulations were carried out by Mr. Lars Müller at the workgroup of Prof. G. Matthias Ullmann at the University of Bayreuth. The model presented in section 4.4 was developed in close cooperation between the author and Mr. Müller. RC-LH1 complexes were kindly provided by the workgroup of Prof. Richard J. Cogdell, University of Glasgow. Preparation of the complexes was conducted by Ms. June Southall.

4.1. Introduction

By evolutionary selection, Nature has developed countless variations of the photosynthetic concept, each of them realized in a different organism. This plethora of life forms comprises plants, algae and bacteria. One group of photosynthetic bacteria are the so called non-sulphur purple bacteria, which can be found in the oxygen-devoid layers of ponds, lakes and streams [9].

4.1.1. Photosynthesis of Purple Bacteria

Purple bacteria adapted to their habitat by evolving a variation of photosynthesis that is based on a cyclic electron transfer chain that does not require the external intake of oxygen [11], in contrast to the photosynthesis of plants. Furthermore, purple bacteria adapted to the light conditions of the depth. As algae and cyanobacteria in the upper layers of the habitat effectively filter the solar spectrum, purple bacteria shifted their maxima of light absorption towards the near infrared (NIR) and the green spectral region [47]. Inside these bacteria, we find invaginations of the cell membrane that are called chromatophores. The lipid bilayer of the chromatophores houses a modular assembly of membrane proteins that constitutes the purple bacteria's photosynthetic apparatus [8].

Peripheral antenna complexes [48–50], the light-harvesting II complexes (LH2), are arranged in a two-dimensional network within the membrane (see Figure 4.1) [51]. They absorb incoming photons and deliver the so gathered energy to further light-

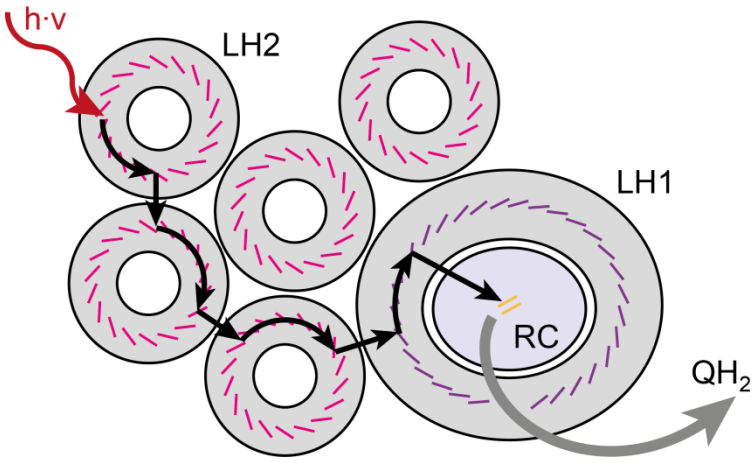

Figure 4.1: Sketched view onto the photosynthetic membrane of purple bacteria (perpendicular to the membrane plane). For clarity, only light-harvesting complexes and the reaction centre are shown. Black arrows indicate energy transfer, grey ones the transfer of QH_2 molecules. Energy absorbed by a LH2 is transferred by means of the B850 pigments (magenta) among the network of LH2 complexes until it reaches the B875 pigments (purple) of the LH1 ring. It is then transferred to the BChl *a* of the RC's special pair (orange) where a charge separation is initiated and Q is reduced. Once Q is doubly reduced, QH_2 is transferred to cytochrome b/c_1 and replaced by Q. Adapted from [46].

harvesting complexes in the form of molecular excitations. Once the excitation reaches a primary antenna, the light-harvesting I complex (LH1) [12,52,53], the energy is transferred from LH1 to a protein called the reaction centre (RC), where it is used to induce a charge separation and to reduce an ubiquinone molecule (Q) [54]. The joint assembly of LH1 and RC is called a core complex, abbreviated as RC-LH1. Once Q is doubly reduced, it is transferred to a cytochrome b/c_1 complex in the form of QH_2, where it is used to establish a proton gradient across the membrane, while Q is restored to its neutral form and the excess electrons are transferred back to the RC via a cytochrome *c* complex. The transmembrane proton gradient is the driving force for ATP-Synthase that synthesizes adenosine triphosphate (ATP) from adenosine diphosphate (ADP) and inorganic phosphate (P_i) [55]. ATP serves as the energetic currency of life that can easily be transported to different spots within the cell, where it is again split into ADP and P_i and the released energy is used to power a wide range of processes. The work presented in this chapter will focus on the investigation of the energy transfer dynamics of reaction centre light-harvesting 1 complexes.

4.1.2. Structure of RC-LH1 from *Rps. palustris*

The basic motif in the structure of RC-LH1 complexes is that the elliptical LH1 complex encircles the RC. It defines the mutual functional relationship between LH1 and RC and is conserved among different species of purple bacteria. While this basic idea is maintained, the details do differ between species. We will find S-shaped, dimeric RC-LH1 [56] in *Rhodobacter (Rb.) sphaeroides* [52,57] while those of *Thermochromatium (T.) tepidum* are monomeric with a 'closed' ring-like pigment assembly in LH1 [53]. The RC-LH1 complexes from *Rhodopseudomonas (Rps.) palustris*, which will be discussed here, are monomeric and feature a 'gap' in the elliptical pigment assembly of the LH1 ring [12].

LH1 from *Rps. palustris* consists of 15 pairs of transmembrane helices labelled α and β as well as a single polypeptide labelled W (see Figure 4.2). These 16 units form a ring-like, elliptical structure that surrounds the RC. Each α-β pair non-covalently binds a

dimer of bacteriochlorophyll *a* (BChl *a*) molecules. In total these 30 BChl *a* molecules form an ellipse of close lying pigments that features a gap, where the W polypeptide is located [12]. The information from x-ray crystallography is also consistent with data from optical single-molecule experiments [58,59]. Spirilloxanthin carotenoid molecules connect the α-β subunits pairwise and help to stabilize the LH1 complex while serving as additional pigments.

The reaction centre is placed in the middle of the LH1 ring and is also built from a protein shell that arranges several pigments (Figure 4.2) [60–63]. Its structure is mostly conserved between different bacterial species and even shows high homology with the RCs from plants [13,64,65]. It accommodates a BChl *a* dimer (special pair, primary donor, P), two accessory BChl *a* molecules (B_A, B_B), two bacteriopheophytin a (BPheo a) molecules (H_A, H_B), and two ubiquinones (Q_A, Q_B) bound to two protein subunits denoted L and M. The cofactors are arranged in two nearly identical branches, called A and B, which share the primary donor, P [61,63,66,67].

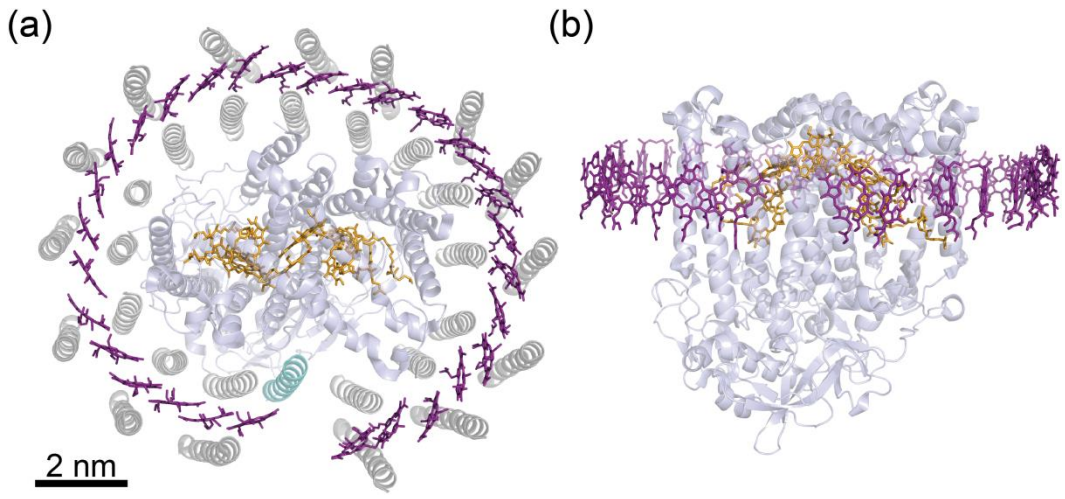

Figure 4.2: Crystal structure of RC-LH1 from *Rps. palustris* at a resolution of 4.8 Å. α- and β-polypeptides are depicted in light and dark grey, respectively, W in cyan and the protein shell of the RC in light blue. B875 pigments of the LH1 ring are held in purple, RC pigments in orange. a) View perpendicular to the membrane plane. b) View from within the membrane. α- and β-polypeptides were omitted for reasons of clarity. In both views the Car molecules are not shown. Redrawn from PDB entry 1PYH [12].

4.1.3. Energy and Electron Transfer in RC-LH1

In the LH1 ring of *Rps. palustris*, the BChl *a* molecules are oriented such, that their Q_y transition dipole moments lie almost perfectly within the membrane plane. Moreover those two BChl *a* molecules that are bound by the same α-β subunit lie antiparallel to each other. In the overall picture this leads, together with the close spacing between the Bchl *a*, to a system of 15 strongly coupled dimers, with a strong coupling between adjacent dimers. This pigment pool gives rise to a room temperature absorption band that is centred around 875 nm and is therefore called B875 (Figure 4.3a).

Mathematically this can be treated within the formalism discussed in Section 2.2 as a linear chain of coupled dipoles in the strong coupling regime and with the geometric constraints of the elliptical assembly [58]. The result is an excitonic system with 30 exciton states, labelled $k = 1, \ldots, 30$, in energetically increasing order (Figure 4.3b). Excitation of a higher lying exciton state, either by energy transfer from another LH complex or absorption of a photon, leads to an ultrafast relaxation on a timescale of about 100 fs along the ladder of exciton states into the lowest lying $k = 1$ state [68,69].

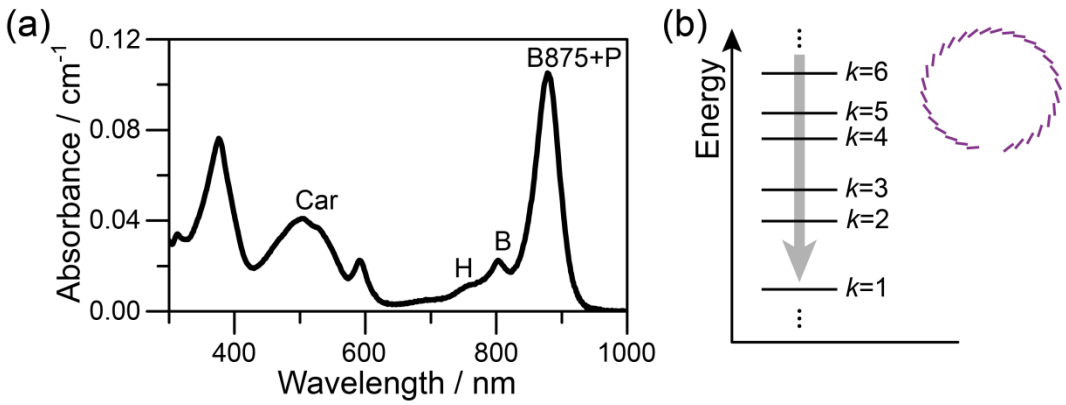

Figure 4.3: a) Room temperature absorption spectrum of a dilute sample of RC-LH1 from *Rps. palustris*. The absorption bands of the different pigment pools are highlighted by their respective abbreviations. b) Sketch of the six energetically lowest lying exciton states of the idealized BChl *a* pigment pool from the LH1 ring of *Rps. palustris* (purple inset). Higher excited exciton states relax into the lowest lying exciton state $k = 1$ on an ultrafast timescale of about 100 fs, as indicated by the grey arrow. The electronic ground state of the idealized BChl *a* pigment pool as well as exciton states $k > 6$ are not shown.

The strong coupling furthermore leads to a delocalisation of the exciton over several pigments [11]. This is thought to have at least two benefits: On the one hand, local energetic traps can be avoided and thus improve the energy transfer to the special pair of the RC, on the other hand, it enables the LH1 antenna to transfer energy to an adjacent LH1 more easily in the case that its corresponding RC cannot accept the energy trapped on LH1.

The carotenoid molecules play a double role in the energy transfer kinetics of the LH1 ring. Their first one is as additional pigments in the green spectral region. Energy absorbed by the Car will be transferred to the B875 band on a fast timescale, which effectively extends the absorption cross section of LH1 spectrally and realizes the concept of an energy funnel [8]. Their second role is as a protective switch. There is a small chance that an excitation of the B875 band leads to a BChl *a* triplet state by intersystem crossing, $^1\text{B875}^* \rightarrow {}^3\text{B875}^*$. These triplets pose a threat to the organism as their presence can lead to the generation of singlet oxygen, which can cause severe damage to the cell's structure. By acting as a quencher for BChl *a* triplet states, $^3\text{B875}^* + {}^1\text{Car} \rightarrow {}^1\text{B875} + {}^3\text{Car}^*$, the carotenoids actively prevent the generation of singlet oxygen [70,71]. This is on the price of a long lived (in the order of 10^{-6} s) Car triplet that can be the cause for singlet-triplet annihilation (STA, see section 2.4). A complete summary of the different states of the LH1 ring and the transition rates between those states will be given in section 4.4.1, where the model used for LH1 in this study will be discussed. We will deal with the states and rates that describe the RC accordingly.

The main task of the reaction centre is not to serve as an antenna, but to facilitate a charge separation across the photosynthetic membrane. Upon electronic excitation of the special pair P, this charge separation is induced and leaves the special pair in the oxidized P^+ state, while the electron is first transferred to B_A, then to H_A and subsequently to Q_A where it is temporarily stabilized. In a last step, the electron is transferred to Q_B, where the final stabilisation takes place. After P^+ has recombined to P by uptake of an electron from a nearby cytochrome, the charge transfer cascade takes

place a second time and reduces Q_B^- to Q_B^{2-} [8,13]. The doubly reduced Q_B^{2-} can then be transferred to cytochrome b/c_1 in the form of QH_2 for further use and is replaced by a neutral ubiquinone molecule. Most rate constants for these electron transfers have been reported on the RC from *Rhodobacter* (*Rb.*) *sphaeroides* that has served as a cornerstone for elucidating structure-function relationships employing a large variety of spin resonance [72–77] and optical spectroscopies [78–85].

The excitation of P can either occur by absorption of a photon or via energy transfer from LH1. This energy transfer occurs over a distance of about 40 Å and can therefore be described by an incoherent hopping of the excitation as described in Section 2.3 for the limit of weak electronic coupling [86]. The particular dynamics of the energy transfer between the LH1 and the RC has been the subject of countless studies, and the characteristic time constants that have been found range from several picoseconds up to a few nanoseconds [86–97]. In some studies the fluorescent transients were described by up to five decay times that could not always be attributed to distinct processes. The general picture that has emerged from these studies can be summarized as follows. Time constants up to 10 ps are associated with the detrapping, *i.e.* energy transfer from an excited special pair back to the LH1 ring [98–102]. Energy transfer from the LH1 ring to the neutral special pair takes place with time constants around 30-70 ps [100,103–105], whereas time constants between 200 and 300 ps were attributed to energy transfer from LH1 to the reduced special spair in the RC [103–107]. Decay times between 500 ps and 1 ns have been attributed to the decay of excitations on the LH1 ring [108–110], and decay times longer than that were sometimes interpreted as a charge recombination in the RC which results in delayed fluorescence [101,111,112].

In order to assess these data one has to consider that due to the lack of isolated, purified RC-LH1 complexes at that time many of these studies have been carried out on whole chromatophores from purple bacteria. Hence, either some of these samples contained also an unknown fraction of LH2 complexes, or species were used that did not produce peripheral antenna complexes. In any case intercomplex energy transfer between the LH1 and/or LH2 complexes and the influence of concomitant singlet-singlet

annihilation on the observed dynamics could not be controlled. To the best of our knowledge, exploiting the benefits of isolation and purification protocols for RC-LH1 has led only to one time-resolved pump-probe experiment to date. [113]

Recently, PFLOCK *et al* investigated systematically the energy transfer dynamics of isolated LH2 complexes as a function of the excitation conditions. Combining the experimental results with Dynamic Monte Carlo simulations the authors obtained a quantitative understanding of the fluorescence quenching mechanisms in LH2 without the need for any free parameter [114]. Moreover, using these results as input for the interpretation of the transients obtained on reconstituted homo arrays of LH2 complexes, *i.e.* model membranes of well-defined composition, they revealed a clear influence of the size and the geometry of the LH2 clusters on the fluorescence transients [115].

In line with the studies by PFLOCK et. al, a study on the time-resolved emission from isolated RC-LH1 complexes from the species *Rps. palustris* will be presented, with a systematic variation of the photon fluence, the repetition rate of the excitation laser, and the concentrations of a reducing and an oxidizing agent. The data obtained serve as input for a model that allows to predict quantitatively the time-resolved fluorescence response of isolated RC-LH1 complexes from *Rps. palustris* over a wide range of the above mentioned parameters

4.2. Experimental

4.2.1. Samples

RC-LH1 complexes from *Rps. palustris* were kindly provided by the workgroup of Prof. Richard J. Cogdell, University of Glasgow. Under the lead of Mrs. June Southall, the RC-LH1 complexes were isolated and purified as described previously [12]. After purification, the RC-LH1 complexes were transferred to a buffer containing 20 mM

Tris (tris-hydroxymethyl-aminomethane, Sigma-Aldrich, St. Louis, USA) at pH 8 and 0.02 % DDM (n-Dodecyl β-D-moltoside, Roth, Karlsruhe, Germany). In order to avoid multiple thaw-freeze cycles the material was aliquoted in small amounts and stored at -80 °C until used. For the optical experiments this solution was further diluted with buffer to yield an optical density of 0.1 cm^{-1} at 879 nm. All preparations were made under minimal illumination conditions and the measurements started immediately after the preparation.

4.2.2. Chemical Manipulation

As a reference, we conducted experiments where the time-resolved fluorescence response of RC-LH1 complexes was investigated as a function of the concentration of either a reducing or an oxidizing agent. For the reduction of the RC we used 2,3,5,6-Tetramethyl-p-phenylenediamine (DAD; Sigma-Aldrich, St. Louis, USA) as reducing agent. A stock solution of 100 mM DAD in Ethanol (Sigma-Aldrich, St. Louis, USA) was added to the RC-LH1 solution until the desired final concentration in the sample was achieved. Oxidation of the RC was accomplished by using Potassium hexacyanoferrate(III) (Sigma-Aldrich, St. Louis, USA) as an oxidant. A stock solution of 100 mM oxidant in 100 mM Tris at pH 8 was added to the RC-LH1 solution until the desired final concentration in the sample was achieved.

4.2.3. Experimental Setup and Protocol

For time-resolved measurements the experimental setup as described in sections 3.1.2 and 3.1.3 was used. The streak-camera was operated in single sweep mode with a time window of 2 ns. The transients from RC-LH1 were recorded upon excitation at 879 nm as a function of the photon fluence (number of photons per pulse per area) using repetition rates of 81 MHz, 8.1 MHz, 810 kHz and 81 kHz, respectively. For each repetition rate the photon fluence was varied in steps of $\sqrt{10}$ between 10^{10} (81 MHz and 8.1 MHz), 10^{11} (810 kHz) or 10^{12} (81 kHz) photons/(pulse·cm^2), respectively, as lower limits and 10^{14} photons/(pulse·cm^2) for all repetition rates as upper limit. These limits were determined either by the constraint to limit the integration time of the signal

to less than four hours, or in order to stay just below the threshold where statistically more than one photon per pulse is absorbed by one RC-LH1 complex (given an absorption cross section of $1.43 \cdot 10^{-14}$ cm² at 879 nm [116]).

For ease of comparison all transients are presented on a normalized scale such that 1 corresponds to the maximum of the respective transient and 0 to the averaged background level. In order to control the integrity of the RC-LH1 samples we recorded an absorption spectrum before and after the streak experiment using a commercial UV-Vis spectrometer (see section 3.3). For none of the excitation conditions we found significant bleaching or an irreversible damage of the sample.

4.2.4. Computational Setup

Simulations of the energy and electron transfer in RC-LH1 complexes were conducted by Mr. Lars Müller at the workgroup of Prof. G. Matthias Ullmann at the University of Bayreuth. The model description presented later on was developed in close cooperation between Mr. Müller and the author. For reasons of clarity, a brief overview of the computational simulations shall be given here.

To simulate the energy and transfer dynamics in isolated RC-LH1 complexes, a microstate description was used [117]. We define a microstate as the tuple of a LH state and a RC state. For an empty LH1 ring the respective LH state alone corresponds to a microstate. More details will be outlined in the description of the model (see section 4.4.1). A master equation approach was chosen to compute the relative population of each individual microstate as a function of time [118].

In order to mimic the rotating cuvette used in the experiments, the simulation was split into a part outside and a part inside the laser focus (see Figure 4.4). Inside the laser focus, the excitation probability during each laser pulse was set to the product of the absorption cross-section ($1.43 \cdot 10^{-14}$ cm² at 879 nm [116]) and the excitation fluence. As we exclude the possibility of multiple excitations on one LH1 ring during the same pulse (see section 4.4.1 for details), excitation probabilities exceeding one were set to

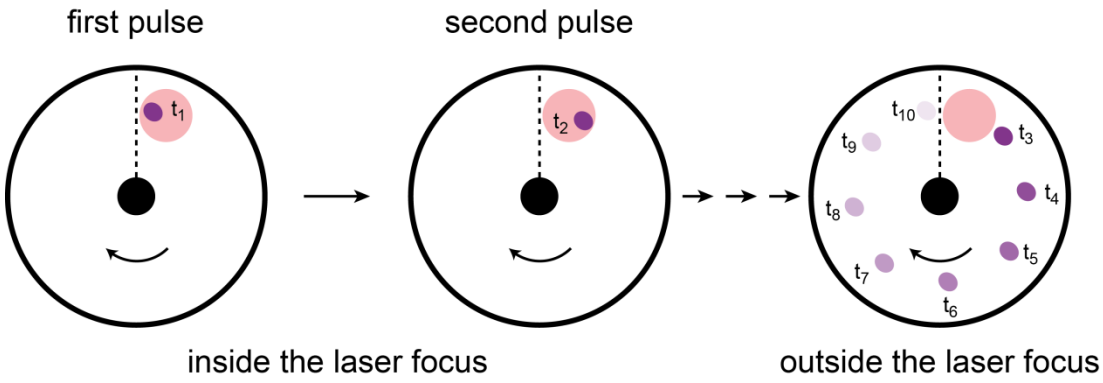

Figure 4.4: Pictorial representation of one revolution of the rotating cuvette for the example of a repetition rate of 81 kHz. The laser focus is indicated by the red shaded area and the purple ellipses refer to the RC-LH1 complexes (not to scale). The complexes can be excited by multiple laser pulses during the rotation of the cuvette through the focus (here at t_1 and/or t_2) and evolve between the laser pulses as well as between transitions through the focus (here from t_3 until t_{10}). The decay of the excited states during the rotation of the cuvette is indicated by the fading colour of the RC-LH1 complexes. Adapted from [45].

unity. In accordance with the experimental conditions, the system was exposed to 2, 21, 208 and 2080 consecutive pulses for repetition rates of 81 kHz, 810 kHz, 8.1 MHz and 81 MHz, respectively. After excitation, each energy and electron transfer step was described by a transition between the respective microstates. Outside the laser focus, where no excitation occurs, the time evolution of the system was calculated by solving the master equation.

To obtain simulated fluorescence transients, we recorded the photon count rate as a function of time for all those states that contain a deexcitation from $|2_{LH}\rangle$ to $|1_{LH}\rangle$ or a deexcitation from $|4_{LH}\rangle$ to $|3_{LH}\rangle$ (*vide infra*). We obtained the total photon count rate n_{fluo} by summing the products of the occupation probability $P_v(t)$ of the corresponding fluorescent microstates with the respective fluorescence rate k_v:

$$n_{fluo}(t) = \sum_{v=1}^{M} k_v P_v(t). \qquad 4.1$$

To avoid an artefact caused by the initial phase of the simulations, we monitored the populations of the system's microstates at the end of each revolution of the rotating cuvette. In the initial phase of the simulation, these populations vary strongly as a

function of the number of revolutions that have already passed, while in a later phase these populations converge towards fixed values. For the reported simulated fluorescence transients, we only considered the revolution after convergence of the populations and discarded those from the initial phase.

4.3. Results & Discussion: Experimental

4.3.1. Fluorescence Transients without Chemical Manipulation

The fluorescence decays of isolated RC-LH1 complexes were registered as a function of both the photon fluence and the repetition rate of the laser. The observed transients are displayed in Figure 4.5 (black dots) together with the results from master equation simulations that will be discussed later. The data in each column of the figure correspond to a distinct repetition rate that decreases from left to right. Within each column the photon fluence (given in units of photons/(pulse·cm^2)) increases from top to bottom. The transients are arranged such that within each row the continuous wave (cw) equivalent of the excitation intensity (number of photons/(time·area)) is constant, *i.e.* the product of the photon fluence and the repetition rate is the same along a row.

As a starting point for the analysis, the transients were fitted as a superposition of three exponential decays. For a fixed repetition rate the decay times were treated as global parameters and only the amplitudes of the three contributions were allowed to vary. The general picture that emerges from this approach is as follows: At low fluences the transients can be described as biexponentials (40 ps, 600 ps), at intermediate fluences as triexponentials (40 ps, 200 ps, 600 ps), and at high fluences again as biexponentials (200 ps, 600 ps). Thereby, the amplitude of the 200 ps component grows for increasing fluences, whereas that of the 40 ps component decreases at the same time, until it becomes undetectable small at the highest fluence applied. The amplitude of the slow component does not depend significantly on the fluence.

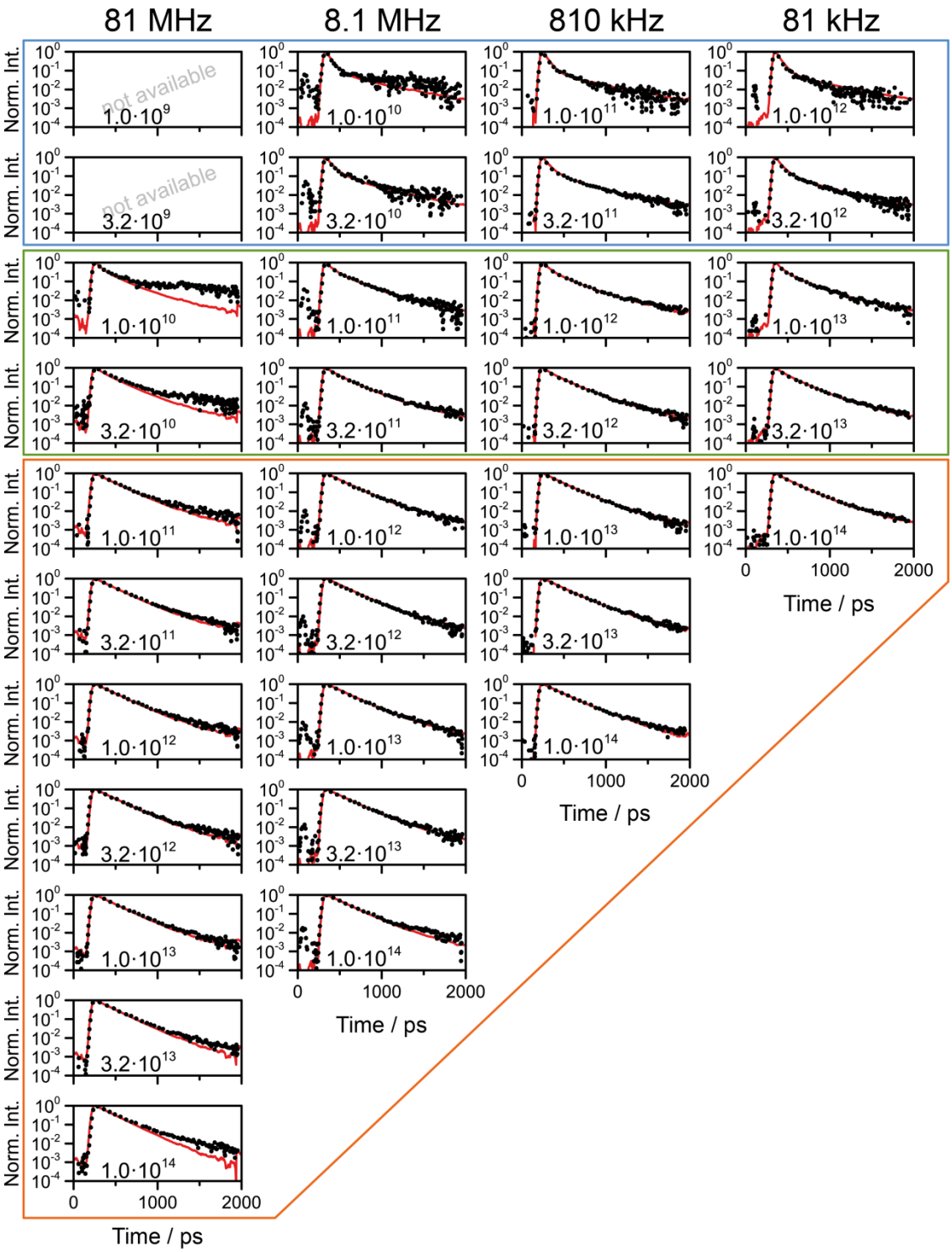

Figure 4.5: Semi-logarithmic plots of the normalized fluorescence decays (black dots) of isolated RC-LH1 complexes in detergent solution as a function of the repetition rate (columns) and the photon fluence (rows) of the excitation together with simulated fluorescence decays (red lines). →

The repetition rate decreases from left to right, and the photon fluence, which is given in units of photons/(pulse·cm²) within each graph, increases from top to bottom. Within each row the cw equivalent excitation intensity is constant. The coloured boxes indicate the range of excitation parameters for which we find from the simulations that the majority of RC-LH1 complexes is in an open state P (more than 81 % open RCs, blue box), where RCs in the open and closed state P and P^+ coexist (20-80 % open RCs, green box) and where RCs in the closed state P^+ dominate (below 20 % open RCs, orange box). Figure from [45].

It is interesting to note that within experimental error the transients that were measured with the same equivalent cw excitation intensity yield identical results with the fits. Deviations of the amplitudes from this scheme are only observable for the highest repetition rate of 81 MHz. At that rate we find for both, the lowest and the highest fluence, that the amplitude of the slowest decay component is enhanced with respect to what has been found at the other repetition rates.

Upon electronic excitation of the special pair a sequence of electron transfers is initiated leaving behind a positively charged special pair P^+. For excitation rates that are higher than the inverse of the recovery time of the RC, which amounts to about 100 ms, it is known that the sample accumulates a mixture of RC-LH1 complexes with open (P) and closed (P^+) RCs after a few excitation cycles [104–107,112,119]. Therefore we tentatively attribute the 40 ps and 200 ps components to reflect the fractions of RCs in the open and closed state, respectively, which is in qualitative agreement with the changes of the corresponding amplitudes as a function of the excitation rate. Moreover, since the amplitude of the slow component does not depend significantly on the excitation rate, it is possible to associate the 600 ps component with a residual population of "empty" LH1 rings that might reflect a consequence of the extraction procedure. This conjecture is in line with the fact that the observed lifetime is in close agreement with the 650 ps decay time that has been found for chromatophores of a mutant without RCs [109].

4.3.2. Fluorescence Transients under Chemical Manipulation

In order to test the influence of the redox state of the RC on the dynamics of the fluorescence decays we performed two control experiments. For the first one, the RC

was chemically reduced to shift the steady-state population of the RCs to the open state P. This experiment had to be conducted on a newly prepared batch of RC-LH1 complexes that were grown and purified following the same protocol as before. For these complexes the fraction of the long-lived component was enhanced with respect to the previous sample. The general variation of the populations as a function of the excitation conditions, however, was the same as described above.

This sample was illuminated with a fluence of 10^{14} photons/(pulse·cm²) at a repetition rate of 810 kHz, while the reducing agent DAD was added to the sample up to a final concentration of 1 mM. At the given fluence and repetition rate, the RCs are supposed to reside in the closed state, as long as no DAD is present in the sample. Examples of the corresponding fluorescence decays are shown in Figure 4.6a for DAD concentrations of 0 µM (orange line), 1 µM (green line) and 100 µM (blue line). The transient recorded in the absence of any reducing agent shows a biexponential decay with time constants of 200 ps and 600 ps (Figure 4.6a orange line). Upon increasing the concentration of DAD a further decay component with a time constant of 40 ps grows

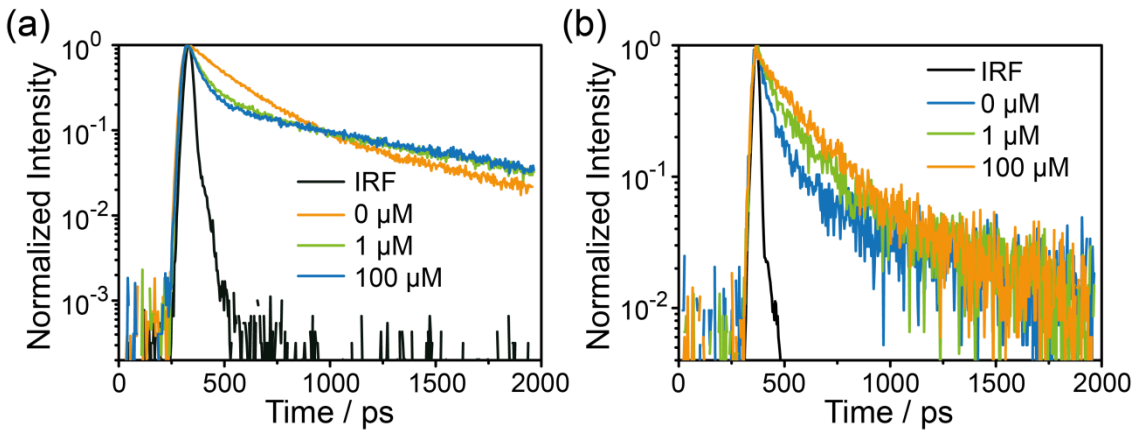

Figure 4.6: Normalized fluorescence decays of isolated RC-LH1 complexes in detergent solution a) for a repetition rate of 810 kHz and a fluence of 10^{14} photons/(pulse·cm²) as a function of the diaminodurene (DAD) concentration (coloured curves), b) for a repetition rate of 8.1 MHz and a fluence of $3.2 \cdot 10^{10}$ photons/(pulse·cm²) as a function of the potassium hexacyanoferrate(III) ($K_3Fe(CN)_6$) concentration (coloured curves). The black curves in both graphs refer to the instrument response and both have a width of 50 ps (FWHM). Figure adapted from [45].

in, whereas at the same time the amplitude of the 200 ps component decreases and finally vanishes at a DAD concentration of 100 µM. For even higher DAD concentrations no further changes of the transients could be detected. During the whole sequence of experiments the amplitude of the 600 ps component did not change significantly.

For the second control experiment the RC was chemically oxidized and the steady-state population of the RCs was shifted towards the closed state P^+. The sample was illuminated with a fluence of $3.2 \cdot 10^{10}$ photons/(pulse·cm²) at a repetition rate of 8.1 MHz, while the oxidizing agent $K_3Fe(CN)_6$ was added to the sample up to a final concentration of 1 mM. The excitation parameters were chosen such as to keep the majority of the RCs in the open state as long as no $K_3Fe(CN)_6$ is present in the sample. The higher repetition rate of 8.1 MHz compared to the previous control experiment was chosen to keep the integration time for each transient at about one hour. Examples of the corresponding fluorescence decays are shown in Figure 4.6b for oxidant concentrations of 0 µM (blue line), 1 µM (green line) and 100 µM (orange line). The transient recorded in the absence of the oxidizing agent (Figure 4.6b, blue line) shows a triexponential decay with time constants of 40 ps, 200 ps and 600 ps, where the amplitude of the 200 ps component is very small. Adding the oxidant results in an increase of the amplitude of the 200 ps component at the expense of the amplitude of the 40 ps component (Figure 4.6b, green line) until the latter becomes undetectable at a concentration of 100 µM. As before the amplitude of the 600 ps component does not change significantly as a function of the $K_3Fe(CN)_6$ concentration. We note that we observe a strong quenching of the RC-LH1 fluorescence as well as a bleaching of the B875 absorption band for $K_3Fe(CN)_6$ concentrations above 100 µM, which is likely to be caused by an oxidation and concomitant destruction of the LH1 ring as has been found before [120].

Apparently, the increase of the concentration of the reducing agent, *i.e.* shifting the steady state population of the RCs to the neutral state P (RC open), has qualitatively the same effect (increase of the 40 ps component; decrease of the 200 ps component) as

decreasing the excitation rate for an unmanipulated sample. *Vice versa*, increasing the concentration of the oxidant, *i.e.* shifting the steady-state populations of the special pairs towards the P+ state (RC closed) has the same effect (decrease of the 40 ps component; increase of the 200 ps component) as increasing the excitation rate for an unmanipulated sample. These similarities support the association of the three observed decay components with pigment-protein complexes that have the RC in the open state (40 ps) or in the closed state (200 ps), and those that feature an "empty" LH1 ring (600 ps).

4.4. Results & Discussion: Simulations

4.4.1. Model for RC-LH1

The DDM concentration in our samples is about 0.4 mM, which is above the critical micellar concentration of 0.17 mM at 25 °C for this detergent. Therefore, we consider the sample to consist of non-aggregated RC-LH1 complexes that do not interact with each other, and we exclude intercomplex energy transfer. In order to obtain a more quantitative understanding of the processes that take place in the RC-LH1 complexes upon photoexcitation we performed simulations based on a master equation approach. The computational details are explained in section 4.2.4.

The “Empty” LH1-Ring

As a starting point for the modelling, we resort to the same concept that has been used to obtain a quantitative description of the dynamics of the photophysical processes in non-aggregated LH2 complexes [114]. The basic idea of this approach was to treat the LH2 as a multichromophoric system that can carry more than one electronic excitation at the same time. Because there was no need to specify the exact size of the assembly, we will use an equivalent approach for modelling the fraction of "empty" LH1 rings.

In Figure 4.7, we use a pictorial representation of the electronic states of a non-aggregated LH1 ring that has been proven to be very useful in the past [114,115]. The LH1 ring in the various states is represented by coloured spheres that are connected by transitions that have specific rates k_{ij}. A LH1 ring in the electronic singlet ground state is represented by a green sphere. For brevity, we refer to this state as $|1_{LH}\rangle = |{}^1B875, {}^1Car\rangle$. Upon excitation into the B875 band, there will be a fast equilibration within the exciton states, which is beyond the time resolution of our experiment, and we therefore treat the ^{1}B875* excited state as an effective level. In Figure 4.7 this state is visualized by a red sphere with an ellipse and is referred to as $|2_{LH}\rangle = |{}^1B875^*, {}^1Car\rangle$. Under high-illumination conditions, it becomes possible to create two excited ^{1}B875* states in the same RC-LH1 complex, giving rise to singlet-singlet annihilation (SSA). In earlier studies on RC-LH1-only chromatophores or LH2 samples of mM concentrations, it has been found that fluences above $3 \cdot 10^{14}$ photons/(pulse·cm²) are required to have more than one singlet state on an individual light-harvesting complex [37,121]. However, in those chromatophore samples the possible intercomplex energy transfer increases the probability by orders of magnitude that a LH complex receives a second excitation [115]. Although the highest fluence used in our work is close to the threshold given above, we rule out the

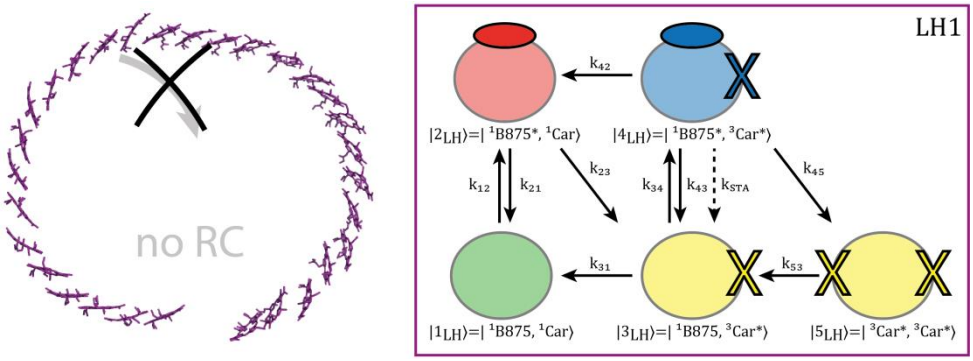

Figure 4.7: Pictorial representation of the transitions between the electronic states of an isolated LH1 ring without RC. The coloured spheres represent the B875 pigment pool of LH1 in different electronic states, where ellipses correspond to singlet excitations and crosses to triplet excitations. Singlet-triplet annihilation (STA) is taken into account. For more details see text. Figure from [45].

possibility of SSA, because we work at nM concentrations, what excludes populating the $|2_{LH}\rangle$ state by intercomplex energy transfer.

From the $|2_{LH}\rangle$ state the system can decay back to the ground state or cross over within 10 ns to the triplet state $|\,^3B875^*,\,^1Car\rangle$, which is quenched by the carotenoids with a rate of $(10\text{ ns})^{-1}$ [122] resulting in the state $|3_{LH}\rangle = |\,^1B875,\,^3Car^*\rangle$. This state is displayed in Figure 4.7 as a yellow sphere with a cross that symbolises a LH1 ring that carries a triplet state on one of the carotenoids. In the following, the transition from $|2_{LH}\rangle$ to $|3_{LH}\rangle$ will be described by an effective rate that amounts to $(20\text{ ns})^{-1}$. In RC-LH1 complexes that contain spirilloxanthin as carotenoids the subsequent decay of the carotenoid triplet state occurs with a time constant between 1.6 and 2.9 µs [123,124].

Singlet-triplet annihilation (STA) becomes possible if a LH1 ring that still carries a triplet state (cross in Figure 4.7) gets excited again to the ^{1}B875* state (ellipse in Figure 4.7). This situation is depicted by a circle with both a cross and an ellipse and will be referred to as $|4_{LH}\rangle = |\,^1B875^*,\,^3Car^*\rangle$, Figure 4.7 blue sphere. However, since LH1 is a multichromophoric system, it is also possible that a LH1 ring that is in state $|4_{LH}\rangle$ decays with a rate k_{45} to a state $|5_{LH}\rangle = |\,^3Car^*,\,^3Car^*\rangle$ having two triplet states on different carotenoids. Since it is known from ESR experiments that the triplet states on the carotenoids are immobile [125], and because triplet-triplet energy transfer is mediated by the short-range exchange interaction, we neglect triplet-triplet annihilation in our analysis. However, for state $|4_{LH}\rangle$ we do take into account the additional decay channel to state $|5_{LH}\rangle$. The numerical values for the rates that are required for a quantitative modelling have been taken either from the literature, the current study, or from the previous study on LH2 and are summarized in Table 4.1 together with the corresponding references.

Open Reaction Centre

For modelling the RC-LH1 complexes that contain a RC we start the description with those complexes that feature an open RC. In addition to the processes that occur within the LH1 ring, and which have been described above, we have to take into account the

Table 4.1: Input parameters for the simulations that are associated with LH1. From [45].

LH1			
parameter	type	value	reference
σ_{B875}	absorption cross section ^{1}B875	$1.43 \cdot 10^{-14}$ cm²	[116]
k_{12}	excitation rate ^{1}B875	$\sigma_{B875} \cdot J_{ex}$	
k_{21}	singlet decay ^{1}B875*	$(600\ \text{ps})^{-1}$	this work
k_{23}	intersystem crossing to ^{3}Car*	$(20\ \text{ns})^{-1}$	[122]
k_{31}	triplet decay from ^{3}Car*	$(1.6\ \mu\text{s})^{-1}$	[123]
k_{34}	excitation rate ^{1}B875	$= k_{12}$	
k_{43}	singlet decay ^{1}B875*	$= k_{21}$	this work
k_{STA}	singlet triplet annihilation	$(5.56\ \text{ns})^{-1}$	[114]
k_{42}	triplet decay from ^{3}Car*	$= k_{31}$	
k_{45}	intersystem crossing to ^{3}Car*	$= k_{23}$	
k_{53}	triplet decay from ^{3}Car*	$= 2 \cdot k_{31}$	
k_{open}	transfer ^{1}B875* to P	$(40\ \text{ps})^{-1}$	this work
k_{back}	transfer P* to ^{1}B875	$(8\ \text{ps})^{-1}$	[106]
k_{closed}	transfer ^{1}B875* to P$^+$	$(300\ \text{ps})^{-1}$	this work

photophysical and photochemical processes that take place in the RC after the photoexcitation. In order to avoid confusion, electronic states that are associated with the LH1 ring are indexed as "LH", whereas those that are associated with the RC are indexed as "RC". For the sake of brevity, the RC is depicted at the bottom of Figure 4.8 with the pigments of the A-branch (diamonds), only. We do not consider direct excitation of the special pair by the laser because of its low absorption cross section compared with that of the B875 pigment pool at the wavelength used.

In our nomenclature, transfer of excitation energy from the LH1 ring to the RC can occur from the states $|2_{LH}\rangle$ and $|4_{LH}\rangle$. The time constant for this processes is 40 ps and induces the transition of the RC from the ground state $|1_{RC}\rangle = |P,\ B_A,\ H_A,\ Q_A\rangle$ to a state with the special pair in the excited state $|2_{RC}\rangle = |P^*,\ B_A,\ H_A,\ Q_A\rangle$ (see Figure 4.8a, blue box). Back transfer from state $|2_{RC}\rangle$ to the LH1 has been observed and occurs with a time constant of 8 ps [98,99,106]. Alternatively, the excitation of the special pair initiates an electron transfer chain via the accessory BChl B_A ($|3_{RC}\rangle =$

$|P^+, B_A^-, H_A, Q_A\rangle$) and the BPhe H_A ($|4_{RC}\rangle = |P^+, B_A, H_A^-, Q_A\rangle$) to a ubiquinone molecule Q_A ($|5_{RC}\rangle = |P^+, B_A, H_A, Q_A^-\rangle$), where the charge-separated state is stabilized [13]. The time constants for the electron transfer to states $|3_{RC}\rangle$, $|4_{RC}\rangle$ and $|5_{RC}\rangle$ are 3, 0.9 and 200 ps, respectively.

In vivo the charge stabilized on Q_A^- would be transferred within about 100 µs [126] to a second ubiquinone molecule Q_B. This molecule is loosely bound to the RC protein

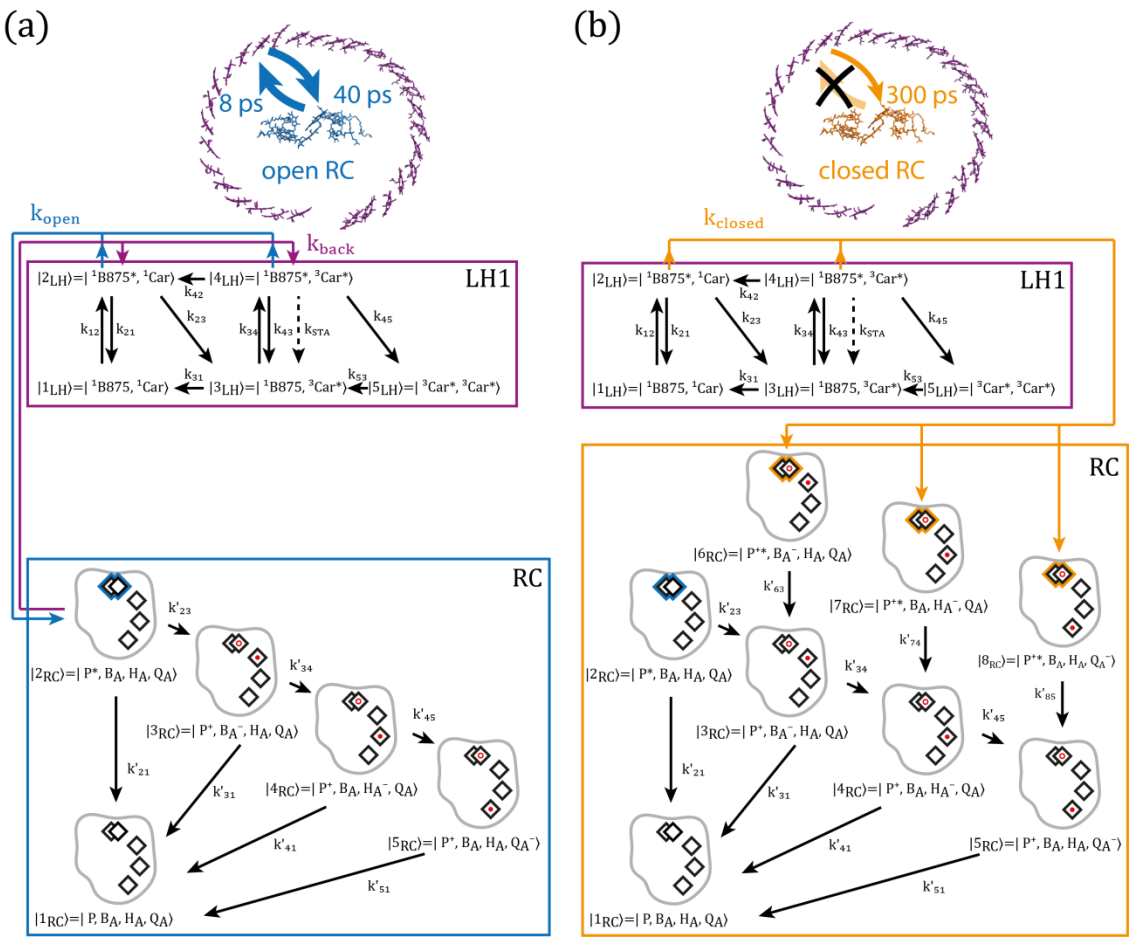

Figure 4.8: Pictorial representation of the energy and electron transfer dynamics in RC-LH1 complexes with open (a) or closed (b) RCs. The top boxes refer to the description of empty LH1 rings as in Figure 4.7. The lower boxes refer to the description of the RCs. In the RC, the cofactors are shown as diamonds for one branch only. An electronic excitation is indicated by a coloured halo, and oxidized (reduced) states are represented by an open (closed) dot. Figure from [45].

matrix and often lost during the purification process. From test simulations we learned that the presence (or lack) of Q_B in the RCs has only a minor influence on the fluorescence transients (see Appendix A, Figure A.1), and was therefore neglected in this study. Relaxation from the states $|2_{RC}\rangle$, $|3_{RC}\rangle$ $|4_{RC}\rangle$ and $|5_{RC}\rangle$ to the ground state $|1_{RC}\rangle$ occurs with time constants of 180 ps, 200 ps, 10 ns and 100 ms, respectively [127–129].

The rates of the transitions between the five states associated with the RC are denoted with k_{ij}' in the blue box in Figure 4.8a and are summarized in Table 4.2. We have also neglected the transition of the radical pair $^1(P^+, H_A^-)$ to the triplet state $^3(P^+, H_A^-)$, because this conversion occurs only in RCs without Q_A and at very high illumination intensities, which are both not the case here.

Closed Reaction Centre

First, it is important to note that the definition of a closed RC is not uniform in the literature. Here, we refer to the RC as being in the closed state if the special pair is in the oxidized state P^+. As has been demonstrated before the P^+ state can still act as an acceptor for the excitation energy from LH1, yet at a reduced energy transfer

Table 4.2: Input parameters for the simulations that are associated with the RC. From [45].

	RC		
parameter	type	value	reference
k_{21}'	singlet decay P*	$(180\ \text{ps})^{-1}$	[128]
k_{23}'	charge separation to (P^+,B_A^-)	$(3\ \text{ps})^{-1}$	[13]
k_{31}'	charge recombination to P	$(200\ \text{ps})^{-1}$	[129]
k_{34}'	charge separation to (P^+,H_A^-)	$(0.9\ \text{ps})^{-1}$	[13]
k_{41}'	charge recombination to P	$(10\ \text{ns})^{-1}$	[127]
k_{45}'	charge separation to (P^+,Q_A^-)	$(200\ \text{ps})^{-1}$	[13]
k_{51}'	charge recombination to P	$(100\ \text{ms})^{-1}$	[127]
k_{63}'	singlet decay P^+*	∞	see text
k_{74}'	singlet decay P^+*	∞	see text
k_{85}'	singlet decay P^+*	∞	see text

rate [106,107,130].

For the description of RC-LH1 complexes with a closed RC, we resort on the details described above and extend the RC model by three states. These correspond to a situation where P is oxidized, but resides in an excited state P^{+}*, and either B_A, H_A or Q_A is in the reduced state. These states are denoted as $|6_{RC}\rangle = |P^{+*}, B_A^-, H_A, Q_A\rangle$, $|7_{RC}\rangle = |P^{+*}, B_A, H_A^-, Q_A\rangle$ and $|8_{RC}\rangle = |P^{+*}, B_A, H_A, Q_A^-\rangle$ (see Figure 4.8b, orange box), and the corresponding energy transfer rates from $|2_{LH}\rangle$ or $|4_{LH}\rangle$ to either of these states are referred to as k_{closed}. A numerical value for this rate can be obtained from the measured decay time of 200 ps for this case. Using

$$k_{meas} = (200\,ps)^{-1} = k_{21} + k_{closed} + k_{23} \approx k_{21} + k_{closed}, \qquad 4.2$$

with $k_{21} = (600\,ps)^{-1}$ eventually yields $k_{closed} = (300\,ps)^{-1}$.

Unfortunately, little is known about the exact decay process of the P^{+}* state, yet it is conceivable that the relaxation from P^{+}* to the P^{+} ground state is beyond the temporal resolution of our experiment [130]. Therefore we have modelled the transitions from $|6_{RC}\rangle$ to $|3_{RC}\rangle$, from $|7_{RC}\rangle$ to $|4_{RC}\rangle$, and from $|8_{RC}\rangle$ to $|5_{RC}\rangle$ as instantaneous and do not consider back transfer of the excitation to the LH1 ring from these states. The rates used for the simulations for a closed RC are also summarized in Table 4.2.

Further Parameters

In addition to the parameters summarized in the tables, we have to specify the fraction of pigment-protein complexes that carry no RC, as well as the fraction of RC-LH1 complexes that freshly enter the laser focus during the revolution of the rotating cuvette that contains the sample.

The first parameter can be estimated from the relative amplitude of the slow decay component, and we find satisfactory agreement between the simulations and the whole data set of 30 transients only if this value is kept in a range of (3±2) % (see Appendix A, Figure A.2). The fraction of fresh sample that enters the focus was estimated to be 25 %. This parameter can be varied between 25 % and 50 % yielding minor but visible

deviations between the measured and simulated decay curves (see Appendix A, Figure A.3). The remaining fraction of RC-LH1 complexes was treated as having been already exposed to the laser during the previous passage. All transients were then simulated simultaneously using a Master equation approach (see also section 4.2.4).

4.4.2. Results of the Simulations

The simulated curves that were obtained using the formalism described above are shown in Figure 4.5 as red lines. The overall agreement between the measured and the simulated transients is striking, in particular, as no free parameters for the fitting of individual decays have been used. Rather we applied one global model to describe all the curves simultaneously.

For the lowest three repetition rates, 81 kHz, 810 kHz, and 8.1 MHz, there is only a small but observable deviation of the simulated decay from the experimentally observed one for the lowest fluence at 8.1 MHz. For this parameter setting, the photon counting rate (and concomitantly the signal-to-noise ratio) is rather low, which might cause an artefact when the transient is normalized for comparison.

At the highest repetition rate of 81 MHz a very good agreement between simulation and experiment can be found but only for fluences between 10^{11} photons/(pulse·cm²) and $3.2 \cdot 10^{13}$ photons/(pulse·cm²). For the two lowest fluences, the simulated transients show a significantly faster decay than the experimentally observed ones, and also for the highest fluence, an observable albeit not dramatic difference between simulation and experiment is apparent at longer times. These discrepancies reflect a stronger contribution of the fraction of LH1 without RC at the lowest and highest fluences, when the time interval between two succeeding laser pulses decreases from about 120 ns to 12 ns (corresponding to repetition rates of 8.1 and 81 MHz, respectively).

On first sight this observation seems to indicate the involvement of long-lived triplet states and concomitant STA. However, this process is already included in the simulations and we find a nearly perfect match between experiment and simulation at

the other repetition rates where STA is also relevant. In order to find another explanation for the deviations between the simulated and experimentally observed transients at 81 MHz, we performed further test simulations. First we adjusted the fraction of complexes without RC such that simulation and experiment matched for 10^{10} photons/(pulse·cm²) at 81 MHz. However, this resulted in a strong mismatch between the calculated and observed transients at all other repetition rates. Secondly, we considered the possibility of SSA, which was not taken into account for the simulations. Since for the highest repetition rate of 81 MHz the temporal separation between two consecutive laser pulses already exceeds the fluorescence lifetime by more than a factor of ten this requires the creation of two $^1B875^*$ excitations within a single laser pulse. This effect then, should solely depend on the fluence and not on the applied repetition rate. However, such a deviation between experiment and simulation is not observable at the highest fluences at repetition rates other than 81 MHz, which excludes this option as well.

Nevertheless, for most of the combinations of fluence and repetition rate the model used for the simulations predicts dynamics of RC-LH1 that are in excellent agreement with the experiments. Therefore, we used this model to extract the relative number of LH1 complexes that carry a triplet state as well as the fraction of RC-LH1 complexes with a closed RC as a function of the excitation parameters.

The relative steady-state triplet population (the relative number of RC-LH1 complexes that carry at least one triplet state) is shown in Figure 4.9a as a function of the fluence for the applied repetition rates. Expectedly, this fraction is zero for all fluences at the repetition rate of 81 kHz as the time delay between two successive pulses of about 12 µs exceeds the lifetime of the triplet state by at least a factor of five. For the other three repetition rates the fraction of RC-LH1 complexes that carry $^3Car^*$ states on the LH1 ring increases by several orders of magnitude with increasing fluence, see Figure 4.9a. Representing the same data as a function of the repetition rate for the cw equivalent excitation intensities, Figure 4.9b, reveals for all intensities an increase of the triplet population for rising the repetition rate from 810 kHz to 8.1 MHz, that levels

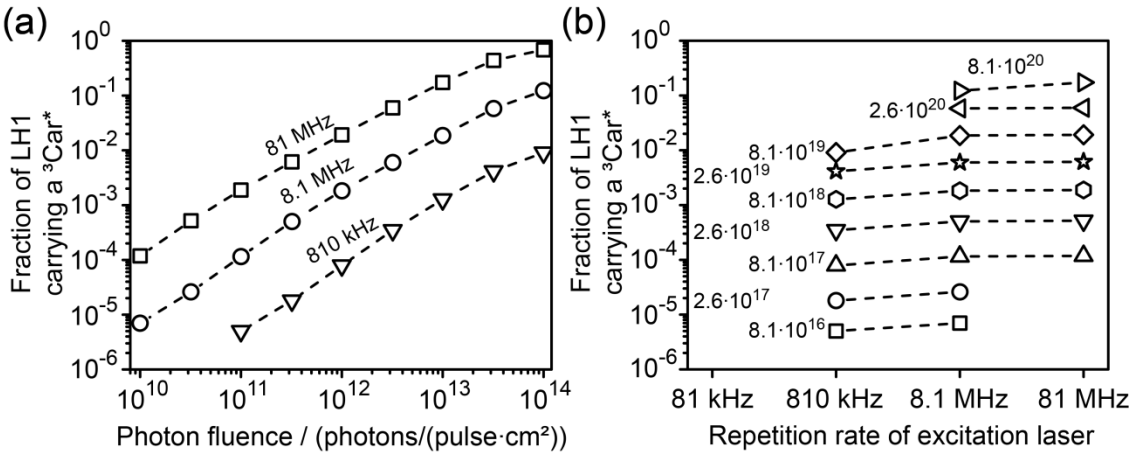

Figure 4.9: Simulated fraction of RC-LH1 complexes that carry at least one triplet excitation on the LH1 ring ($^3Car^*$) a) as a function of the fluence and b) as a function of the repetition rate. The lines serve as a guide for the eye and connect data points of equal repetition rate (a) or equal cw equivalent excitation intensity (b), given in photons/(s·cm²). Figure adapted from [45].

off for a further increase of the repetition to 81 MHz. Apparently the pulse separation at 8.1 MHz of 120 ns is already so much faster than the triplet decay time of a few µs that a further increase of the repetition rate has only a negligible influence on the steady-state triplet population, see also Table A.1 in Appendix A.

The calculated steady-state fraction of RC-LH1 complexes with a closed RC, *i.e.* a RC with a P^+ state, is shown in Figure 4.10a as a function of the fluence for the four repetition rates. For the three smaller repetition rates the fraction of closed RCs is about 6 % at low fluence and rises towards 97 % at higher fluences (in our model this corresponds to all complexes that carry a RC). Yet, the onset of this rise occurs the earlier the higher the repetition rate, and in particular at 81 MHz the fraction of closed RCs is already about 40 % at the lowest fluence applied before it converges towards 97 % at increasing fluences. Plotting the same data as a function of the repetition rate for the cw equivalent excitation intensities, Figure 4.10b, allows us to identify three ranges:

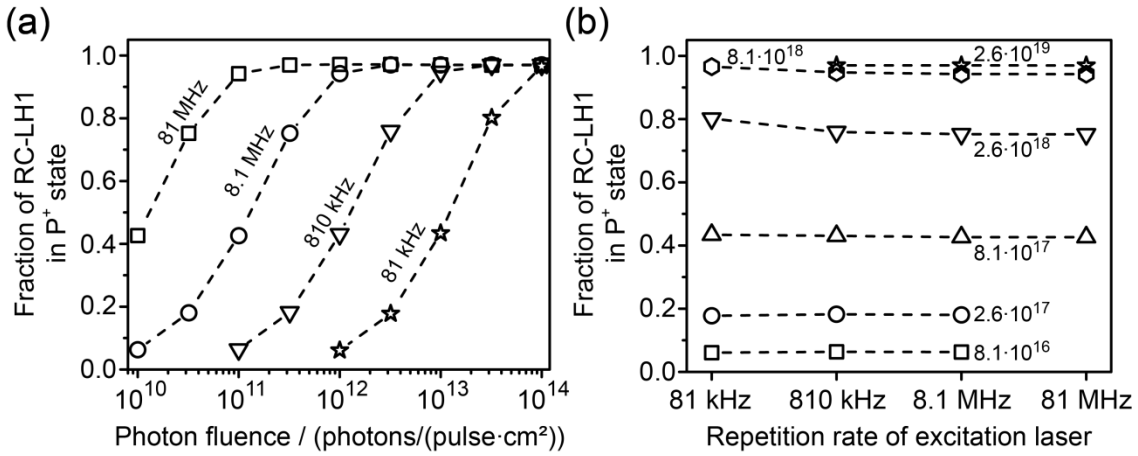

Figure 4.10: Simulated fraction of RC-LH1 complexes with an oxidized special pair (P^+) a) as a function of the fluence and b) as a function of the repetition rate. The lines serve as a guide for the eye and connect data points of equal repetition rate (a) or equal cw equivalent excitation intensity (b), given in photons/(s·cm²). Figure adapted from [45].

i. For cw equivalent excitation intensities of $8.1 \cdot 10^{17}$ photons/(s·cm²) and below, the fraction of RC-LH1 complexes with a special pair in the P^+ state does not depend on the repetition rate.

ii. At cw equivalent excitation intensities between $2.6 \cdot 10^{18}$ and $8.1 \cdot 10^{18}$ photons/(s·cm²) we find a slight decrease of the P^+ population for an increase of the repetition from 81 kHz to 810 kHz levelling off for a further increase of the repetition rate.

iii. At the highest shown cw equivalent excitation intensity of $2.6 \cdot 10^{19}$ photons/(s·cm²), all RC-LH1 complexes have their special pair in the P^+ state irrespective of the repetition rate.

The relative decrease of the P^+ population between 81 kHz and 810 kHz at elevated cw equivalent excitation intensities can be rationalised as follows. Only at repetition rates higher than 810 kHz do we find a significant steady-state triplet population. If for these rates the excitation intensity is sufficiently large to have a singlet and a triplet state on the same LH1 ring, STA occurs. As a consequence the number of excitations that can be transferred to the RC is reduced, which in turn also reduces the population of closed

RCs. The threshold for the onset of this effect can be deduced from Figure 4.10b. For excitation intensities up to $8.1 \cdot 10^{17}$ photons/(s·cm²) the relative triplet population is about 10^{-4} (see Figure 4.9a and Table A.1, Appendix A), which is too small to make a significant impact via STA on the P^+ population. On the other hand, for cw excitation intensities above $8.1 \cdot 10^{18}$ photons/(s·cm²), STA cannot outcompete the rapid build-up of the P^+ population, so that the latter one saturates. Hence the influence of STA on the P^+ population is only significant for cw excitation intensities between $8.1 \cdot 10^{17}$ photons/(s·cm²) and $8.1 \cdot 10^{18}$ photons/(s·cm²). Interestingly, this corresponds to a relative triplet population in the order of 10^{-3} - 10^{-4} per LH1-ring (see Figure 4.9a and Table A.1, Appendix A), which already makes a detectable impact on the fluorescence decay of isolated RC-LH1 complexes.

4.5. Conclusion

In the study at hand, we investigated the fluorescence decay of isolated RC-LH1 complexes from *Rhodopseudomonas palustris* on a ps time scale. The fluorescence transients were recorded as a function of the photon fluence and the repetition rate of the excitation laser, both of which have been varied over several orders of magnitude. This allowed us to identify the simultaneous presence of RC-LH1 complexes in our sample that have an open RC (special pair in the neutral state P), those that have a closed RC (special pair in the oxidized state P^+) and those that completely lack a reaction centre, featuring characteristic fluorescence lifetimes of 40, 200 and 600 ps, respectively. These findings were corroborated by control experiments with reducing or oxidizing agents. For a quantitative analysis of the data we performed elaborate simulations using a global master equation approach based on a microstate description of RC-LH1 and achieved very good agreement between the simulated and the measured transients. This model allows us to predict the relative population triplet states on LH1 ($^3Car^*$) as well as the fraction of closed RCs (P^+) as functions of the photon fluence and the repetition rate of the excitation.

Moreover RC-LH1 gives a good example of a modular, but highly optimized natural building block. With only a small number of pigments, Nature has evolved a highly complex structure that is capable to react to a wide range of light intensities only by its intrinsic energy and electron transfer properties. Through the transition from a neutral to an oxidized special pair, the RC is able to switch the energy transfer behaviour of LH1. In the first case, LH1 will preferably transfer energy to the RC, while in the second, it will more likely redistribute energy to close lying LH complexes. Understanding these details of structure-function relationship might allow us to adapt these concepts in highly efficient and most compact molecular electronics.

5. Hybrid Nanostructures: Plasmon Enhancement of LH2 Fluorescence

The optical response of hybrid nanostructures that are made of individual light-harvesting complexes interacting with gold nanoparticles, was investigated using single molecule imaging techniques. The experiments show an enhancement of LH2 fluorescence intensities when excited within the plasmon resonance of the gold nanoparticles. No such effect is observed on excitation far off the plasmon resonance. Reference experiments and model calculations evidence the enhancement effect to be of plasmonic origin and hint towards an adsorption of LH2 to the gold nanoparticles.

Note: This chapter closely follows and in wide parts cites the publication S. R. Beyer *et al.*, "Hybrid Nanostructures for Enhanced Light-Harvesting: Plasmon Induced Increase in Fluorescence from Individual Photosynthetic Pigment-Protein Complexes", *Nano Letters*, **11**, 4897-4901 (2011) [131]. Section 5.3.1, including Figure 5.5, and the initial version of the algorithm used to extract the information shown there from the raw data were already presented in [20] and are not considered part of this thesis. They are repeated here for reasons of clarity. The remaining sections and data presented in this chapter, the analysis and discussion of the data as well as the model simulations are subject of this thesis. LH2 complexes were kindly provided by the workgroup of Prof. Richard J. Cogdell, University of Glasgow. Preparation of the complexes was conducted by Ms. June Southall. Gold nanoparticle substrates were manufactured and provided by Mr. Simon Ulrich and Dr. Stefan Kudera, Max-Planck Institute for Intelligent Systems, Stuttgart.

5.1. Introduction

The recent years saw an enormous interest in trying to mimic photosynthetic systems to collect, direct and use solar radiation [132–135]. Important issues that have to be considered when thinking of how to design such systems concern the character of the donor-acceptor materials, their chemical nature, their mutual arrangement (distance and orientation), their electronic couplings, their reorganisation energies, and the influence

of the surrounding matrix to optimize the energy- and charge-transfer properties of the supramolecular building blocks. Moreover the hierarchical organisation of individual components must be precisely controlled so that devices can cover macroscopic surface areas without loss in efficiency.

An alternative strategy is to take advantage of existing functional photosynthetic units, such as natural pigment-protein complexes, and use them as building blocks for the development of novel, biohybrid light-harvesting devices [136–139]. Arguments in favour of this strategy are that the protein matrix imposes a structural hierarchy that ensures the proper positioning of the cofactors and acts as a "smart matrix" forming a unique environment around the chromophores that promotes functionality.

In the following we will discuss a biohybrid nanostructure that is composed of a light-harvesting II complex from the photosynthetic membrane of purple bacteria (see section 4.1.1) and a gold nanoparticle.

5.1.1. Structure of Light-Harvesting Complex II

The general structural idea of LH2 is very similar to that of LH1, which was discussed in section 4.1.2. Depending on the species, LH2 consists of eight respectively nine pairs of transmembrane helices labelled α and β that form a circular arrangement (see Figure 5.1). Each α-β subunit non-covalently binds three BChl *a* molecules. Two are closely spaced with the planes of their bacteriochlorin rings being oriented perpendicular to the membrane plane. The remaining BChl *a* molecule is separated from the closely spaced pair and its bacteriochlorin ring is oriented roughly parallel to the membrane plane [11]. In the assembled LH2 complex this gives rise to two different pigment pools. One circular arrangement of nine respectively eight widely spaced BChl *a* molecules (Figure 5.1, orange) and a circular arrangement of 18, respectively 16 closely spaced BChl *a* molecules (Figure 5.1, purple) that are often compared to the look of a turbine wheel. Carotenoid molecules (Figure 5.1, green) form the third pigment pool of LH2. They insure the structural integrity of the assembled LH2 complex, as they connect each pair of neighbouring α-β subunits like a skewer and are

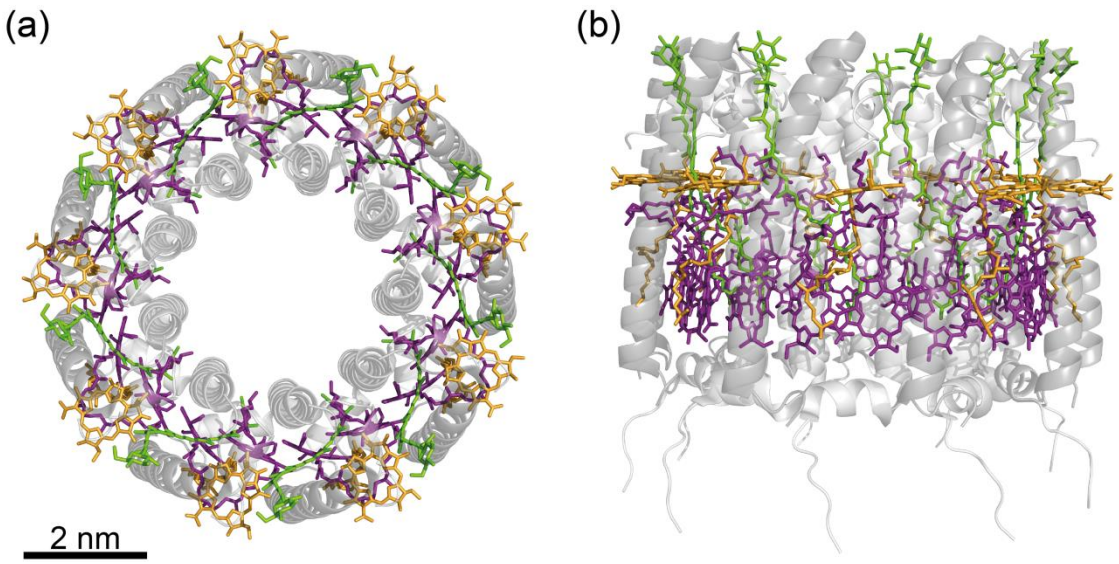

Figure 5.1: Crystal structure of LH2 from *Rps. acidophila* at a resolution of 2.0 Å. α- and β-polypeptides are depicted in light and dark grey, respectively. B850 pigments are held in purple, those of the B800 ring in orange. Carotenoids are drawn in green. a) View perpendicular to the membrane plane. b) View from within the membrane. Redrawn from PDB entry 1NKZ [14].

positioned such that they lie close to the single BChl *a* of one subunit and the pair of BChl *a* molecules of the other [14,140].

High-resolution structural information is available for the LH2 complexes of a couple of species. While an eightfold symmetry was found for LH2 from *Rhodospirillum (Rsp.) molischianum* [50], complexes with nine α-β subunits have been found in *Rhodopseudomonas (Rps.) acidophila* [14]. The LH2 complexes discussed in this chapter originate from *Rhodobacter (Rb.) sphaeroides* [141]. Up to date, their structure could not be determined with sufficient resolution, but it is highly likely that it is very similar to that of *Rps. acidophila*.

5.1.2. Function of Light-Harvesting Complex II

As described in section 4.1.1, LH2 complexes serve as an antenna for light and are also built to transfer the absorbed solar energy to further close lying light-harvesting

complexes. Thereby the two BChl *a* pigment pools described in the previous section act as the main absorbers.

The ring of nine widely spaced BChl *a* molecules can be described in terms of weak to medium coupling according to the formalism discussed in section 2.2, as the ratio $|V/\Delta E|$ has been reported to be <1 [11]. It gives rise to a room temperature absorption band that is centred around 800 nm (see Figure 5.2a) and is labelled as B800 ring. The current view is that an excitation on the B800 ring is mostly localized to the individual BChl *a* molecules, but can be delocalized over up to 2 – 3 pigments, depending on the distinct structural details of the LH2 complex under investigation. Energy migration between the pigments of the B800 band has been reported to appear with a time constant of ~1.5 ps [142,143].

The ring of 18 closely spaced BChl *a* can be described in terms of strong coupling and values for $|V/\Delta E|$ were reported to be >1 [144–146]. Due to the coupling, the room temperature absorption band of this ring is centred around 850 nm, giving rise to the term B850 ring (Figure 5.2a). We will find a system with 18 excitonic states usually labelled $k^{as} = 0, \pm 1, \dots, \pm 4$ and $k^{s} = \pm 4, \dots, \pm 1, 0$ [11], that are strongly delocalized over the pigments. Excitation of a higher excitonic state will result in an ultrafast relaxation down the exciton ladder to the energetically lowest lying exciton state $k^{as} = 0$ on a timescale of about 100 fs (as indicated by the grey arrow in Figure 5.2b) [69,86]. This excitation can migrate along the B850 ring on an ultrafast time scale [11], which is thought to be favourable for the transfer of energy to adjacent light-harvesting complexes as the excitation can be offered to LH complexes in different directions within a very short time.

The carotenoids give rise to an absorption band in the green spectral region at around 450 to 540 nm. Just as is the case in RC-LH1, they serve as additional pigments on the one hand and as protective switches on the other (see section 4.1.3) [70,71].

The three different pigment pools together act as an energy funnel [8]. Energy absorbed within the B800 band will be efficiently transferred to B850 on a timescale of less than

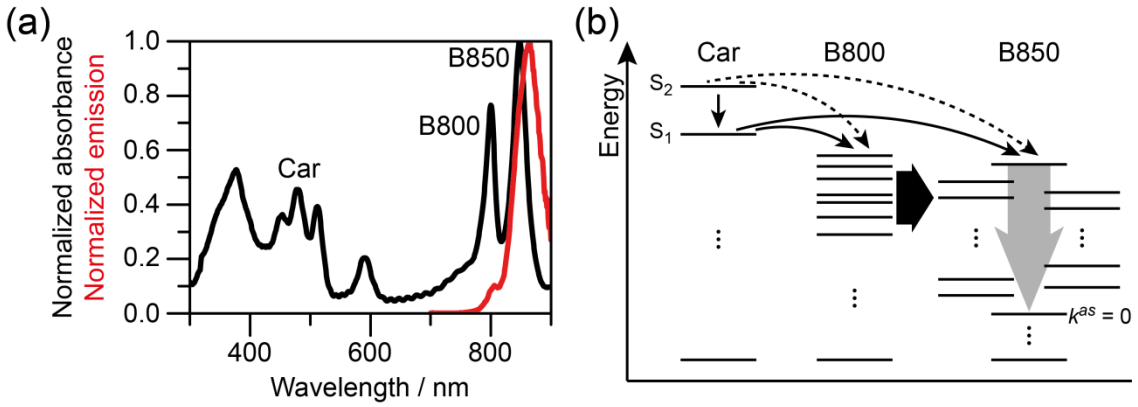

Figure 5.2: a) Normalized absorption (black) and emission (red) spectra of a dilute solution of LH2 from *Rb. sphaeroides* at room temperature. The absorption bands of the three pigment pools are highlighted by their respective abbreviations. Data show results from [20]. b) Sketch of the energy transfer between and within the pigment pools of LH2. Thin black arrows (straight and dotted) mark energy transfer while the broad black arrow indicates energy transfer from the manifold of the B800 Q_y states to the manifold of exciton states of the B850 band. The broad grey arrow denotes ultrafast relaxation within the exciton manifold of B850 into the lowest lying exciton state $k^{as} = 0$. The Q_x states of B800 and B850 have been omitted for clarity, but pose waypoints of additional energy transfer routes.

1 ps [147,148]. There, it relaxes to the lowest lying exciton state. Energy absorbed by the carotenoids can either be transferred to the B800 ring or the B850 ring on timescales of 200 – 300 fs (see sketch in Figure 5.2b) [86]. Either way this eventually results in the excitation being funnelled to the lowest lying B850 state from where it can be transferred to an adjacent LH complex (*in vivo*) on a picosecond time scale or decay either fluorescently or non-fluorescently (in the case of isolated complexes) on a timescale of nanoseconds [114].

5.1.3. Metallic Nanostructures for Plasmonic Enhancement

During the past decade it has been well established that the emission rate of a fluorescent dye can be significantly modified by coupling it resonantly to noble metal nanoparticles (NPs) [149–151]. In such particles, the conduction electrons can be excited collectively resulting in a plasmon. The details of the plasmon spectrum depend on the material, the dielectric constant of the surrounding medium, and the size/shape of the NP [152–154]. The extinction of light in resonance with the plasmon oscillation

features not only an absorption component but also a strong scattering component, which produces new field components in the vicinity of the NP. As a consequence of this, the excitation and emission properties of a fluorophore close to the NP can be altered significantly. Both, quenching of the chromophores' fluorescence due to energy transfer to the NP and subsequent radiationless dissipation, as well as an increased emission due to the enhancement of the local electric field becomes possible [18,19,155] (see also section 2.5). The net effect of the change of the fluorescence rate of the chromophore depends on the mutual arrangement of the chromophore and the noble metal NP, as well as the spectral overlap between the absorption spectrum of the chromophore and the plasmon resonance [156,157]. Meanwhile plasmon coupling of chromophores has been exploited for various biophysical applications for example for biomolecular recognition [158] or as a molecular ruler [159,160].

An important step forward to control the optical response of complex biomolecules has been reported by MACKOWSKI *et al.* [16] who studied a peridinin-chlorophyll-protein (PCP), which is a photosynthetic antenna complex from algae. These authors showed that placing a PCP complex close to a silver island film resulted in an enhancement of the fluorescence intensity of these systems by more than 1 order of magnitude. This enhancement was attributed to a significant increase of the excitation rate of the antenna induced by excitations in the silver layer, suggesting a novel route that can be used to improve the light-collection efficiency of the PCP complex. Recently, a similar enhancement of the absorption of photosystem I (PS I) from plants was observed in a study conducted on ensembles of PS I metal nanoparticle hybrids and on single PS I systems [161,162].

Some of the structures that have proven to be the working horses of plasmon research are spherical noble metal nanoparticles, cylindrical nano rods and nano-bowties [163–165] – two close lying noble metal triangles facing each other with one of their tips. An overview of these structures and their typical absorbance spectra, which give information on their plasmon resonances, is shown in Figure 5.3. In the following, we

will discuss the benefits and drawbacks of using the respective particle class to study fluorescence enhancement.

i. **Spherical nanoparticles** are the easiest of all three to fabricate and can be tailored to patterns that cover macroscopic length scales [166]. This opens the possibility to study systems where no specific binding between nanoparticle and chromophore could be realized, as we will average over a continuum of possible configurations between them across the pattern. The plasmonic properties of spherical nanoparticles can be calculated with relatively simple methods and the position of their plasmon resonance can be shifted by adjusting the diameter of the sphere. Their drawback is a relatively low theoretical enhancement effect.

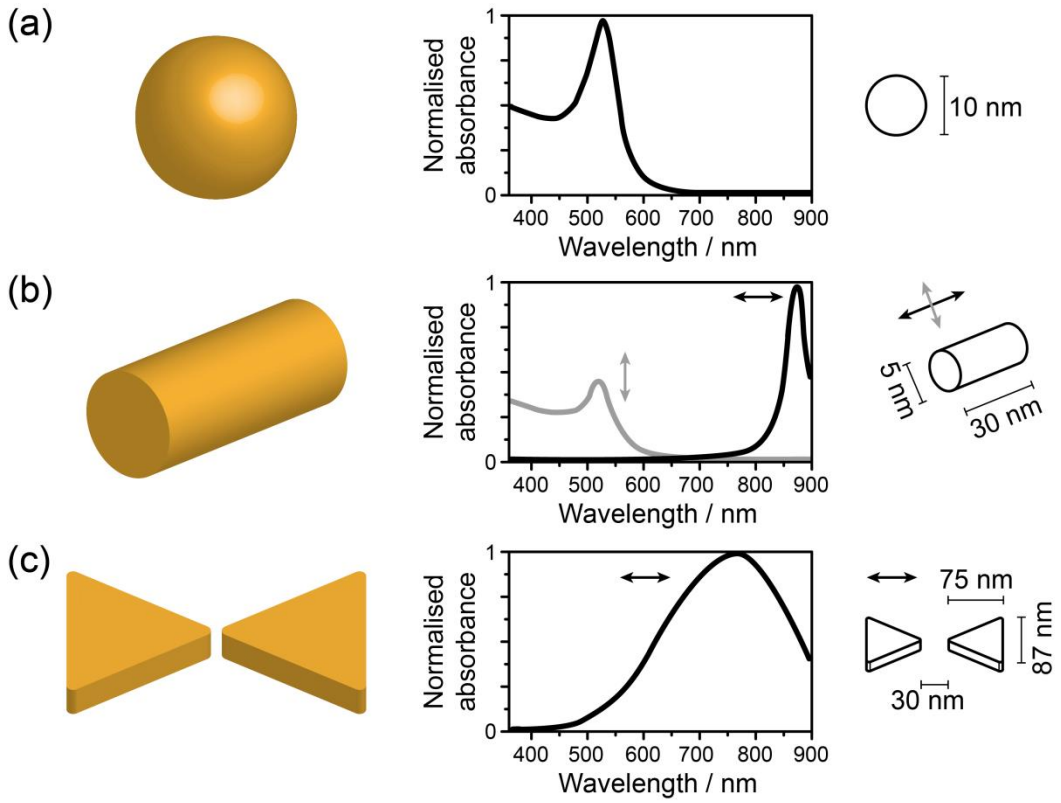

Figure 5.3: Examples of typical plasmonic nanostructures: a) spherical gold nano particle, b) gold nano rod, c) bowtie gold nano antennas. Exemplary dimensions of the particles together with their respective typical plasmon spectra are shown in the graphs to the right of the particles. Double headed arrows indicate the polarisation of incident light relative to the NP and their corresponding absorbance spectra.

ii. **Nano rods** feature two plasmon resonance peaks that are reflected in their structure by their length and their diameter [163]. They allow the polarisation dependent excitation of the plasmon resonances and by adjusting their length, the corresponding resonance peak can be shifted mostly independent of the other plasmon resonance to the red for longer nano rods and to the blue for shorter ones. Patterning large surfaces is less straightforward than for nano spheres. Usually a pattern of nano rods that covers a macroscopic length scale is paid for by a loss of order in the pattern or a loss of control over the dimensions of the nanorod [167]. Well defined structures and patterns can be achieved by electron beam lithography or other more sophisticated techniques [165,168,169], which is very time consuming for large patterns and only practical for small areas.

iii. Usually electron beam lithography is also used to manufacture **bowtie nano antennas**. They promise the highest field enhancement factors of all the discussed structures, as the gap between both triangles can host very high electric fields [170]. By adjusting the size of the triangles and the width of the gap, their plasmon resonance can efficiently be tuned [171]. As they feature two distinct symmetry axes (when viewed from above), their plasmon response is also dependent on the polarisation of the incident light. To date only small areas can be covered with bowtie nano antennas.

The work of MACKOWSKI *et al.* [16] already demonstrated that the plasmon-induced amplification of the electromagnetic fields is also effective for chromophores that are embedded in a protein matrix. However, any type of systematic tuning of the electronic properties of biological functional units required a better control of the plasmon nanostructures. As a first step toward this goal, we decided to use well defined, monodisperse spherical gold nanoparticles as conductor for the plasmonic fluorescence enhancement of LH2 complexes. They could be manufactured to form well defined quasi-hexagonal patterns that covered areas of several cm^2. The separation between the particles was such as to exclude a coupling between them. Moreover, their reduced

structural complexity later allowed for an efficient theoretical modelling of the system. Employing a high throughput single molecule approach we were able to accumulate meaningful statistics but could avoid the disadvantages of ensemble averaging at the same time.

5.2. Experimental

5.2.1. Sample Preparation

Fused silica (SiO_2) substrates coated with AuNPs were manufactured by Simon Ullrich and Stefan Kudera (MPI IS, Stuttgart, Germany), following the procedure described in ref [166]. The substrates carried a quasi-hexagonal pattern of spherical AuNPs with a mean centre-to-centre distance of about 60 nm. The nanoparticles featured a narrow size distribution with an average diameter of (12.3 ± 1.3) nm. The plasmon resonance occurs at a peak position of 525 nm with a width of 260 nm (FWHM).

The LH2 complexes from *Rhodobacter (Rb.) sphaeroides* (strain 241) were isolated and purified as described previously [172] by Mrs. June Southall at the workgroup of Prof. Richard Cogdell, University of Glasgow. After purification the LH2 complexes were transferred to a buffer (20 mM TRIS/HCl, pH 8, 0.2% LDAO), aliquoted and stored at -80 °C until used. For the present experiments this stock solution was diluted with buffer to 10^{-12} M and 2% polyvinyl alcohol (PVA) was added. Subsequently the material was spin coated onto an AuNP substrate forming an amorphous film with a thickness of about 100 nm that contained the LH2 complexes, see Figure 5.4. The low LH2 concentration ensures that the average distance between the LH2 complexes that interact with AuNPs is significantly larger than the resolving power of the optics employed.

For reference experiments, thin films of PVA were produced by spin coating solutions with varying concentrations of PVA onto SiO_2 substrates. For films of 20 nm thickness,

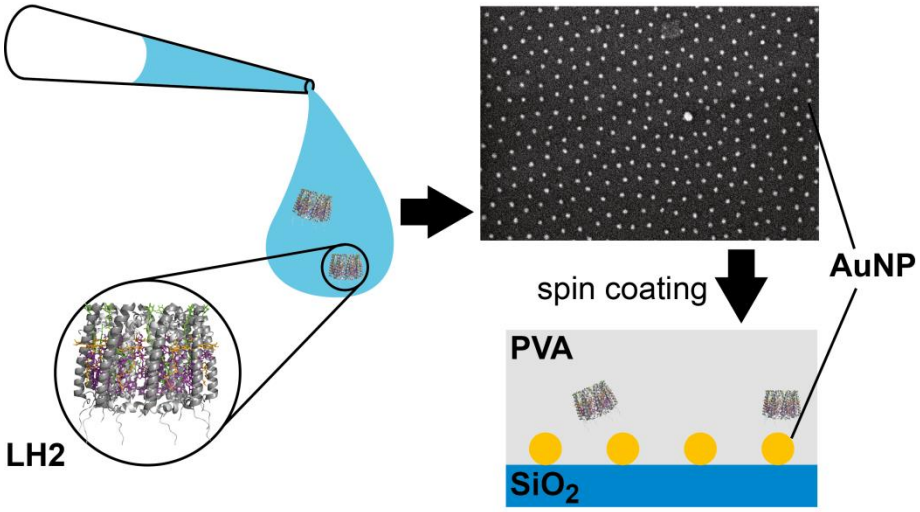

Figure 5.4: Left: A buffer solution containing 2% of PVA and a low concentration of LH2 complexes from *Rb. sphaeroides* was spin coated onto a fused silica (SiO_2) substrate. Top right: Electron micrograph of the nanopatterned substrate that is covered with an array of gold nanoparticles (AuNP). Bottom right: Schematic side view of the sample (not to scale) displaying the substrate (blue), AuNPs (yellow), LH2 (dark grey), and the PVA matrix (light grey). The thickness of the PVA layer is about 100 nm. Figure adapted from [131].

the same buffer solution as for dilution of the LH2 stock solution was used with the addition of 0.2% PVA. The substrate was covered completely with the solution and spun for 16 s at 500 rpm (including a ramp of 6 s) followed by 70 s at 2500 rpm (including a ramp of 10 s) with a spin coater Model P6700 (Specialty Coating Systems Inc.) resulting in dry PVA films that were homogeneous over the whole substrate surface.

5.2.2. Experimental Protocol

For single molecule measurements the experimental setup as described in section 3.2 was used. To obtain the fluorescence intensities of single LH2 complexes or AuNP-LH2 hybrids, the samples were illuminated either at 514 nm or at 788 nm, at an excitation intensity of 140 W/cm^2, each. At both excitation wavelengths, measurements were taken of LH2 complexes spin coated onto substrates carrying AuNP as well as bare SiO_2 substrates. For every investigated spot on the respective sample, a

fluorescence image was taken with an integration time of 500 ms. These images were analysed using home-written software, as described in section 3.2. It extracted the background corrected, integrated fluorescence intensities of single LH2 complexes (or AuNP-LH2 hybrids) and registered them in the histograms shown later on.

The thickness of thin PVA films was characterized by scratching a thin line into the polymer with the back of a scalpel. Care was taken not to scratch the substrate carrying the PVA film. Subsequently, the scratch was investigated with an atomic force microscope as described in section 3.4. The resulting two-dimensional height profiles were analyzed in sections for the height of the film. The obtained film heights were averaged over several sections per sample and over multiple samples.

5.3. Results

5.3.1. LH2 on AuNPs and on bare SiO_2

The distributions of the fluorescence response from individual LH2 complexes are compared in Figure 5.5 (results reproduced from [20]). For the left panel, Figure 5.5a, the samples were excited at 514 nm, that is, within the region of spectral overlap of LH2's absorption and the plasmon resonance of the AuNPs. Whereas for the right panel, Figure 5.5b, the samples were excited at 788 nm, that is, far outside the overlap of the LH2's absorption with the plasmon resonance. The ensemble absorption spectrum of LH2 has equal extinction coefficients at these wavelengths (see insets Figure 5.5). This is why these particular wavelengths were chosen. However, since a direct comparison of the emission intensities at the two excitation wavelengths is hampered by several experimental factors, such as differences in the transmission characteristics and/or the collection efficiencies of the optical setup, or variations in focal size, at each excitation wavelength a control experiment on bare SiO_2 substrates without AuNPs was conducted (Figure 5.5, data shown in grey). From these controls, the mean fluorescence intensity, $\langle I_{ref} \rangle$, could be deduced for a LH2 complex in the

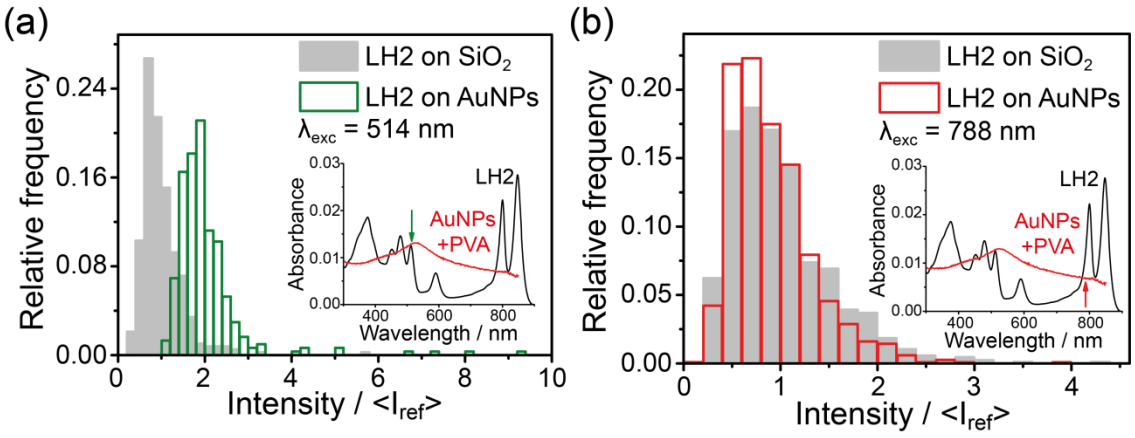

Figure 5.5: Distributions of the fluorescence response from individual LH2 complexes (a) for excitation at 514 nm and (b) for excitation at 788 nm. The insets display the absorption spectrum of LH2 (black line) overlaid with the plasmon resonance of the AuNPs in PVA (red line). The arrows indicate the wavelengths of 514 and 788 nm, respectively. The coloured histograms have been obtained from LH2 complexes on substrates covered with AuNPs, and the grey histograms were recorded from LH2 complexes on bare SiO_2 substrates. For better comparison the histograms are scaled to relative occurrences, and the fluorescence intensities are given in units of $\langle I_{ref} \rangle$, which refers to the mean of the fluorescence intensity observed for the reference experiment on bare SiO_2 substrates (grey bars). The absolute number of LH2 complexes contributing to the histograms was (bare/covered substrate) 378/303 (panel a) and 867/1184 (panel b). Both panels show results from [20].

absence of nanoparticles. In the following, the measured fluorescence intensities observed in the presence of the AuNPs will be given in units of the respective $\langle I_{ref} \rangle$ in order to allow direct comparisons.

Excitation of LH2 at 514 nm on bare SiO_2 substrates yields a distribution of the relative intensities with a mean value of 1.0 (by definition of $\langle I_{ref} \rangle$) and a standard deviation of 0.5. For the substrates covered with the gold spheres the respective histogram in Figure 5.5a is clearly shifted toward higher intensities and is characterized by a mean (standard deviation) of 2.0 (0.9). A few of the individual LH2 complexes had relative fluorescence intensities between 4.1 and 9.3 and one complex had a maximum intensity of 12.2. The histograms obtained from the experiment at 788 nm are displayed in Figure 5.5b and are characterized by a mean (standard deviation) of 1.0 (0.5) for the bare SiO_2 substrate and 0.9 (0.4) for the coated substrate, showing no significant statistical differences between these two distributions. These data clearly reveal the

influence of the plasmon resonance of the AuNPs on the fluorescence intensity of the pigment-protein complexes.

5.3.2. Reference Experiments

The fact that the experiments display a broad range of enhancement factors can be ascribed to a distribution of distances and mutual orientations between the LH complexes and the NPs. In order to obtain a coarse grained estimate for the maximum distance between a LH2 and an AuNP for which the enhancement effect can be observed, a similar experiment as described above was performed yet with a slightly modified preparation of the sample. First the AuNP substrates were covered with an extra layer of PVA with a thickness of about (20 ± 5) nm and then the LH2-containing PVA solution was spin coated on top of this. To account for slightly varying preparation conditions the above value for the film thickness is a conservative estimate. An example for an actual measurement of the film thickness is shown in Figure 5.6.

Applying an additional film of PVA as a spacer layer ensured a minimum distance of

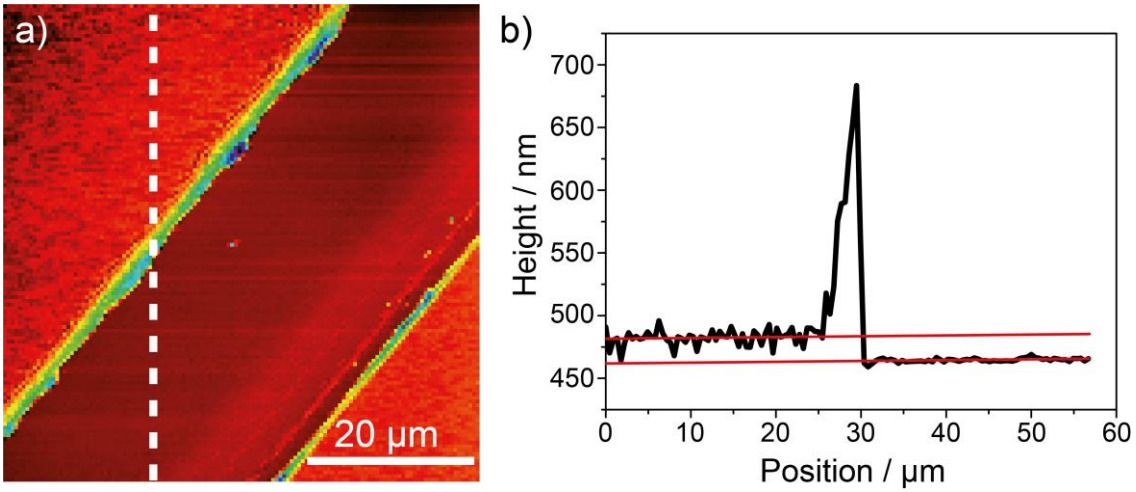

Figure 5.6: a) AFM height image of a PVA film on a fused silica substrate. The image was taken at a resolution of 128 x 128 pixels and a speed of 5 s/line, the length of one edge is 57 µm. b) Height profile along the dotted line. For this example the film thickness amounts to (19.9 ± 1.2) nm, which has been extracted from the two fits (red lines). The steep increase of the height profile is attributed to material that has been dislocated by the scalpel. Figure adapted from [131].

about 20 nm between the LH2 complexes and the AuNPs. In this case, no enhancement of the LH2 emission due to the presence of the AuNPs could be observed (see Figure 5.7) providing an upper limit of 20 nm for the maximum distance between the LH2 and the AuNPs for an observable enhancement effect.

5.4. Discussion

An estimate for the enhanced absorption of a LH2 complex in the vicinity of a AuNP can be obtained by considering a metallic sphere that is illuminated by a plane wave $\vec{E}_{noNP} = \vec{E}_0 e^{-i\omega t} = E_0 \hat{n}_{E_0} e^{-i\omega t}$. Here E_0 denotes the amplitude of the incident electric field, which is linearly polarized along the direction of the unit vector $\hat{n}_{E_0}$. In the limit where the size of the NP is much smaller than the wavelength of light, the dominating contribution to the scattered field comes from the dipolar component [173]. Within this approximation the electric potential in presence of the NP is given by [174]

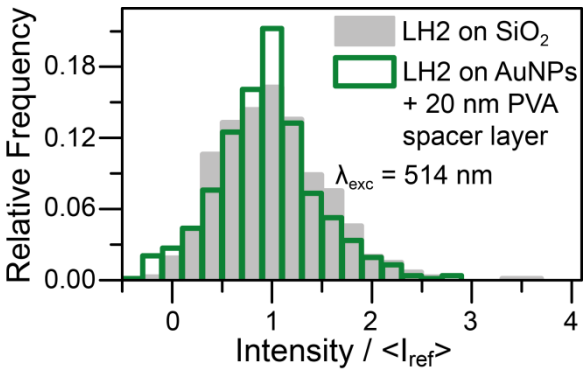

Figure 5.7: Comparison of the distributions of the fluorescence response from individual LH2 complexes from *Rb. sphaeroides* on bare SiO_2 substrates (grey bars, 745 complexes) and on AuNP-covered SiO_2 substrates with a (20 ± 5) nm PVA spacer layer between LH2 and the AuNPs (green bars, 777 complexes). Intensities are given in units of $\langle I_{ref} \rangle$, which corresponds to the mean of the intensity distribution obtained from LH2 on bare SiO_2 (grey bars). The mean (standard deviation) of the histograms are 1.0 (0.5) (grey) and 0.9 (0.5) (green), respectively. The negative values on the abscissa are an artefact that occurs for low intensity complexes that undergo blinking. This is not relevant for the conclusions. Figure from [131].

$$\varphi_{NP} = \varphi_{noNP} + \varphi_{scatter} = -\vec{E}_0 \cdot \vec{r} + R^3 \frac{\varepsilon_{NP} - \varepsilon_{Medium}}{2\varepsilon_{Medium} + \varepsilon_{NP}} \frac{\vec{E}_0 \cdot \vec{r}}{r^3} \qquad 5.1$$

Here φ_{noNP} corresponds to the electric potential without NPs, ε_{NP} and ε_{Medium} denote the dielectric functions of the NP and the surrounding medium, respectively. R corresponds to the radius of the NP, and $\vec{r} = r\vec{n}_r$ refers to the radius vector from the origin, which is placed in the centre of the NP. For brevity the time dependence of the electric field has been omitted. The amplitude of the electric field in the presence of the NP follows from $\vec{E}_{NP} = -\nabla\varphi_{NP}$ which yields

$$\vec{E}_{NP} = \vec{E}_0 - \beta \frac{R^3}{r^3} \vec{E}_0 + 3\beta \frac{R^3}{r^5} (\vec{E}_0 \cdot \vec{r})\vec{r} \qquad 5.2$$

using the abbreviation $\beta = (\varepsilon_{NP} - \varepsilon_{Medium})/(2\varepsilon_{Medium} + \varepsilon_{NP})$. The enhancement factor of the intensity of the electric field due to the presence of the NP can be defined as $P = \left|\vec{E}_{NP}\right|^2 / \left|\vec{E}_{noNP}\right|^2$ which reads in this approximation

$$P = 1 - 2\frac{R^3}{r^3}\mathrm{Re}(\beta)\left[1 - 3\left(\hat{n}_{E_0} \cdot \hat{n}_r\right)^2\right] + \frac{R^6}{r^6}|\beta|^2\left[1 + 3\left(\hat{n}_{E_0} \cdot \hat{n}_r\right)^2\right] \qquad 5.3$$

Averaging this expression over all directions finally yields

$$\langle P \rangle_r = 1 + 2\frac{R^6}{r^6}|\beta|^2 \qquad 5.4$$

which gives the enhancement factor of the intensity of the electric field as a function of the distance of the chromophore from the NP.

Using equation 5.4 one can calculate the distribution of the enhancement factors $\langle P \rangle_r$ within a spherical shell that surrounds the NP concentrically with an inner radius $R + \rho$ and a thickness d (see Figure 5.8b for comparison). For ε_{NP} the dielectric function of gold as given in ref [175] was used ($\varepsilon_{NP} = -3.95 + 2.58i$) and ε_{Medium} was set to $\varepsilon_{PVA} = 2.19$. The distance ρ between the inner surface of the shell and the surface of the NP was set to 3 nm, which takes into account that the pigments are embedded in a protein matrix that is surrounded by a cage of surfactant molecules.

However, when trying to relate the calculated distribution of the enhancement factors to the experimentally observed intensity distribution of the LH2 fluorescence, one faces the problem that the fluorescence intensity from individual LH2 complexes already features a distribution without any NPs, see Figure 5.5a (grey bars). Therefore the simulated distribution for the enhancement factors was convoluted with the distribution of the fluorescence intensity of the LH2 complexes that is observed on bare SiO_2 substrates NPs.

The result of this procedure is shown in Figure 5.8 for d varying from 0.5 to 11 nm, together with the measured reference distributions of the fluorescence intensity in the

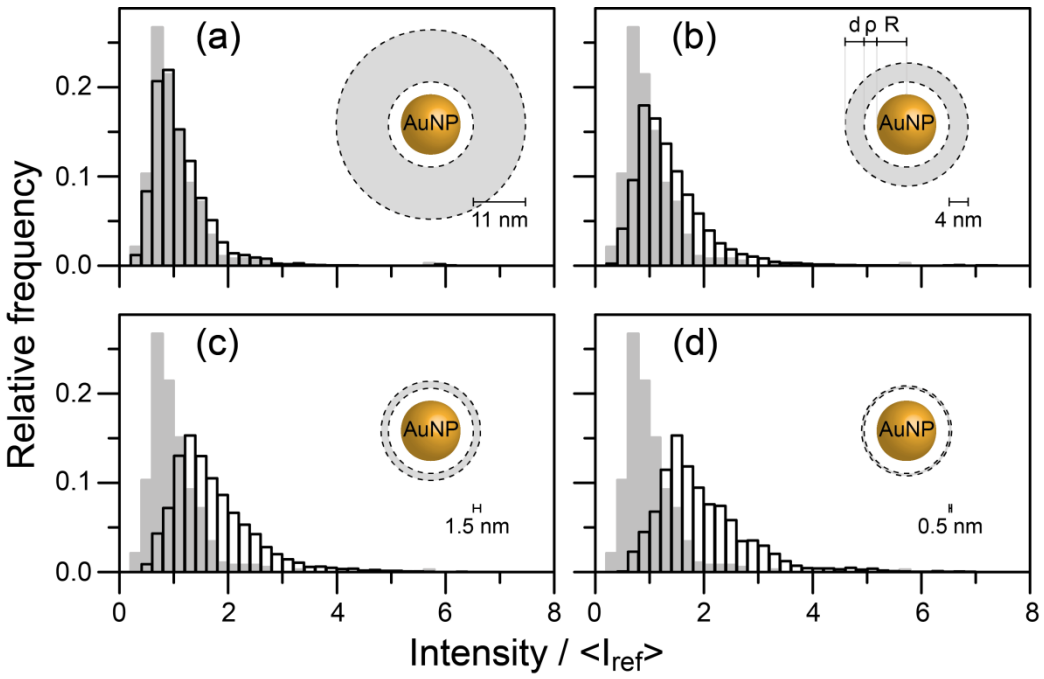

Figure 5.8: Calculated intensity distributions for the fluorescence enhancement of LH2 complexes (black) as a function of their distance from a single AuNP. The calculations were performed using a dipole approximation as explained in the text. The LH2 complexes were located within a shell of finite thickness d (grey area) that accommodates the AuNP (yellow) in its centre. The distance between the surface of the AuNP and the inner surface of the shell was set to 3 nm, while the thickness d of the shell was varied from 11 nm (top left) to 0.5 nm (bottom right). The intensities are given in units of $\langle I_{ref} \rangle$, which corresponds to the mean of the intensity distribution obtained experimentally from LH2 on bare SiO_2 (grey). The mean (standard deviation) of the simulated histograms are (a) 1.1 (0.6), (b) 1.4 (0.7), (c) 1.7 (0.9), and (d) 2.0 (1.0). Figure adapted from [131].

absence of NPs (light grey). An enhancement of the LH2 fluorescence that resembles the experimentally obtained intensity distribution is found only if the distance between the AuNP and the pigments falls into the range of 3-5 nm. This finding is consistent with the result from the control experiment with the extra PVA layer. The conjecture that the LH2 complexes seem to stick to the AuNPs within a thin layer of only a few nanometres thickness is in line with the well-known fact that proteins tend to adsorb on noble metal surfaces [176].

5.5. Conclusion

In a systematic study, we could show plasmonic fluorescence enhancement of individual LH2 complexes by gold nano spheres. We took great care to precisely define the system under investigation by using monodisperse, non-interacting AuNP, that could only interact with a single LH2 at a time. Using a high throughput single molecule approach, we obtained clear and meaningful statistics and could bypass the disadvantages of ensemble measurements.

Excitation of LH2 in resonance with the AuNPs' plasmons in average resulted in a fluorescence enhancement factor of 2, while off-resonant excitation showed no fluorescence enhancement at all. Introducing a spacer layer of 20 nm between AuNP and LH2 efficiently prevented fluorescence enhancement, even when the LH2 complexes were excited in resonance with the plasmon. In combination with model calculations this led to the conclusion that the LH2 complexes adsorb to the AuNP and are located within a thin shell around the individual particles. The fact, that the experimental data is well reproduced by the model calculations gives rise to the assumption, that the LH2 complexes only witness an absorptive enhancement, as only this contribution was taken into account in the model. The quantum yield and thus the radiative rate of LH2 seem to remain unchanged.

This study marks a first step in the use of noble metal nanoparticles for tuning the photophysical properties of integral membrane antenna complexes in a well-defined

way. In combination with other recent studies [17,177–180] it shows the way on how we can manipulate nature to build novel biohybrid light-harvesting architectures.

6. Artificial System: Photophysical Characterisation of CBT-Derivatives

The photophysical properties of two novel multichromophoric compounds are presented. Their molecular design comprises a carbonyl-bridged triarylamine core and either naphthalimides or 4-(5-hexyl-2,2'-bithiophene)-naphthalimides as second chromophore in the periphery. Steady-state and basic time-resolved spectroscopic investigations of these compounds, in combination with three reference compounds, provide clear evidence for energy transfer in both multichromophoric compounds. The direction of the energy transfer depends on the lateral chromophore used.

Note: This chapter closely follows and in wide parts cites the publication A. T. Haedler, S. R. Beyer, *et al.*, "Synthesis and Photophysical Properties of Multichromophoric Carbonyl-Bridged Triarylamines", *Chemistry - A European Journal*, **20**, 11708-11718 (2014). [181] The CBT-derivatives as well as their reference compounds were kindly provided by the workgroup of Prof. Hans-Werner Schmidt. The substances were designed and synthesised by Mr. Andreas T. Haedler. The spectroscopic results were analysed and discussed in close cooperation with Mr. Haedler.

6.1. Introduction

Exploiting the unique properties of organic matter for electronic applications holds great promise. Not only does the production of organic materials and devices typically need less resources and energy than their inorganic counterparts, but organic materials also have the potential to open up new applications in light-harvesting and solar energy conversion. In particular, functional π-conjugated systems are of key interest for such applications, as they possess appealing optoelectronic properties [182,183]. However, an order of magnitude estimate, based on the absorption cross-section of a typical organic chromophore and the number of photons provided from the sun, yields that under optimum conditions an organic molecule would absorb only a few photons per

second [184]. From this it becomes clear that employing organic matter for any kind of solar energy conversion requires an efficient light-harvesting apparatus (an antenna) for collecting as many photons as possible. This requirement is nicely illustrated by the setup of the natural light-harvesting machineries (see also section 4.1.1) where hundreds of light absorbing chromophores, organized in protein complexes serve for the collection of sunlight, whose energy is transferred efficiently among these chromophores to a special pair of pigments, which initiates an electron transfer chain thereby acting as a transducer [11]. The attempt to mimic these biological systems led to a number of different approaches aiming for an excess of donor chromophores, which funnel the excitation energy into a small number of acceptor chromophores. Despite extensive research the structural diversity of the employed chromophoric systems remains rather narrow and comprises mostly rylene diimides [185–191], fullerenes [192–197], porphyrins, and phthalocyanines [198–201], potentially decorated with thiophene and triarylamine donors [202–204]. Furthermore, multichromophoric dendritic [205–207], polymeric [208–211], and supramolecular systems [212–215] were investigated.

Promising alternative building blocks are bridged C_3-symmetric triarylamines, so-called heterotriangulenes [216,217], in particular with three electron-withdrawing carbonyl moieties. When suitably substituted, these compounds form columnar structures [22–24,218] and possess tuneable photophysical properties [21,219,220]. The carbonyl-bridged triarylamine (CBT) moiety acts as a moderate electron acceptor with appealing optoelectronic and materials characteristics for organic electronics applications [221–224]. For example, star-shaped CBT-derivatives, bearing directly connected lateral carbazole moieties, have been reported as electroluminescent materials in organic light emitting diodes [225].

Synthetic procedures to obtain functionalized carbonyl-bridged triarylamines as well as basic studies of their photophysical properties are still rare. Herein, we present two three-armed multichromophoric compounds **1** and **2** comprising the carbonyl-bridged triarylamine core with either three naphthalimide (NI) or three 4-(5-hexyl-2,2'-

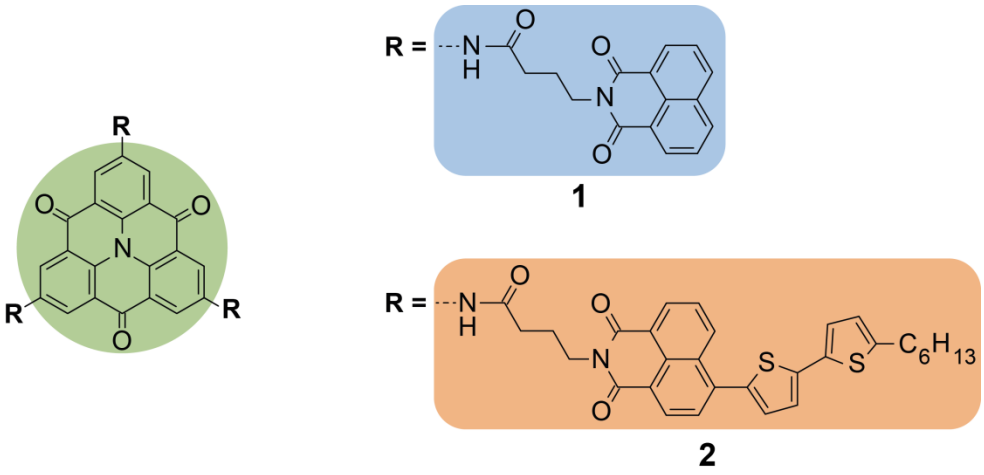

Figure 6.1: Molecular structures of the multichromophoric compounds **1** and **2**, comprising a carbonyl-bridged triarylamine (CBT, green background) with peripheral naphthalimides (NI, blue background) and peripheral 4-(5-hexyl-2,2'-bithiophene)-naphthalimide (NIBT, orange background) chromophores, respectively.

bithiophene)-naphthalimide (NIBT) chromophores in the periphery (Figure 6.1). The bridged triarylamine and the chromophores in the periphery are linked by an amide unit and a short alkyl spacer to break the conjugation between the chromophores. To understand the photophysical properties of the multichromphoric compounds **1** and **2**, three reference compounds **3**–**5** (Figure 6.2) were investigated additionally. In the following, we demonstrate that the energy transfer in **1** proceeds from the naphthalimide periphery to the CBT core and in **2** from the core to the 4-(5-hexyl-2,2'-bithiophene)-naphthalimide.

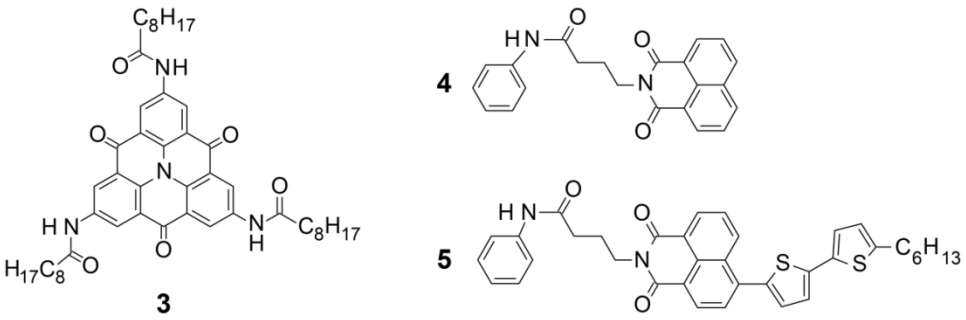

Figure 6.2: Chemical structures of the reference compounds **3-5** representing the CBT-core, the naphthalimide (NI), and the 4-(5-hexyl-2,2'-bithiophene)-naphthalimide (NIBT) moiety, respectively.

6.2. Experimental

6.2.1. Sample Preparation

Compounds **1**-**5** were kindly provided by the workgroup of Prof. Hans-Werner Schmidt, University of Bayreuth. Under the lead of Mr. Andreas T. Haedler, the compounds were synthesized as described in [181]. After recrystallization the compounds were stored under dry conditions in a low-light environment until used.

Stock solutions of compounds **1**-**5** were prepared by adding the respective substance to 1,1,2,2-tetrachloroethane (TCE, used as received). The samples were heated under stirring until clear solutions were obtained. After dilution with TCE to the desired concentration, the solutions were used for measurements immediately.

6.2.2. Experimental Protocol

UV/vis absorbance spectra were recorded on a PerkinElmer Lambda 750 Spectrophotometer (see section 3.3) with a scan speed of 274 nm/min, a spectral resolution of 2.0 nm, and a data interval of 1 nm in the range of 250–1100 nm (for clarity we do not show the full range). The solutions were measured directly after preparation in 10 mm Hellma QS quartz-glass cuvettes at room temperature.

All PL emission spectra were recorded on a JASCO FP-8600 Spectrofluorometer (see section 3.3) with a scan speed of 200 nm/min and a data interval of 0.4 nm from 10 nm above the excitation wavelength to 800 nm. The excitation and emission bandwidth were set to 5 and 2 nm, respectively, with a 0.1 s response time. For the photoluminescence (PL) emission maps the excitation wavelength was varied in 2 nm steps from 280 to 700 nm. The solutions were measured directly after preparation in 10 mm Hellma QS quartz-glass cuvettes at room temperature. Compounds that contain 4-(5-hexyl-2,2'-bithiophene)-naphthalimide (**2** and **5**) show strong photo-bleaching upon excitation in the high-energy range of the spectrum. To avoid corruption of the PL emission maps by this effect, we had to replace solutions containing these compounds

by unilluminated samples in distinct intervals. The excitation wavelengths at which the sample was replaced are marked by dashed horizontal lines in the respective PL emission maps. For the measurement of PL quantum yields the spectrofluorometer could be equipped with an integrating sphere and the detection range was adjusted accordingly.

Time-resolved measurements were performed with different custom-built setups. For excitation at 440 nm (compounds **2**, **3** and **5**) the setup as described in section 3.1.4 was used. Those samples were held in quartz-glass cuvettes (Hellma, 10 mm) and excited with a laser repetition rate of 810 kHz and a fluence of 10^{13} photons/(pulse·cm²). The streak camera's detection window was set to 5 ns.

For excitation at 360 nm (compounds **1** and **4**) a similar setup to that described in section 3.1.4 was kindly provided by the workgroup of Prof. Anna Köhler, University of Bayreuth, under the supervision of Mr. Alexander Rudnick. Briefly, the samples were held in quartz-glass cuvettes (Hellma, 10 mm) and were excited by the frequency doubled and pulse picked light from a Ti:Sapphire laser system (Chameleon 2 Ultra, Coherent). The emission signal was collected in a right-angle geometry and directed to a streak camera system equipped with an imaging spectrograph (Optronis SRU-BA with spectrograph Acton SP2300, Princeton Instruments). The laser's repetition rate was set to 8 MHz, with a fluence of $3.6 \cdot 10^{14}$ photons/(pulse·cm²) in the excitation spot. The streak camera's detection window was adjusted to the respective sample.

At both excitation wavelengths, the repetition rates and fluences of the excitation light were kept as low as possible to avoid annihilation processes. For a first basic characterization of the time-resolved properties of compounds **1**-**5**, as they are presented in this chapter, we spectrally integrated the emission signal from each individual compound. For data analysis, we used home-written software to conduct a reconvolutive (multi-) exponential fit, taking into account the instrument response function of the system.

6.3. Results & Discussion

The photophysical properties of the two multichromophoric compounds **1** and **2** were investigated in solution by absorption, steady-state, and time-resolved photoluminescence (PL) spectroscopy. To facilitate the interpretation of the data, we also studied the reference compounds **3**–**5** with molecular structures as close as possible to their respective π-conjugated subunits in the multichromophoric systems. Furthermore, the photoluminescence quantum yields (PL-QY) were determined for all five compounds using an integrating sphere. For all of the measurements, 1,1,2,2-tetrachloroethane (TCE) was used as it is a good solvent for these compounds. The concentration of the CBT derivatives **1**–**3** was adjusted to 1 µM, while for the naphthalimide and the 4-bithiophene-naphthalimide bearing reference compounds **4** and **5** the concentration was set to 3 µM, to account for the three-armed geometry of compounds **1** and **2**. Photoluminescence emission maps of all five compounds were recorded varying the excitation wavelength between 280 and 700 nm (Figure 6.3-Figure 6.6a and Figure 6.8a). Two additional maps were recorded from mixed solutions of compounds **3**+**4** and **3**+**5** (Figure 6.7a and Figure 6.9a, respectively) for comparison with the multichromophoric systems **1** and **2**. From these maps, PL emission and PL

Table 6.1: Optical data of compounds **1**-**5**. Adapted from [181].

Comp.	λ_{max} / nm		PL-QY	τ
	Abs.	PL	/ %	/ ns
1	281 340 460	492	~10	0.307 (**r**) 3.6
2	279 340 433	608	~10	0.041 2.4
3	278 459	489	~15	2.5
4	338	382	~5	0.495
5	335 433	609	~25	0.017 2.5

excitation spectra could be extracted for different excitation and emission wavelengths. The time-resolved spectra were recorded on custom-build streak camera setups with picosecond time-resolution using excitation wavelengths of either 360 nm for compounds **1** and **4** or 440 nm for compounds **2**, **3**, and **5** (see Section 6.2.2 for more details). The relevant photophysical properties are summarized in Table 6.1

6.3.1. Reference Compounds

We start the discussion with the CBT reference compound **3**. The absorption spectrum shows two distinct peaks (Figure 6.3b, black solid line): an aromatic π–π* transition at 278 nm with a shoulder at 300 nm and a weak red-shifted absorption at 459 nm. The PL

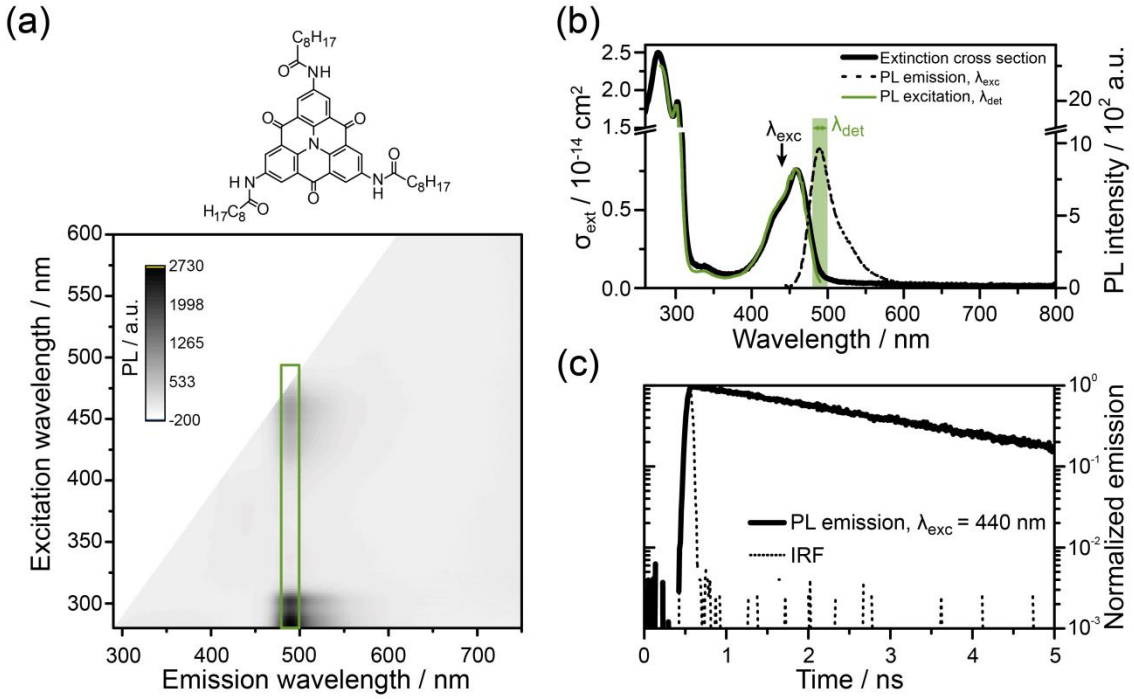

Figure 6.3: Photophysical properties of compound **3** (chemical structure inset in (a)) at a concentration of 1 µM in 1,1,2,2-tetrachloroethane (TCE). a) PL emission map. The spectral signature of compound **3** is highlighted by a green box. b) Absorbance spectrum given as extinction cross section σ_{ext} (black solid line) and PL excitation spectrum detected in the range $\lambda_{det} = [480, 500]$ nm (green solid line). An exemplary PL emission spectrum excited at $\lambda_{exc} = 440$ nm is given as black dashed line. c) Time-resolved PL emission of **3** at $\lambda_{exc} = 440$ nm (solid line) and instrument response function (IRF, dashed line) of the experimental setup. Adapted from [181].

excitation spectrum (Figure 6.3b, green solid line) extracted from the PL emission map (Figure 6.3a) in the emission range from 480-500 nm, closely follows the absorbance spectrum with only minor deviations.

An illustrative PL spectrum of compound **3** upon excitation of the lowest-energy absorption peak at 440 nm is shown in Figure 6.3b (dashed line), which was picked from the photoluminescence emission map in panel (a). A single fluorescence band is observed at 490 nm with a small vibronic shoulder at around 520 nm. The PL emission map reveals that the emission maximum is independent of the excitation wavelength. The PL decay curve of compound **3**, after excitation at 440 nm, shows a clearly monoexponential behaviour with a time constant of $\tau = 2.5\,ns$ (Figure 6.3c) and the photoluminescence quantum yield (PL-QY) of the CBT reference compound was determined to be about 15%.

The absorption spectrum of the second reference compound **4** comprising the naphthalimide exhibits a vibronically structured $S_0 \rightarrow S_1$ transition peaking at 338 nm (Figure 6.4b, black solid line), which is typical for these chromophores. The PL excitation spectrum (Figure 6.4b, blue solid line) extracted from the PL emission map (Figure 6.4a) in the emission range from 372-392 nm, is in close resemblance to the absorbance spectrum of compound **4**.

The photoluminescence emission spectrum of **4** upon excitation at 340 nm (Figure 6.4b, dashed line) reveals the expected vibronically structured naphthalimide fluorescence peaking at around 382 nm [226], which is independent of the excitation wavelength as shown in the PL emission map. The time-resolved PL decay features a monoexponential behaviour with a time constant of $\tau = 495\,ps$ (Figure 6.4c), and the PL-QY was determined to be about 5%. Unfortunately no instrument response function could be retrieved for this measurement. Consequently a fitting procedure that does not involve reconvolution was applied to determine this time constant.

The last reference compound **5** bearing the 4-bithiophene-napthalimide shows absorption over a broad range from 280 to almost 550 nm with two main peaks (Figure

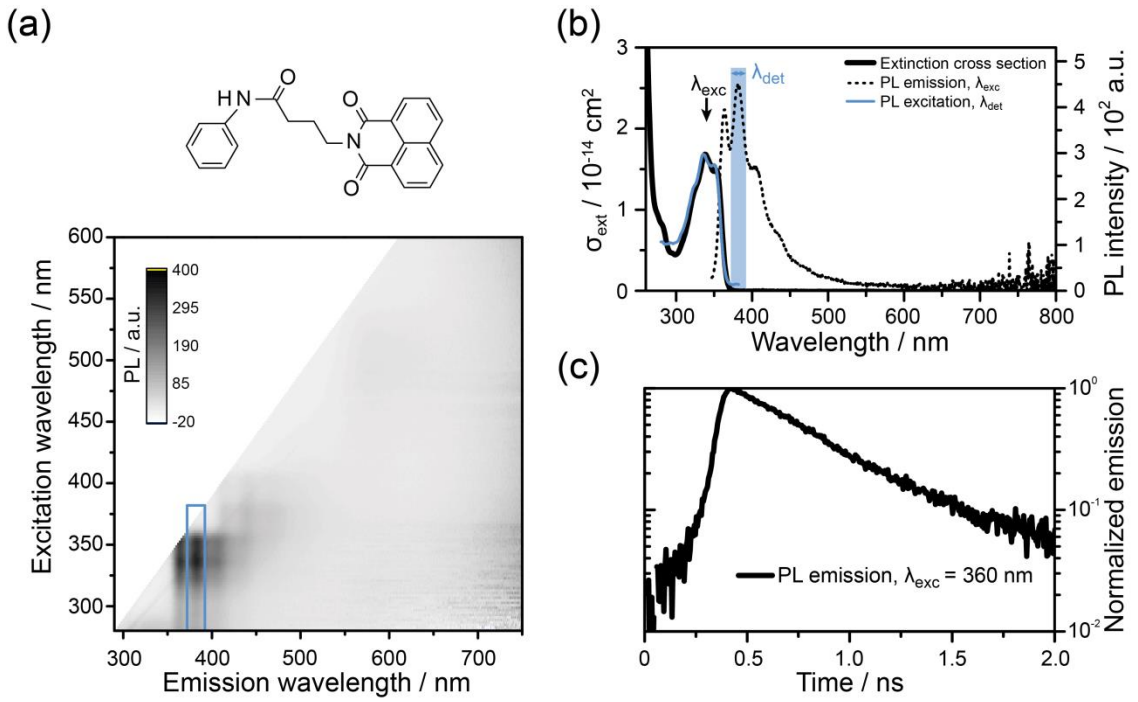

Figure 6.4: Photophysical properties of compound **4** (chemical structure inset in (a)) at a concentration of 3 µM in 1,1,2,2-tetrachloroethane (TCE). a) PL emission map. The spectral signature of compound **4** is highlighted by a green box. Weak PL intensities between an emission wavelength of 420 and 450 nm are of instrumental origin. b) Absorbance spectrum given as extinction cross section σ_{ext} (black solid line) and PL excitation spectrum detected in the range $\lambda_{det} = [372, 392]\, nm$ (blue solid line). An exemplary PL emission spectrum excited at $\lambda_{exc} = 340\, nm$ is given as black dashed line. c) Time-resolved PL emission of **4** at $\lambda_{exc} = 360\, nm$ (solid line). Adapted from [181].

6.5b, black solid line). A higher-energy peak is located at 335 nm and a broad and unstructured peak can be detected around 440 nm, which we attribute to a charge-transfer (CT) absorption between the covalently linked electron-deficient naphthalimide and the electron-rich bithiophene. The PL excitation spectrum (Figure 6.5b, orange solid line) extracted from the PL emission map (Figure 6.5a) in the emission range from 600-620 nm, shows an almost perfect overlap with the absorbance spectrum. The occurring deviations can be attributed to the strong tendency of compound **5** to undergo photo bleaching. At wavelengths below 310 nm, at the high energy end of the employed excitation range, photo bleaching occurs so rapidly that recording an emission spectrum was not possible.

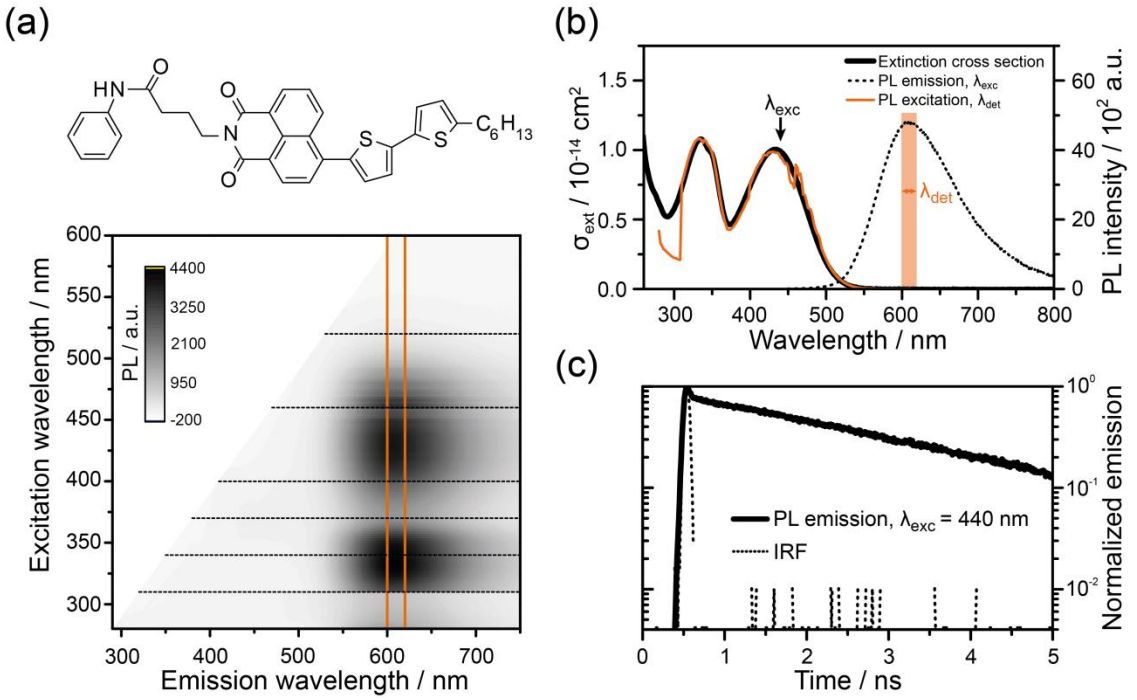

Figure 6.5: Photophysical properties of compound **5** (chemical structure inset in (a)) at a concentration of 3 µM in 1,1,2,2-tetrachloroethane (TCE). a) PL emission map. Horizontal dotted lines mark the replacement of the solution, see text. The spectral signature of compound 5 is highlighted by an orange box. b) Absorbance spectrum given as extinction cross section σ_{ext} (black solid line) and PL excitation spectrum detected in the range $\lambda_{det} = [600, 620]\,nm$ (orange solid line). An exemplary PL emission spectrum excited at $\lambda_{exc} = 440\,nm$ is given as black dashed line. c) Time-resolved PL emission of **5** at $\lambda_{exc} = 440\,nm$ (solid line) and instrument response function (IRF, dashed line) of the experimental setup. Adapted from [181].

The CT character of compound **5** is also reflected in the broad and unstructured photoluminescence between 500 and 800 nm peaking at 609 nm (Figure 6.5b, dashed line), independent of the excitation wavelength (Figure 6.5a). The PL transient of this compound exhibits a more complex multiexponential decay that can best be described by two exponents with time constants of $\tau_1 = 17\,ps$ and $\tau_2 = 2.5\,ns$ and an amplitude ratio of $A_1/A_2 = 1.57$ (Figure 6.5c). Compound **5** possesses the highest PL-QY (ca. 25%) of the reference compounds, which is in accordance with the strong emission intensity of the illustrative spectrum shown in Figure 6.5b.

From the spectra of the reference compounds **3**–**5** shown in Figure 6.3-Figure 6.5, it is clear that the spectral shape of the photoluminescence of these substances is independent of the excitation wavelength. The peak maximum of the PL can be easily

attributed to the naphthalimides (382 nm), the carbonyl-bridged triarylamine (489 nm), and the 4-bithiophene-naphthalimide (609 nm). The characterisation of the individual chromophores shows a significant spectral overlap between the PL of the naphthalimide (NI) and the absorption of the carbonyl-bridged triarylamine (CBT) as well as between the PL of the CBT and the absorption of the 4-bithiophene-naphthalimide (NIBT). This is an important prerequisite for efficient energy transfer.

6.3.2. Multichromophoric Compounds

Having characterized the reference compounds, we now turn to the photophysical properties of the more complex multichromophoric systems **1** and **2**. In both compounds the CBT core is in close proximity of a few nanometres to the respective peripheral chromophore, which should facilitate energy transfer. The absorbance spectra of both multichromophoric systems are a superposition of the absorbance of their respective chromophoric parts with only slight differences in the shape of the bands and in the position of their maxima (Figure 6.6b and Figure 6.8b, black solid lines). For both compounds **1** and **2**, neither strongly shifted nor additional absorbance peaks are observed with respect to the reference materials, which indicates that the electronic coupling between the subunits is weak.

The PL response of compound **1** shows the characteristic emission signature of the CBT core upon excitation at 340 nm but no photoluminescence from the peripheral naphthalimide (Figure 6.6b, dashed line). This behaviour is independent of the excitation wavelength (Figure 6.6a) throughout the whole absorption regime of compound **1**.

From the PL emission map, we also extracted the PL excitation spectra of compound **1** for detection wavelengths that represent the characteristic PL signature of the naphthalimide (372–392 nm) and the CBT core (480–500 nm). The PL excitation spectrum that was detected in the spectral emission window of the CBT core (Figure 6.6b, green solid line) follows the absorption spectrum of compound **1** closely without major deviations. Thus, it incorporates the absorptive channels of the CBT core as well

as those of the peripheral NI. The PL excitation spectrum that was detected in the spectral emission window of the peripheral NI, on the other hand, shows no signal at all (Figure 6.6b, blue solid line). This means that both the absorption of the CBT core and of the peripheral naphthalimides result in PL of the CBT core.

In a control experiment with a mixed solution of reference compounds **3** and **4** (Figure 6.7) the chromophores are on average about 75 nm apart, which renders energy transfer highly unlikely. In this experiment, photoluminescence stems either from the carbonyl bridged triarylamine or from the naphthalimide chromophore (Figure 6.7b, black dashed and black solid line, respectively), depending on which chromophore is addressed at the particular excitation wavelength. The PL excitation spectra that have

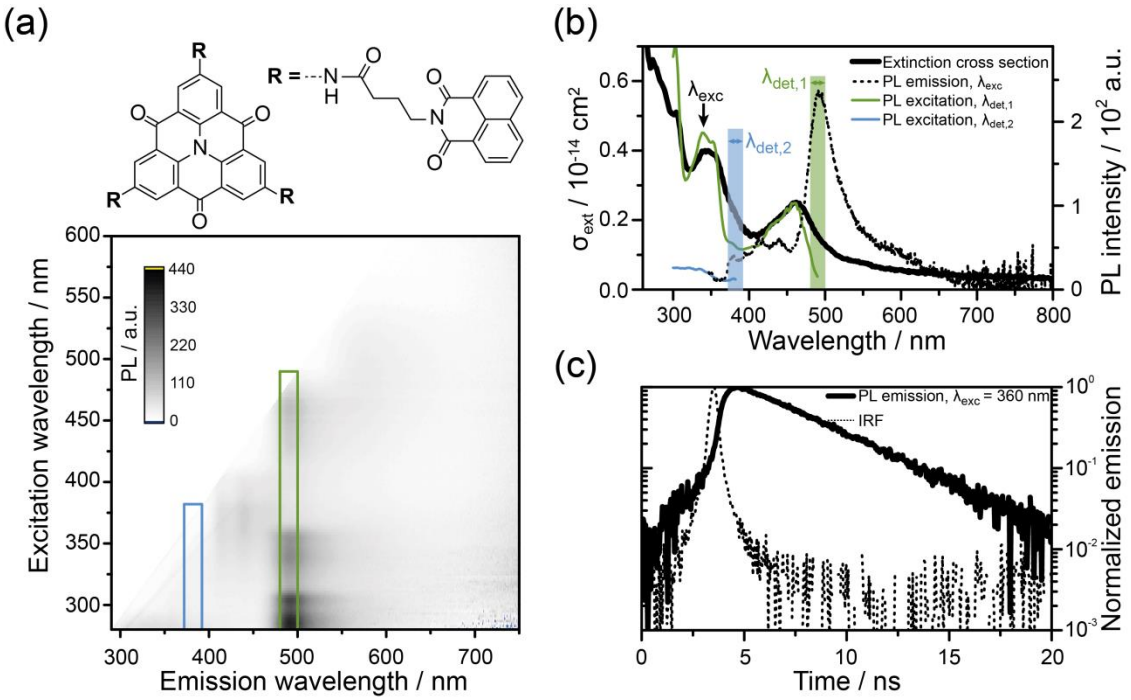

Figure 6.6: Photophysical properties of compound **1** (chemical structure inset in (a)) at a concentration of 1 µM in 1,1,2,2-tetrachloroethane (TCE). a) PL emission map. The spectral signature of the reference compounds **3** and **4** is highlighted by green or blue boxes, respectively. b) Absorbance spectrum given as extinction cross section σ_{ext} (black solid line) and PL excitation spectra detected in the range $\lambda_{det,1} = [480, 500]$ nm (green solid line) and $\lambda_{det,2} = [372, 392]$ nm (blue solid line). An exemplary PL emission spectrum excited at $\lambda_{exc} = 340$ nm is given as black dashed line. c) Time-resolved PL emission of **1** at $\lambda_{exc} = 360$ nm (solid line) and instrument response function (IRF, dashed line) of the experimental setup. Adapted from [181].

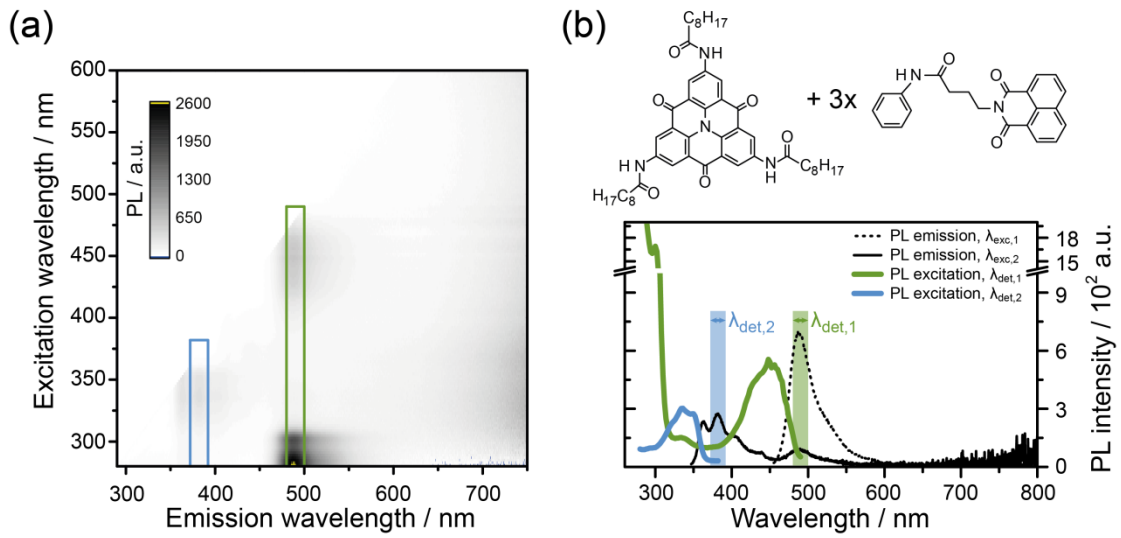

Figure 6.7: Photophysical properties of a mixture of compound **3** at 1 µM with 3 µM of compound **4** (chemical structures inset in (b)) in 1,1,2,2-tetrachloroethane (TCE). a) PL emission map. The spectral signature of the reference compounds **3** and **4** is highlighted by green or blue boxes, respectively. b) PL excitation spectra detected in the range $\lambda_{det,1} = [480, 500]$ nm (green solid line) and $\lambda_{det,2} = [372, 390]$ nm (blue solid line). Exemplary PL emission spectra excited at $\lambda_{exc,1} = 440$ nm and $\lambda_{exc,2} = 340$ nm are given as black dashed and black solid line, respectively. Adapted from [181].

been extracted from the corresponding PL emission map (Figure 6.7a) in the region of the CBT's or the NI's spectral fingerprint (Figure 6.7b, green and blue solid line, respectively) strictly follow the absorbance spectra of the isolated compounds, giving also no hint on energy transfer between compounds **3** and **4** in the mixed solution. These findings suggest that in compound **1**, the energy absorbed by the peripheral naphthalimide (energy donor) is funnelled to the carbonyl-bridged triarylamine core (energy acceptor) by intramolecular energy transfer.

Time-resolved PL measurements provide direct evidence for energy transfer. For these experiments on compound **1**, we excited at 360 nm where the absorption of the naphthalimide is prominent while that of the core is negligible, and integrated the PL spectrally from 450 to 580 nm. The resulting PL decay curve (Figure 6.6c, solid line) features a clear rising component with a time constant of 307 ps followed by a monoexponential decay with a time constant of 3.6 ns. As we almost exclusively excite

the NI periphery, the rising component in the PL transient from the CBT core clearly demonstrates energy transfer from the periphery to the core. We note that the time constant of the decay of compound **1** is longer with respect to reference compound **3**. Presumably, this reflects a change in the dielectric environment owing to the different molecular structure.

The quantum yield of the energy transfer can be estimated according to a standard kinetic model (see Appendix B). The obtained rise time corresponds to the inverse sum of the rates that depopulate the NI exited state $\tau_{rise} = (\Gamma + k_{nr} + k_{trans})^{-1}$ with Γ being the radiative and k_{nr} the non-radiative rate of NI and k_{trans} the transfer rate from NI to CBT. Assuming that for the NI chromophore in reference compound **4** and in compound **1**, Γ and k_{nr} remain constant, we can estimate the energy transfer time to be $(k_{trans})^{-1} = 808\,ps$ and the energy transfer quantum yield from NI to CBT to be $k_{trans}/(k_{trans} + \Gamma + k_{nr}) = 0.38$, with $(\Gamma + k_{nr})^{-1} = 495\,ps$ being the observed lifetime of NI in compound **4**.

Compound **2** shows the characteristic PL signature of the peripheral 4-bithiophene-naphthalimide at around 610 nm when excited at 440 nm (Figure 6.8b, dashed line). Yet, the spectral signature of the CBT core around 492 nm cannot be observed. The PL emission map (Figure 6.8a) shows that this holds true for all employed excitation wavelengths from 280 to 600 nm. As the peripheral NIBT chromophore absorbs over a broad spectral range, it is not possible to exclusively excite the carbonyl-bridged triarylamine. However, the PL excitation spectrum detected in the emission range of the NIBT (600–620 nm, Figure 6.8a orange box and Figure 6.8b, orange line) reproduces the absorption spectrum of compound **2** very well. In contrast, the respective spectrum detected in the PL range of the CBT core (480–500 nm; Figure 6.8a green box and Figure 6.8b, green line) shows no signal at all. Therefore, it can be concluded that the absorption of both chromophores contribute to the emission of the NIBT. Furthermore, in a control experiment on a mixed solution of compounds **3** and **5** (Figure 6.9), where energy transfer can be excluded, an additional PL peak arises at

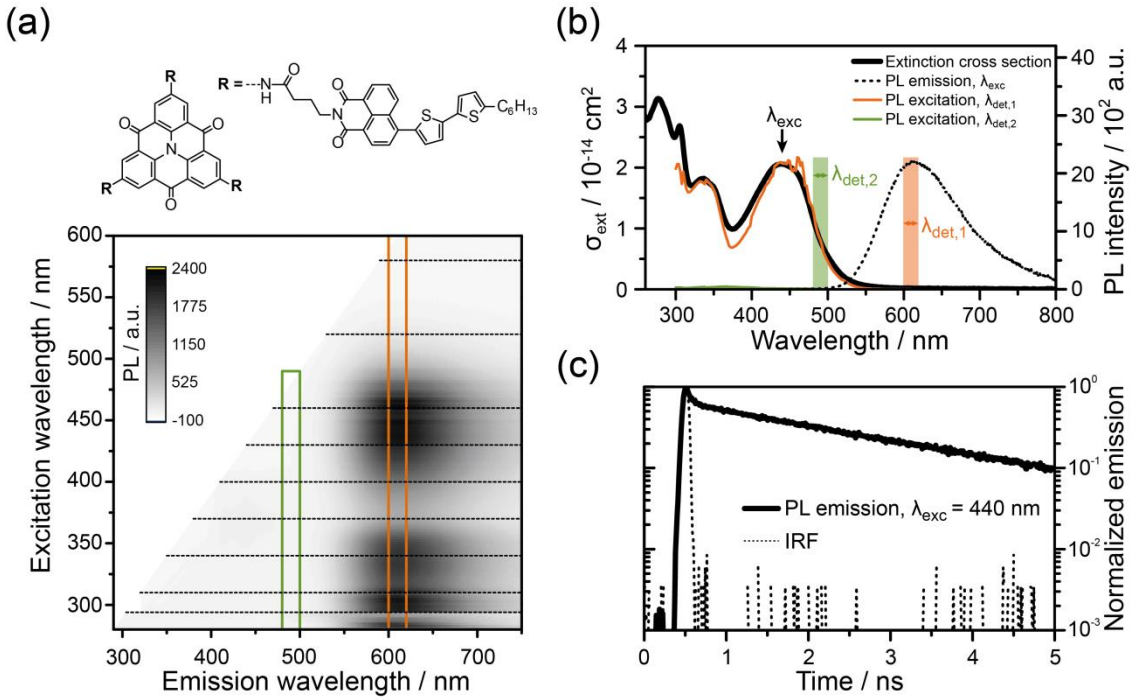

Figure 6.8: Photophysical properties of compound **2** (chemical structure inset in (a)) at a concentration of 1 µM in 1,1,2,2-tetrachloroethane (TCE). a) PL emission map. Horizontal dotted lines mark the replacement of the solution, see text. The spectral signature of the reference compounds **3** and **5** is highlighted by green or orange boxes, respectively. b) Absorbance spectrum given as extinction cross section σ_{ext} (black solid line) and PL excitation spectra detected in the range $\lambda_{det,1} = [600, 620]$ nm (green solid line) and $\lambda_{det,2} = [480, 500]$ nm (orange solid line). An exemplary PL emission spectrum excited at $\lambda_{exc} = 440$ nm is given as black dashed line. c) Time-resolved PL emission of **2** at $\lambda_{exc} = 440$ nm (solid line) and instrument response function (IRF, dashed line) of the experimental setup. Adapted from [181].

around 500 nm that can be clearly assigned to the central carbonyl-bridged triarylamine, after excitation in the absorption regime of that chromophore (Figure 6.9b, dashed line). This peak is not present in the spectra of the multichromophoric compound **2**. The PL excitation spectra extracted from the emission range of the spectral fingerprints of CBT and NIBT (Figure 6.9b, green and orange line, respectively) correspond to those of the respective isolated compounds. No additional peaks arise in the PL excitation spectra of their mixture. These results provide first evidence for an intramolecular energy transfer in compound **2** from the triarylamine core to the peripheral chromophores.

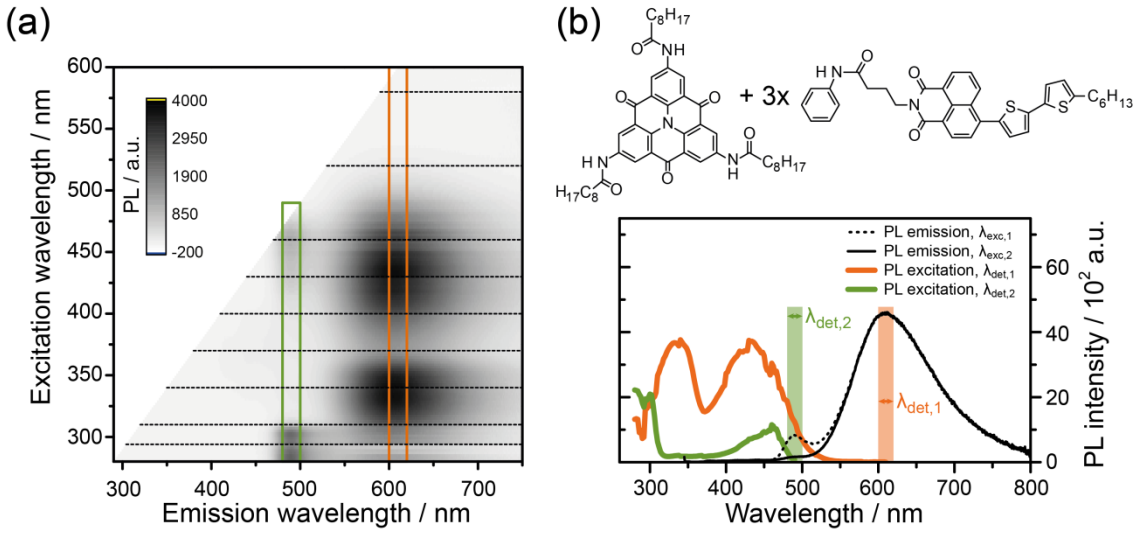

Figure 6.9: Photophysical properties of a mixture of compound **3** at 1 µM with 3 µM of compound **5** (chemical structures inset in (b)) in 1,1,2,2-tetrachloroethane (TCE). a) PL emission map. Horizontal dotted lines mark the replacement of the solution, see text. The spectral signature of the reference compounds **3** and **5** is highlighted by green or orange boxes, respectively. b) PL excitation spectra detected in the range $\lambda_{det,1} = [600, 620]$ nm (green solid line) and $\lambda_{det,2} = [480, 500]$ nm (orange solid line). Exemplary PL emission spectra excited at $\lambda_{exc,1} = 440$ nm and $\lambda_{exc,2} = 340$ nm are given as black dashed and black solid line, respectively. Adapted from [181].

The time-resolved PL transient for compound **2** was recorded upon excitation at 440 nm and spectrally integrated from 480–600 nm, according to the procedure employed for compound **1**. Interpretation of the time-resolved photoluminescence spectrum of compound **2** (Figure 6.8c, solid line) is, however, more challenging. Just like for compound **5**, we find a biexponential transient with decay times of $\tau_1 = 41\,ps$ and $\tau_2 = 2.4\,ns$ with an amplitude ratio of $A_1/A_2 = 1.55$. Within the experimental uncertainty, the values for compounds **2** and **5** are identical. We could not identify a rising component in the transient of **2**. This is due to two factors:

i. The core distributes its energy to three peripheral molecules, which results in a shortening of the rise time.
ii. We simultaneously excite the core and the periphery, where the latter possesses a much larger absorption cross-section.

This is in agreement with a kinetic model (see Appendix B) that predicts a 2- to 6-fold decrease in the amplitude of the rising component of the acceptor chromophore relative to the amplitude of the decay of the donor. Therefore, we cannot determine the efficiency for the transfer from CBT to NIBT in compound **2**. Yet, from steady state spectroscopy, we have evidence that this transfer occurs.

A PL-QY of 10% was found for both multichromophoric compounds **1** and **2**. This is lower compared to the PL-QYs of the reference compounds **3** and **5** representing the respective acceptor chromophore and can be rationalized with the larger molecular structures of **1** and **2**, which enables additional non-radiative relaxation pathways due to structural distortion.

6.4. Conclusion

In this Chapter, we presented the first photophysical characterization of two novel light-harvesting materials based on a carbonyl-bridged triarylamine core. The three-armed multichromophoric systems **1** and **2** comprise next to the carbonyl-bridged triarylamine core either naphthalimides or 4-(5-hexyl-2,2'-bithiophene)-naphthalimides as peripheral chromophores, respectively. Steady-state and time-resolved spectroscopy of **1** and **2** in comparison with three reference compounds **3**–**5** provide clear evidence for energy transfer in both multichromophoric compounds. For system **1**, the energy is funnelled from the peripheral naphthalimides (energy donor) to the carbonyl-bridged triarylamine core (energy acceptor). In the second system (compound **2**), the energy transfer proceeds in the opposite direction; that is, from the carbonyl-bridged triarylamine core (energy donor) to the 4-(5-hexyl-2,2'-bithiophene)-naphthalimides (energy acceptor) in the periphery.

Compound **1** is an excellent example of how man can **imitate** natural concepts. In analogy with the energy funnel concept found in the photosynthetic apparatus of purple bacteria in general (see section 4.1.1) and in their light-harvesting complexes in

particular (see sections 4.1.2 and 5.1.2), the peripheral NI molecules are used to concentrate energy on one central building block, the CBT core. Compound **2** puts a twist on this concept and **evolves** it by reversing the direction of energy transfer from the core to the peripheral molecules. These properties make both compounds interesting materials for the design of organic photovoltaic devices. Moreover, compound **2** displays another astonishing feature. It was found [25] to self-assemble into micrometre-long fibres that show a diameter of the circumference of single CBT-NIBT molecules. When optically excited, these fibres show energy transfer over the whole length of the aggregate at room temperature, making them an ideal model system for the investigation of long range energy-transfer. To understand this phenomenon it will be of crucial importance to not only understand the basic spectroscopic properties of CBT-NIBT, as they are presented here, but to extend this knowledge by detailed time-resolved investigations.

Appendix A

Numerical Input for Figure 4.9b and Figure 4.10b

Table A.1: Data shown in Figure 4.9b and Figure 4.10b. The relative fraction of RC-LH1 complexes that carry one or more triplet excitations is given in blue and the fraction of RC-LH1 complexes with an oxidised special pair (P^+) is given in red. From [45].

Equivalent cw excitation intensity [photons/(s·cm²)]	**Repetition rate**			
	81 MHz	8.1 MHz	810 kHz	81 kHz
$8.1 \cdot 10^{16}$	--	$7.0 \cdot 10^{-6}$ 0.06	$5.0 \cdot 10^{-6}$ 0.06	0.0 0.06
$2.6 \cdot 10^{17}$	--	$2.6 \cdot 10^{-5}$ 0.18	$1.8 \cdot 10^{-5}$ 0.18	0.0 0.17
$8.1 \cdot 10^{17}$	$1.2 \cdot 10^{-4}$ 0.42	$1.1 \cdot 10^{-4}$ 0.42	$7.8 \cdot 10^{-5}$ 0.42	0.0 0.42
$2.6 \cdot 10^{18}$	$5.1 \cdot 10^{-4}$ 0.74	$5.0 \cdot 10^{-4}$ 0.74	$3.5 \cdot 10^{-4}$ 0.75	0.0 0.79
$8.1 \cdot 10^{18}$	$1.9 \cdot 10^{-3}$ 0.94	$1.8 \cdot 10^{-3}$ 0.94	$1.3 \cdot 10^{-3}$ 0.95	0.0 0.96
$2.6 \cdot 10^{19}$	$6.2 \cdot 10^{-3}$ 0.97	$6.0 \cdot 10^{-3}$ 0.97	$4.1 \cdot 10^{-3}$ 0.97	
$8.1 \cdot 10^{19}$	$1.9 \cdot 10^{-2}$ 0.97	$1.9 \cdot 10^{-2}$ 0.97	$9.1 \cdot 10^{-3}$ 0.97	
$2.6 \cdot 10^{20}$	$6.0 \cdot 10^{-2}$ 0.97	$5.8 \cdot 10^{-2}$ 0.97		
$8.1 \cdot 10^{20}$	$1.7 \cdot 10^{-1}$ 0.97	$1.2 \cdot 10^{-1}$ 0.97		
$2.6 \cdot 10^{21}$	$4.4 \cdot 10^{-1}$ 0.97			
$8.1 \cdot 10^{21}$	$6.8 \cdot 10^{-1}$ 0.97			

Simulated Fluorescence Transients in Absence and Presence of Q_B

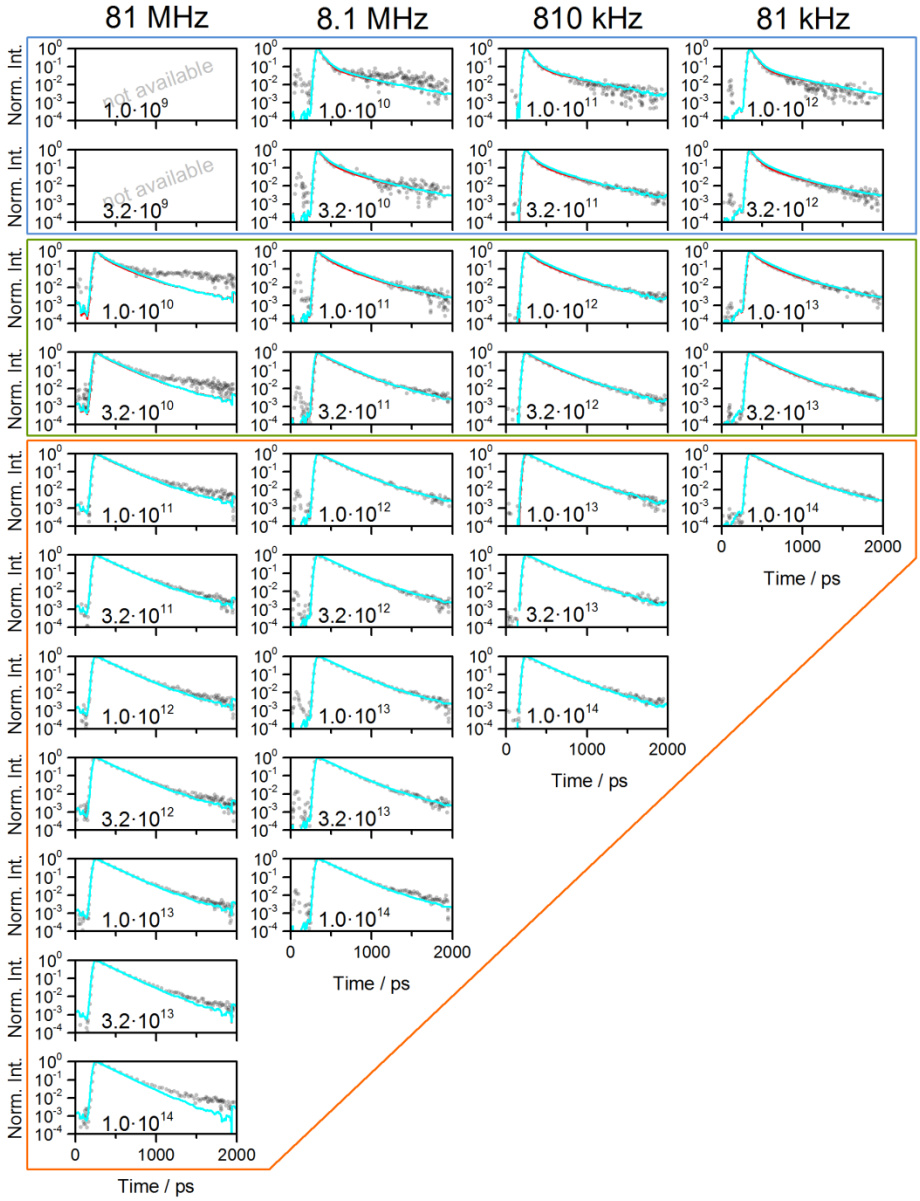

Figure A.1: Normalised fluorescence decays (black dots) of isolated RC-LH1 complexes in detergent solution as a function of the repetition rate (columns) and the photon fluence (rows) of the excitation together with simulated fluorescence decays (red and blue lines). The blue lines refer to simulations in the presence of Q_B using $k'_{51} = (1\ s)^{-1}$. For comparison, the red lines correspond to the simulations as provided in Chapter 4, and which were conducted under the assumption, that Q_B is not present in the samples using $k'_{51} = (100\ ms)^{-1}$. The red lines are barely visible and are almost fully masked by the blue ones. The coloured boxes indicate the range of excitation parameters for which we find from the simulations that the majority of RC-LH1 complexes is in an open state (more than 81% open RCs, blue box), where RCs in the open and closed state coexist (20-80% open RCs, green box) and where RCs in the closed state dominate (below 20% open RCs, orange box). Figure from [45].

Variation of the Fraction of RC-less LH1

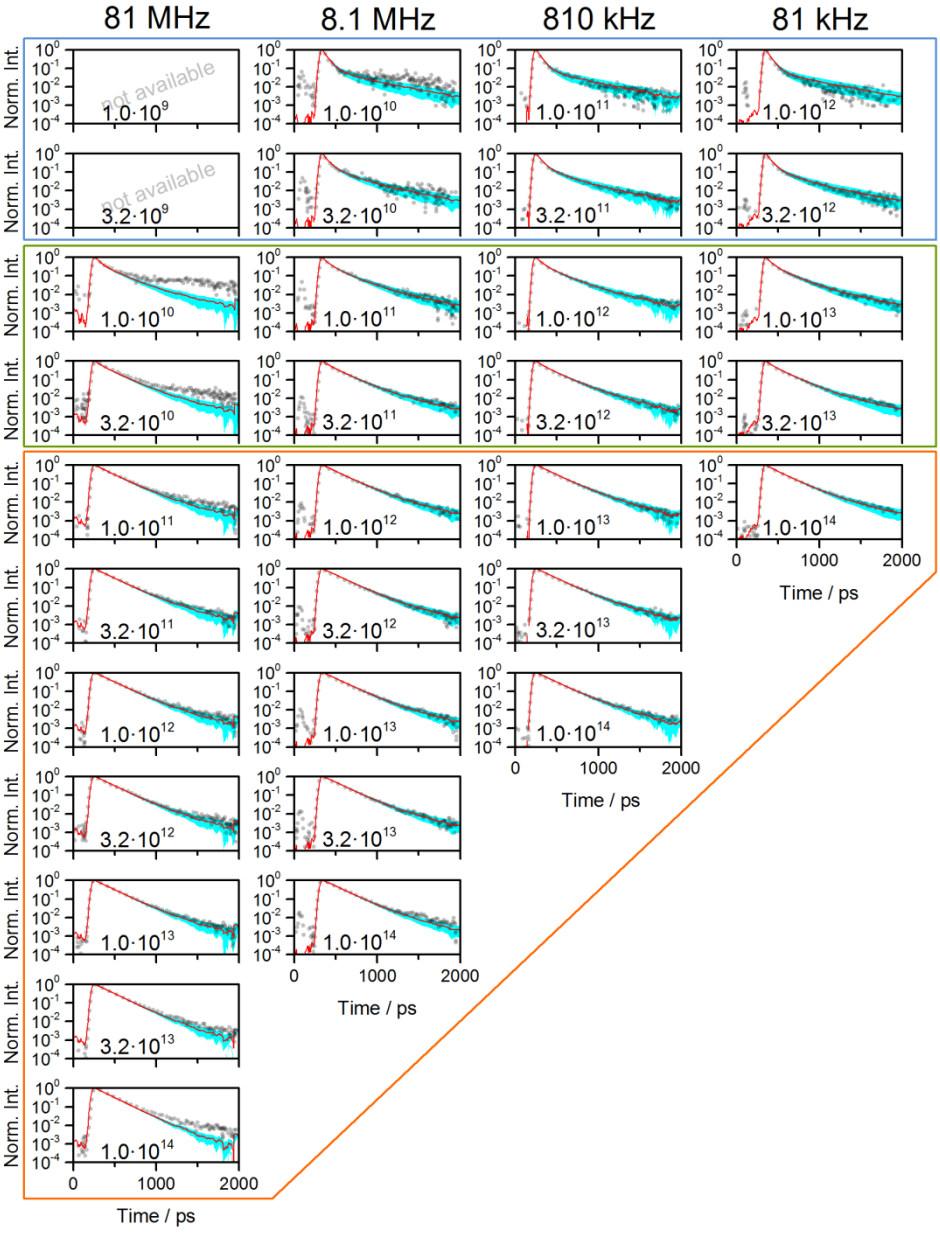

Figure A.2: Normalised fluorescence decays (black dots) of isolated RC-LH1 complexes in detergent solution as a function of the repetition rate (columns) and the photon fluence (rows) of the excitation together with simulated fluorescence decays (red lines and blue hose). The red lines correspond to simulated decays for a fraction of 3% of LH1 rings without RC as provided in Chapter 4. The blue hose gives the outer limits for varying this parameter between 1% and 5%, respectively. The coloured boxes indicate the range of excitation parameters for which we find from the simulations that the majority of RC-LH1 complexes is in an open state (more than 81% open RCs, blue box), where RCs in the open and closed state coexist (20-80% open RCs, green box) and where RCs in the closed state dominate (below 20% open RCs, orange box). Figure from [45].

Variation of the Fraction of Fresh RC-LH1 after Cuvette Revolution

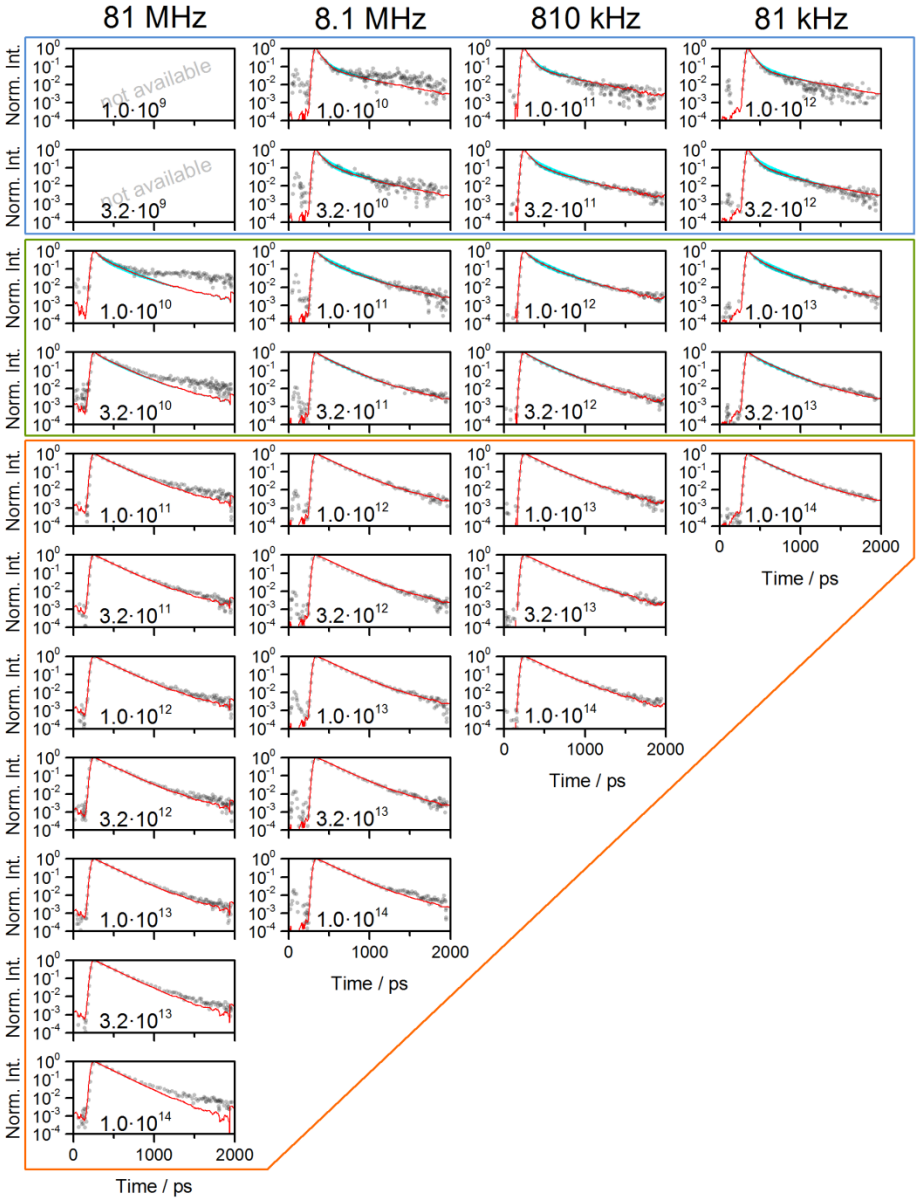

Figure A.3: Normalised fluorescence decays (black dots) of isolated RC-LH1 complexes in detergent solution as a function of the repetition rate (columns) and the photon fluence (rows) of the excitation together with simulated fluorescence decays (red lines and blue hose). The red lines correspond to simulated decays for a fraction of 25% of fresh RC-LH1 complexes that that enter the laser spot after one revolution of the rotating cuvette, as provided in Chapter 4. The blue hose gives the outer limits for varying this parameter between 0 and 50%, respectively. The coloured boxes indicate the range of excitation parameters for which we find from the simulations that the majority of RC-LH1 complexes is in an open state (more than 81% open RCs, blue box), where RCs in the open and closed state coexist (20-80% open RCs, green box) and where RCs in the closed state dominate (below 20% open RCs, orange box). Figure from [45].

Appendix B

Note: This appendix closely follows and in wide parts cites the publication A. T. Haedler, S. R. Beyer, *et al.*, "Synthesis and Photophysical Properties of Multichromophoric Carbonyl-Bridged Triarylamines", *Chemistry - A European Journal*, **20**, 11708-11718 (2014). [181]

A Short Review of Kinetic Models

To describe the time-resolved data of compounds **1** and **2** we used a standard donor-acceptor model as depicted in Figure B.1. In this scheme, the electronic ground (excited) states of the donor and the acceptor are named D (D*) and A (A*). An excitation from the ground to the excited state of the donor (acceptor) occurs via the rate of excitation $k_{exc\,D}$ ($k_{exc\,A}$), while a deexcitation can either occur by emitting a photon with the radiative rate Γ_D (Γ_A) or by nonradiative processes described by the rate $k_{nr\,D}$ ($k_{nr\,A}$). Energy transfer from the excited donor state D* to the excited acceptor state A* can occur with the transfer rate k_T. The time dependent population probabilities of the ground [excited] states of the donor and the acceptor are denoted as· $n_D(t)$ [$n_{D^*}(t)$] and $n_A(t)$ [$n_{A^*}(t)$].

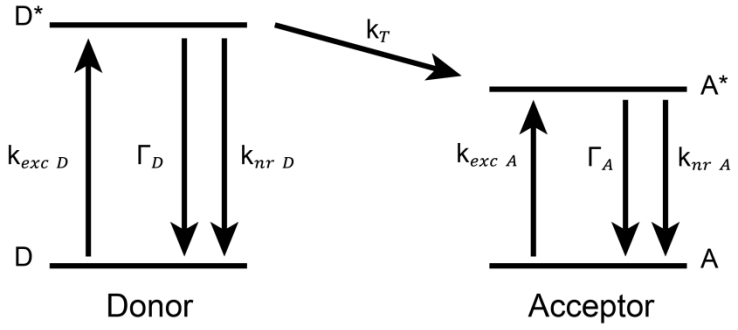

Figure B.1: Sketch of the energy level scheme used in the model for fitting the time resolved decays of compounds **1** and **2**. See text for details. Figure from [181].

Assuming that coherent effects do not play a role, the temporal evolution of the populations can be described by the following set of differential equations:

$$\frac{d}{dt}n_{D^*}(t) = -(\Gamma_D + k_{nr\,D} + k_T)\cdot n_{D^*}(t) + k_{exc\,D}\cdot n_D(t) \qquad \text{B.1}$$

$$\frac{d}{dt}n_{A^*}(t) = -(\Gamma_A + k_{nr\,A})\cdot n_{A^*}(t) + k_T\cdot n_{D^*}(t) + k_{exc\,A}\cdot n_A(t) \qquad \text{B.2}$$

These equations can be simplified by omitting the last term in both equations as we use a pulsed excitation source with a pulse duration that is much shorter than any decay time in our systems. Hence, the initial population probability of the donor and acceptor is set to $n_{D^*}(t=0) = N_{0D^*}$ and $n_{A^*}(t=0) = N_{0A^*}$ (with $N_{0D^*} + N_{0A^*} = 1$), respectively, depending on whether the excitation is resonant with the donor and/or acceptor. Then the solution for the differential equation for $n_{D^*}(t)$ becomes

$$n_{D^*}(t) = N_{0D^*}\cdot e^{-(\Gamma_D + k_{nr\,D} + k_T)\cdot t} = N_{0D^*}\cdot e^{-k_{obs\,D}\cdot t}, \qquad \text{B.3}$$

with $k_{obs\,D} = \Gamma_D + k_{nr\,D} + k_T$ being the effective rate that depopulates the donor D*. With the knowledge of $n_{D^*}(t)$ and defining the effective rate that depopulates the acceptor A* as $k_{obs\,A} = \Gamma_A + k_{nr\,A}$, we find for the time dependence of the A* population

$$n_{A^*}(t) = \left\{N_{0A^*} + N_{0D^*}\cdot\frac{k_T}{k_{obs\,D}+k_{obs\,A}}\right\}\cdot e^{-k_{obs\,A}\cdot t} - N_{0D^*}\cdot\frac{k_T}{k_{obs\,D}+k_{obs\,A}}\cdot e^{-k_{obs\,D}\cdot t}. \qquad \text{B.4}$$

This reflects a biexponential behaviour with the first term describing the decay and the second term the rise of the population of the acceptor excited state.

As we only observe the photoluminescence of the acceptor we limit the following discussion to $n_{A^*}(t)$. We will first consider the situation that we only excite the donor chromophore as for compound **1**, i.e. $n_{D^*}(t=0) = N_{0D^*} = 1$ and $n_{A^*}(t=0) = N_{0A^*} = 0$. Then $n_{A^*}(t)$ simplifies to

$$n_{A^*}(t) = \frac{k_T}{k_{obs\,D}+k_{obs\,A}} \cdot \{e^{-k_{obs\,A}\cdot t} - e^{-k_{obs\,D}\cdot t}\}. \qquad \text{B.5}$$

Importantly, the rate constant obtained for the rise component is $k_{obs\,D} = \Gamma_D + k_{nr\,D} + k_T$, and therefore does not only contain the transfer rate k_T from D* to A*, but all rates that lead to a depopulation of D*. Given that the pure donor lifetime $\Gamma_D + k_{nr\,D}$ is known (e.g. by measurements of reference compounds) and does not change in the presence of the acceptor, the pure transfer rate can be obtained from $k_{obs\,D}$. Notably, the amplitudes of the decaying and rising components are equal.

Second, in the case where the donor as well as the acceptor are excited simultaneously, as for compound **2**, we will accordingly have to apply different initial conditions for N_{0D^*} and N_{0A^*}. Specifically, for compound **2**, where according to the excitation conditions and the absorption cross sections of compounds **3** and **5**, we have a situation with $N_{0D^*} = 0.155$ and $N_{0A^*} = 0.845$. Then it follows for the population of A*:

$$n_{A^*}(t) = \left\{0.845 + 0.155 \cdot \frac{k_T}{k_{obs\,D}+k_{obs\,A}}\right\} \cdot e^{-k_{obs\,A}\cdot t} - 0.155 \cdot \frac{k_T}{k_{obs\,D}+k_{obs\,A}} \cdot e^{-k_{obs\,D}\cdot t}. \qquad \text{B.6}$$

As the donor in compound **2** distributes its energy to three equivalent molecules, each with a rate k_T, we get for the rate constant of the rise component $k_{obs\,D} = \Gamma_D + k_{nr\,D} + 3k_T$. In this case the rising component possesses a high rate due to excess of acceptors. Moreover, the amplitude of the rising component is much smaller than that of the decay component. Hence, resolving the rising component is difficult, if not impossible.

Bibliography

[1] World Energy Council, *World Energy Resources: 2013 Survey* (2013).
[2] BP p.l.c, *BP Statistical Review of World Energy June 2014* (2014).
[3] European Photovoltaic Industry Association, *Global Market Outlook for Photovoltaics 2014-2018* (2014).
[4] National Renewable Energy Laboratory, *NREL Cell Efficiency Chart* (2015).
[5] W. Shockley and H. J. Queisser, J. Appl. Phys. **32**, 510 (1961).
[6] B. O'Regan and M. Grätzel, Nature **353**, 737 (1991).
[7] A. Kojima, K. Teshima, Y. Shirai, and T. Miyasaka, J. Am. Chem. Soc. **131**, 6050 (2009).
[8] R. E. Blankenship, *Molecular Mechanisms of Photosynthesis* (Blackwell Science, Oxford ; Malden, MA, 2002).
[9] M. T. Madigan and D. O. Jung, in *Purple Phototrophic Bact.*, edited by C. N. Hunter, F. Daldal, M. C. Thurnauer, and J. T. Beatty (Springer Science + Business Media B.V., 2009), pp. 1–15.
[10] P. A. Bullough and C. N. Hunter, in *Purple Phototrophic Bact.*, edited by C. N. Hunter, F. Daldal, M. C. Thurnauer, and J. T. Beatty (Springer Science + Business Media B.V., 2009), pp. 155–179.
[11] R. J. Cogdell, A. Gall, and J. Köhler, Q. Rev. Biophys. **39**, 227 (2006).
[12] A. W. Roszak, Science **302**, 1969 (2003).
[13] W. Zinth and J. Wachtveitl, ChemPhysChem **6**, 871 (2005).
[14] M. Z. Papiz, S. M. Prince, T. Howard, R. J. Cogdell, and N. W. Isaacs, J. Mol. Biol. **326**, 1523 (2003).
[15] T. Pullerits and V. Sundström, Acc. Chem. Res. **29**, 381 (1996).
[16] S. Mackowski, S. Wörmke, A. J. Maier, T. H. P. Brotosudarmo, H. Harutyunyan, A. Hartschuh, A. O. Govorov, H. Scheer, and C. Bräuchle, Nano Lett. **8**, 558 (2008).
[17] E. Wientjes, J. Renger, A. G. Curto, R. Cogdell, and N. F. van Hulst, Nat. Commun. **5**, (2014).
[18] P. Anger, P. Bharadwaj, and L. Novotny, Phys. Rev. Lett. **96**, (2006).
[19] P. Bharadwaj, P. Anger, and L. Novotny, Nanotechnology **18**, 044017 (2007).
[20] S. R. Beyer, Biomolekulare Funktionseinheiten Als Bausteine Zur Energiekonversion, Diploma Thesis, Diploma Thesis, University of Bayreuth, 2010.
[21] J. E. Field and D. Venkataraman, Chem. Mater. **14**, 962 (2002).
[22] H. Zhang, Y. Li, X. Wan, and Y. Chen, Chem. Phys. Lett. **479**, 117 (2009).
[23] X. Wan, H. Zhang, Y. Li, and Y. Chen, New J. Chem. **34**, 661 (2010).
[24] M. Kivala, W. Pisula, S. Wang, A. Mavrinskiy, J.-P. Gisselbrecht, X. Feng, and K. Müllen, Chem. – Eur. J. **19**, 8117 (2013).

[25] A. T. Haedler, Synthesis, Self-Assembly and Photophysical Properties of Multichromophoric Systems, Doctoral Thesis, University of Bayreuth, 2015.
[26] H. Haken and H. C. Wolf, *Molekülphysik und Quantenchemie: Einführung in die experimentellen und theoretischen Grundlagen* (Springer, Berlin [u.a.], 2003).
[27] B. Valeur and M. N. Berberan-Santos, *Molecular Fluorescence - Principles and Applications.* (WileyVCH ; John Wiley [distributor], Weinheim; Chichester, 2012).
[28] A. S. Davydov, *Theory of Molecular Excitons* (Plenum Press, 1971).
[29] V. May, *Charge and Energy Transfer Dynamics in Molecular Systems: A Theoretical Introduction*, 1st ed (Wiley-VCH, Berlin ; New York, 2000).
[30] G. D. Scholes, X. J. Jordanides, and G. R. Fleming, J. Phys. Chem. B **105**, 1640 (2001).
[31] S. Jang, M. D. Newton, and R. J. Silbey, Phys. Rev. Lett. **92**, 218301 (2004).
[32] V. Chernyak and S. Mukamel, J. Chem. Phys. **105**, 4565 (1996).
[33] M. Vos, R. van Grondelle, F. W. van der Kooij, D. van de Poll, J. Amesz, and L. N. M. Duysens, Biochim. Biophys. Acta BBA - Bioenerg. **850**, 501 (1986).
[34] A. Freiberg, V. I. Godik, T. Pullerits, and K. Timpman, Biochim. Biophys. Acta BBA - Bioenerg. **973**, 93 (1989).
[35] J. Hofkens, M. Cotlet, T. Vosch, P. Tinnefeld, K. D. Weston, C. Ego, A. Grimsdale, K. Müllen, D. Beljonne, J. L. Brédas, S. Jordens, G. Schweitzer, M. Sauer, and F. D. Schryver, Proc. Natl. Acad. Sci. **100**, 13146 (2003).
[36] G. S. Beddard and G. Porter, Biochim. Biophys. Acta BBA - Bioenerg. **462**, 63 (1977).
[37] L. Valkunas, E. Akesson, T. Pullerits, and V. Sundström, Biophys. J. **70**, 2373 (1996).
[38] V. M. Kenkre and D. Schmid, Chem. Phys. Lett. **94**, 603 (1983).
[39] L. Valkunas, G. Trinkunas, V. Liuolia, and R. van Grondelle, Biophys. J. **69**, 1117 (1995).
[40] L. Novotny, *Principles of Nano-Optics*, 2nd ed (Cambridge University Press, Cambridge, 2012).
[41] C. Sönnichsen, Plasmons in Metal Nanostructures, Doctoral Thesis, Ludwig-Maximilians-University of Munich, 2001.
[42] Hamamatsu Photonics, *Guide to Streak Cameras* (2008).
[43] J. R. Lakowicz, *Principles of Fluorescence Spectroscopy*, 3rd ed (Springer, New York, 2006).
[44] Hamamatsu Photonics, *Test Report, Model C5680-24, Serial 580205, Jan. 30th* (2006).
[45] S. R. Beyer, L. Müller, J. Southall, R. J. Cogdell, G. M. Ullmann, and J. Köhler, J. Phys. Chem. B **119**, 1362 (2015).
[46] W. Kühlbrandt, Structure **3**, 521 (1995).
[47] N. Pfennig, Annu. Rev. Microbiol. **21**, 285 (1967).
[48] G. McDermott, S. M. Prince, A. A. Freer, A. M. Hawthornthwaite-Lawless, M. Z. Papiz, R. J. Cogdell, and N. W. Isaacs, Nature **374**, 517 (1995).

[49] K. McLuskey, S. M. Prince, R. J. Cogdell, and N. W. Isaacs, Biochemistry (Mosc.) **40**, 8783 (2001).
[50] J. Koepke, X. Hu, C. Muenke, K. Schulten, and H. Michel, Structure **4**, 581 (1996).
[51] S. Scheuring, R. P. Gonçalves, V. Prima, and J. N. Sturgis, J. Mol. Biol. **358**, 83 (2006).
[52] P. Qian, C. Neil Hunter, and P. A. Bullough, J. Mol. Biol. **349**, 948 (2005).
[53] S. Niwa, L.-J. Yu, K. Takeda, Y. Hirano, T. Kawakami, Z.-Y. Wang-Otomo, and K. Miki, Nature **508**, 228 (2014).
[54] C. N. Hunter, D. Fevzi, M. C. Thurnauer, and J. T. Beatty, editors , *The Purple Phototrophic Bacteria* (Springer, 2008).
[55] J. M. Berg, J. L. Tymoczko, and L. Stryer, *Stryer Biochemie* (Spektrum, Heidelberg, 2012).
[56] S. Scheuring, J. Busselez, and D. Levy, J. Biol. Chem. **280**, 1426 (2005).
[57] P. Qian, P. A. Bullough, and C. N. Hunter, J. Biol. Chem. **283**, 14002 (2008).
[58] M. F. Richter, J. Baier, T. Prem, S. Oellerich, F. Francia, G. Venturoli, D. Oesterhelt, J. Southall, R. J. Cogdell, and J. Köhler, Proc. Natl. Acad. Sci. **104**, 6661 (2007).
[59] M. F. Richter, J. Baier, J. Southall, R. J. Cogdell, S. Oellerich, and J. Köhler, Proc. Natl. Acad. Sci. **104**, 20280 (2007).
[60] J. Deisenhofer, O. Epp, K. Miki, R. Huber, and H. Michel, Nature **318**, 618 (1985).
[61] J. P. Allen, G. Feher, T. O. Yeates, H. Komiya, and D. C. Rees, Proc. Natl. Acad. Sci. **84**, 6162 (1987).
[62] J. Koepke, E.-M. Krammer, A. R. Klingen, P. Sebban, G. M. Ullmann, and G. Fritzsch, J. Mol. Biol. **371**, 396 (2007).
[63] G. Feher, J. P. Allen, M. Y. Okamura, and D. C. Rees, Nature **339**, 111 (1989).
[64] W. D. Swingley, R. E. Blankenship, and J. Raymond, in *Purple Phototrophic Bact.*, edited by C. N. Hunter, F. Daldal, M. C. Thurnauer, and J. T. Beatty (Springer Science + Business Media B.V., 2009), pp. 17–29.
[65] V. Yurkov and J. T. Csotonyi, in *Purple Phototrophic Bact.*, edited by C. N. Hunter, F. Daldal, M. C. Thurnauer, and J. T. Beatty (Springer Science + Business Media B.V., 2009), pp. 31–55.
[66] U. Ermler, G. Fritzsch, S. K. Buchanan, and H. Michel, Structure **2**, 925 (1994).
[67] T. L. Olson, J. C. Williams, and J. P. Allen, Photosynth. Res. **120**, 87 (2014).
[68] P. S. Böhm, J. Southall, R. J. Cogdell, and J. Köhler, J. Phys. Chem. B **117**, 3120 (2013).
[69] S. I. E. Vulto, J. T. M. Kennis, A. M. Streltsov, J. Amesz, and T. J. Aartsma, J. Phys. Chem. B **103**, 878 (1999).
[70] R. J. Cogdell and H. A. Frank, Biochim. Biophys. Acta BBA - Rev. Bioenerg. **895**, 63 (1987).
[71] H. A. Frank and R. J. Cogdell, Photochem. Photobiol. **63**, 257 (1996).
[72] K. Möbius, W. Lubitz, and A. Savitsky, Appl. Magn. Reson. **41**, 113 (2011).
[73] A. van der Est, F. Reiss-Husson, and D. Stehlik, Photosynth. Res. **55**, 217 (1998).

[74] T. F. Prisner, A. van der Est, R. Bittl, W. Lubitz, D. Stehlik, and K. Möbius, Chem. Phys. **194**, 361 (1995).
[75] A. Marchanka, M. Paddock, W. Lubitz, and M. van Gastel, Biochemistry (Mosc.) **46**, 14782 (2007).
[76] R. Bittl and S. G. Zech, J. Phys. Chem. B **101**, 1429 (1997).
[77] R. Bittl and S. Weber, Biochim. Biophys. Acta BBA - Bioenerg. **1707**, 117 (2005).
[78] J. Fajer, D. C. Brune, M. S. Davis, A. Forman, and L. D. Spaulding, Proc. Natl. Acad. Sci. **72**, 4956 (1975).
[79] U. Finkele, C. Lauterwasser, W. Zinth, K. A. Gray, and D. Oesterhelt, Biochemistry (Mosc.) **29**, 8517 (1990).
[80] H. U. Stilz, U. Finkele, W. Holzapfel, C. Lauterwasser, W. Zinth, and D. Oesterhelt, Eur. J. Biochem. **223**, 233 (1994).
[81] P. N. Dominguez, M. Himmelstoss, J. Michelmann, F. T. Lehner, A. T. Gardiner, R. J. Cogdell, and W. Zinth, Chem. Phys. Lett. **601**, 103 (2014).
[82] L. M. P. Beekman, R. W. Visschers, R. Monshouwer, M. Heer-Dawson, T. A. Mattioli, P. McGlynn, C. N. Hunter, B. Robert, and I. H. M. van Stokkum, Biochemistry (Mosc.) **34**, 14712 (1995).
[83] G. R. Fleming, J. L. Martin, and J. Breton, Nature **333**, 190 (1988).
[84] J. C. Williams, R. G. Alden, H. A. Murchison, J. M. Peloquin, N. W. Woodbury, and J. P. Allen, Biochemistry (Mosc.) **31**, 11029 (1992).
[85] M. Meyer and H. Scheer, Photosynth. Res. **44**, 55 (1995).
[86] V. Sundström, T. Pullerits, and R. van Grondelle, J. Phys. Chem. B **103**, 2327 (1999).
[87] W. J. Vredenberg and L. N. M. Duysens, Nature **197**, 355 (1963).
[88] R. K. Clayton, Photochem. Photobiol. **5**, 679 (1966).
[89] P. Heathcote and R. K. Clayton, Biochim. Biophys. Acta BBA - Bioenerg. **459**, 506 (1977).
[90] A. Y. Borisov and V. I. Godik, J. Bioenerg. **3**, 211 (1972).
[91] V. I. Godik and A. Y. Borisov, FEBS Lett. **82**, 355 (1977).
[92] T. Ritz, S. Park, and K. Schulten, J. Phys. Chem. B **105**, 8259 (2001).
[93] J. Strümpfer and K. Schulten, J. Chem. Phys. **137**, 065101 (2012).
[94] K. J. Visscher, H. Bergström, V. Sundström, C. N. Hunter, and R. V. Grondelle, Photosynth. Res. **22**, 211 (1989).
[95] H. Bergström, R. van Grondelle, and V. Sundström, FEBS Lett. **250**, 503 (1989).
[96] L. Valkunas, V. Liuolia, and A. Freiberg, Photosynth. Res. **27**, 83 (1991).
[97] R. van Grondelle, J. P. Dekker, T. Gillbro, and V. Sundstrom, Biochim. Biophys. Acta BBA - Bioenerg. **1187**, 1 (1994).
[98] K. Timpmann, F. G. Zhang, A. Freiberg, and V. Sundström, Biochim. Biophys. Acta BBA - Bioenerg. **1183**, 185 (1993).
[99] K. Timpmann, A. Freiberg, and V. Sundström, Chem. Phys. **194**, 275 (1995).
[100] W. Xiao, S. Lin, A. K. W. Taguchi, and N. W. Woodbury, Biochemistry (Mosc.) **33**, 8313 (1994).

[101] K. Bernhardt and H.-W. Trissl, Biochim. Biophys. Acta BBA - Bioenerg. **1457**, 1 (2000).
[102] I. A. Abdourakhmanov, R. V. Danielius, and A. P. Razjivin, FEBS Lett. **245**, 47 (1989).
[103] A. Freiberg, V. I. Godik, T. Pullerits, and K. Timpman, Biochim. Biophys. Acta BBA - Bioenerg. **973**, 93 (1989).
[104] P. Sebban and I. Moya, Biochim. Biophys. Acta BBA - Bioenerg. **722**, 436 (1983).
[105] V. Sundström, R. van Grondelle, H. Bergström, E. Åkesson, and T. Gillbro, Biochim. Biophys. Acta BBA - Bioenerg. **851**, 431 (1986).
[106] A. Freiberg, in *Anoxigenic Photosynth. Bact.*, edited by R. E. Blankenship, M. T. Madigan, and C. E. Bauer (Kluwer Academic Publishers, 1995), pp. 385–398.
[107] R. van Grondelle, H. Bergström, V. Sundström, and T. Gillbro, Biochim. Biophys. Acta BBA - Bioenerg. **894**, 313 (1987).
[108] A. Freiberg, J. P. Allen, J. C. Williams, and N. W. Woodbury, Photosynth. Res. **48**, 309 (1996).
[109] P. Sebban, G. Jolchine, and I. Moya, Photochem. Photobiol. **39**, 247 (1984).
[110] A. Freiberg and K. Timpmann, J. Photochem. Photobiol. B **15**, 151 (1992).
[111] K. Timpmann, A. Freiberg, and V. I. Godik, Chem. Phys. Lett. **182**, 617 (1991).
[112] A. Y. Borisov, A. . Freiberg, V. . Godik, K. . Rebane, and K. . Timpmann, Biochim. Biophys. Acta BBA - Bioenerg. **807**, 221 (1985).
[113] A. D. Stahl, L. I. Crouch, M. R. Jones, I. van Stokkum, R. van Grondelle, and M. L. Groot, J. Phys. Chem. B **116**, 434 (2012).
[114] T. J. Pflock, S. Oellerich, J. Southall, R. J. Cogdell, G. M. Ullmann, and J. Köhler, J. Phys. Chem. B **115**, 8813 (2011).
[115] T. J. Pflock, S. Oellerich, L. Krapf, J. Southall, R. J. Cogdell, G. M. Ullmann, and J. Köhler, J. Phys. Chem. B **115**, 8821 (2011).
[116] R. K. Clayton, Photochem. Photobiol. **5**, 669 (1966).
[117] T. Becker, R. T. Ullmann, and G. M. Ullmann, J. Phys. Chem. B **111**, 2957 (2007).
[118] E. Bombarda and G. M. Ullmann, Faraday Discuss. **148**, 173 (2011).
[119] M. G. Müller, G. Drews, and A. R. Holzwarth, Biochim. Biophys. Acta BBA - Bioenerg. **1142**, 49 (1993).
[120] C. J. Law and R. J. Cogdell, FEBS Lett. **432**, 27 (1998).
[121] G. Trinkunas, J. Herek, T. Polívka, V. Sundström, and T. Pullerits, Phys. Rev. Lett. **86**, 4167 (2001).
[122] T. G. Monger, R. J. Cogdell, and W. W. Parson, Biochim. Biophys. Acta BBA - Bioenerg. **449**, 136 (1976).
[123] F. Juan, L. Xue-feng, and L. Yuan, Spectrosc. Spectr. Anal. **28**, 1459 (2008).
[124] Y. Kakitani, J. Akahane, H. Ishii, H. Sogabe, H. Nagae, and Y. Koyama, Biochemistry (Mosc.) **46**, 2181 (2007).
[125] R. Bittl, E. Schlodder, I. Geisenheimer, W. Lubitz, and R. J. Cogdell, J. Phys. Chem. B **105**, 5525 (2001).

[126] M. S. Graige, G. Feher, and M. Y. Okamura, Proc. Natl. Acad. Sci. U. S. A. **95**, 11679 (1998).
[127] V. P. Shinkarev and C. A. Wraight, in *Photosynth. React. Cent. Vol. I*, edited by J. Deisenhofer and J. R. Norris (Academic Press Inc., 1993), pp. 193–256.
[128] J. I. Chuang, S. G. Boxer, D. Holten, and C. Kirmaier, Biochemistry (Mosc.) **45**, 3845 (2006).
[129] B. Carter, S. G. Boxer, D. Holten, and C. Kirmaier, Biochemistry (Mosc.) **48**, 2571 (2009).
[130] J. Pan, S. Lin, and N. W. Woodbury, J. Phys. Chem. B **116**, 2014 (2012).
[131] S. R. Beyer, S. Ullrich, S. Kudera, A. T. Gardiner, R. J. Cogdell, and J. Köhler, Nano Lett **11**, 4897 (2011).
[132] N. Nagata, Y. Kuramochi, and Y. Kobuke, J. Am. Chem. Soc. **131**, 10 (2009).
[133] S. Uemura, S. Sengupta, and F. Würthner, Angew. Chem. **121**, 7965 (2009).
[134] S. Sengupta, S. Uemura, S. Patwardhan, V. Huber, F. C. Grozema, L. D. A. Siebbeles, U. Baumeister, and F. Würthner, Chem. - Eur. J. **17**, 5300 (2011).
[135] T. S. Balaban, Acc. Chem. Res. **38**, 612 (2005).
[136] N. Lebedev, S. A. Trammell, S. Tsoi, A. Spano, J. H. Kim, J. Xu, M. E. Twigg, and J. M. Schnur, Langmuir **24**, 8871 (2008).
[137] I. Oda, M. Iwaki, D. Fujita, Y. Tsutsui, S. Ishizaka, M. Dewa, M. Nango, T. Kajino, Y. Fukushima, and S. Itoh, Langmuir **26**, 13399 (2010).
[138] M. Escalante, Y. Zhao, M. J. W. Ludden, R. Vermeij, J. D. Olsen, E. Berenschot, C. N. Hunter, J. Huskens, V. Subramaniam, and C. Otto, J. Am. Chem. Soc. **130**, 8892 (2008).
[139] R. A. Grimme, C. E. Lubner, D. A. Bryant, and J. H. Golbeck, J. Am. Chem. Soc. **130**, 6308 (2008).
[140] H. P. Lang and C. N. Hunter, Biochem. J. **298 (Pt 1)**, 197 (1994).
[141] T. Walz, S. J. Jamieson, C. M. Bowers, P. A. Bullough, and C. N. Hunter, J. Mol. Biol. **282**, 833 (1998).
[142] J. T. M. Kennis, A. M. Streltsov, S. I. E. Vulto, T. J. Aartsma, T. Nozawa, and J. Amesz, J. Phys. Chem. B **101**, 7827 (1997).
[143] J. M. Salverda, F. van Mourik, G. van der Zwan, and R. van Grondelle, J. Phys. Chem. B **104**, 11395 (2000).
[144] M. H. C. Koolhaas, R. N. Frese, G. J. S. Fowler, T. S. Bibby, S. Georgakopoulou, G. van der Zwan, C. N. Hunter, and R. van Grondelle, Biochemistry (Mosc.) **37**, 4693 (1998).
[145] J. Linnanto, J. E. I. Korppi-Tommola, and V. M. Helenius, J. Phys. Chem. B **103**, 8739 (1999).
[146] M. Ketelaars, A. M. van Oijen, M. Matsushita, J. Köhler, J. Schmidt, and T. J. Aartsma, Biophys. J. **80**, 1591 (2001).
[147] R. Hildner, D. Brinks, J. B. Nieder, R. J. Cogdell, and N. F. van Hulst, Science **340**, 1448 (2013).
[148] G. D. Scholes and G. R. Fleming, J. Phys. Chem. B **104**, 1854 (2000).
[149] E. Dulkeith, M. Ringler, T. A. Klar, J. Feldmann, A. Muñoz Javier, and W. J. Parak, Nano Lett. **5**, 585 (2005).

[150] O. L. Muskens, V. Giannini, J. A. Sánchez-Gil, and J. Gómez Rivas, Nano Lett. **7**, 2871 (2007).
[151] P. Bharadwaj, R. Beams, and L. Novotny, Chem. Sci. **2**, 136 (2011).
[152] C. Sönnichsen, T. Franzl, T. Wilk, G. von Plessen, and J. Feldmann, New J. Phys. **4**, 93.1 (2002).
[153] O. Schubert, J. Becker, L. Carbone, Y. Khalavka, T. Provalska, I. Zins, and C. Sönnichsen, Nano Lett. **8**, 2345 (2008).
[154] C. Sönnichsen, T. Franzl, T. Wilk, G. von Plessen, and J. Feldmann, Phys. Rev. Lett. **88**, (2002).
[155] Y. Chen, K. Munechika, I. Jen-La Plante, A. M. Munro, S. E. Skrabalak, Y. Xia, and D. S. Ginger, Appl. Phys. Lett. **93**, 053106 (2008).
[156] A. Bek, R. Jansen, M. Ringler, S. Mayilo, T. A. Klar, and J. Feldmann, Nano Lett. **8**, 485 (2008).
[157] Y. Chen, K. Munechika, and D. S. Ginger, Nano Lett. **7**, 690 (2007).
[158] C. L. Baciu, J. Becker, A. Janshoff, and C. Sönnichsen, Nano Lett. **8**, 1724 (2008).
[159] C. Sönnichsen, B. M. Reinhard, J. Liphardt, and A. P. Alivisatos, Nat Biotech **23**, 741 (2005).
[160] N. Liu, M. Hentschel, T. Weiss, A. P. Alivisatos, and H. Giessen, Science **332**, 1407 (2011).
[161] I. Carmeli, I. Lieberman, L. Kraversky, Z. Fan, A. O. Govorov, G. Markovich, and S. Richter, Nano Lett. **10**, 2069 (2010).
[162] J. B. Nieder, R. Bittl, and M. Brecht, Angew. Chem. **122**, 10415 (2010).
[163] H. Chen, L. Shao, Q. Li, and J. Wang, Chem. Soc. Rev. **42**, 2679 (2013).
[164] A. Kinkhabwala, Z. Yu, S. Fan, Y. Avlasevich, K. Mullen, and MoernerW. E., Nat Photon **3**, 654 (2009).
[165] P. Biagioni, J.-S. Huang, and B. Hecht, Rep. Prog. Phys. **75**, 024402 (2012).
[166] R. Glass, M. Müller, and J. P. Spatz, Nanotechnology **14**, 1153 (2003).
[167] S. Ullrich, S. P. Scheeler, C. Pacholski, J. P. Spatz, and S. Kudera, Part. Part. Syst. Charact. **30**, 102 (2013).
[168] A. B. Taylor, P. Michaux, A. S. M. Mohsin, and J. W. M. Chon, Opt. Express **22**, 13234 (2014).
[169] C. Kuemin, L. Nowack, L. Bozano, N. D. Spencer, and H. Wolf, Adv. Funct. Mater. **22**, 702 (2012).
[170] P. J. Schuck, D. P. Fromm, A. Sundaramurthy, G. S. Kino, and W. E. Moerner, Phys. Rev. Lett. **94**, 017402 (2005).
[171] D. P. Fromm, A. Sundaramurthy, P. J. Schuck, G. Kino, and W. E. Moerner, Nano Lett **4**, 957 (2004).
[172] A. T. Gardiner, R. J. Cogdell, and S. Takaichi, Photosynth. Res. **38**, 159 (1993).
[173] M. A. van Dijk, A. L. Tchebotareva, M. Orrit, M. Lippitz, S. Berciaud, D. Lasne, L. Cognet, and B. Lounis, Phys. Chem. Chem. Phys. **8**, 3486 (2006).
[174] A. O. Govorov and I. Carmeli, Nano Lett. **7**, 620 (2007).
[175] P. B. Johnson and R. W. Christy, Phys. Rev. B **6**, 4370 (1972).

[176] J. Adams, G. Tizazu, S. Janusz, S. R. J. Brueck, G. P. Lopez, and G. J. Leggett, Langmuir **26**, 13600 (2010).
[177] E. Wientjes, J. Renger, A. G. Curto, R. Cogdell, and N. F. van Hulst, Phys. Chem. Chem. Phys. **16**, 24739 (2014).
[178] Ł. Bujak, M. Olejnik, T. H. P. Brotosudarmo, M. K. Schmidt, N. Czechowski, D. Piatkowski, J. Aizpurua, R. J. Cogdell, W. Heiss, and S. Mackowski, Phys. Chem. Chem. Phys. **16**, 9015 (2014).
[179] X. Yu, D. Y. Lei, F. Amin, R. Hartmann, G. P. Acuna, A. Guerrero-Martínez, S. A. Maier, P. Tinnefeld, S. Carregal-Romero, and W. J. Parak, Nano Today **8**, 480 (2013).
[180] O. Andreussi, A. Biancardi, S. Corni, and B. Mennucci, Nano Lett. **13**, 4475 (2013).
[181] A. T. Haedler, S. R. Beyer, N. Hammer, R. Hildner, M. Kivala, J. Köhler, and H.-W. Schmidt, Chem. – Eur. J. **20**, 11708 (2014).
[182] M. Hasegawa and M. Iyoda, Chem. Soc. Rev. **39**, 2420 (2010).
[183] A. A. Sagade, K. V. Rao, U. Mogera, S. J. George, A. Datta, and G. U. Kulkarni, Adv. Mater. **25**, 559 (2013).
[184] R. J. Cogdell and J. Köhler, in *Semicond. Semimet.*, edited by M. T. and U. W. Eicke R. Weber (Elsevier, 2010), pp. 77–94.
[185] X. Zhan, A. Facchetti, S. Barlow, T. J. Marks, M. A. Ratner, M. R. Wasielewski, and S. R. Marder, Adv. Mater. **23**, 268 (2011).
[186] F. Schlosser, J. Sung, P. Kim, D. Kim, and F. Würthner, Chem. Sci. **3**, 2778 (2012).
[187] W. Yue, A. Lv, J. Gao, W. Jiang, L. Hao, C. Li, Y. Li, L. E. Polander, S. Barlow, W. Hu, S. Di Motta, F. Negri, S. R. Marder, and Z. Wang, J. Am. Chem. Soc. **134**, 5770 (2012).
[188] L. F. Dössel, V. Kamm, I. A. Howard, F. Laquai, W. Pisula, X. Feng, C. Li, M. Takase, T. Kudernac, S. De Feyter, and K. Müllen, J. Am. Chem. Soc. **134**, 5876 (2012).
[189] E. Lang, R. Hildner, H. Engelke, P. Osswald, F. Würthner, and J. Köhler, ChemPhysChem **8**, 1487 (2007).
[190] A. Issac, R. Hildner, D. Ernst, C. Hippius, F. Würthner, and J. Köhler, Phys. Chem. Chem. Phys. **14**, 10789 (2012).
[191] A. Issac, R. Hildner, C. Hippius, F. Würthner, and J. Köhler, ACS Nano **8**, 1708 (2014).
[192] D. M. Guldi, Chem. Commun. 321 (2000).
[193] F. Giacalone and N. Martín, Adv. Mater. **22**, 4220 (2010).
[194] H. C. Hesse, J. Weickert, C. Hundschell, X. Feng, K. Müllen, B. Nickel, A. J. Mozer, and L. Schmidt-Mende, Adv. Energy Mater. **1**, 861 (2011).
[195] L. Feng, M. Rudolf, S. Wolfrum, A. Troeger, Z. Slanina, T. Akasaka, S. Nagase, N. Martín, T. Ameri, C. J. Brabec, and D. M. Guldi, J. Am. Chem. Soc. **134**, 12190 (2012).
[196] C. C. Hofmann, S. M. Lindner, M. Ruppert, A. Hirsch, S. A. Haque, M. Thelakkat, and J. Köhler, J. Phys. Chem. B **114**, 9148 (2010).

[197] C. C. Hofmann, S. M. Lindner, M. Ruppert, A. Hirsch, S. A. Haque, M. Thelakkat, and J. Köhler, Phys. Chem. Chem. Phys. **12**, 14485 (2010).
[198] H. Imahori, T. Umeyama, K. Kurotobi, and Y. Takano, Chem. Commun. **48**, 4032 (2012).
[199] T. Hasobe, J. Phys. Chem. Lett. **4**, 1771 (2013).
[200] F. D'Souza, A. N. Amin, M. E. El-Khouly, N. K. Subbaiyan, M. E. Zandler, and S. Fukuzumi, J. Am. Chem. Soc. **134**, 654 (2011).
[201] Á. J. Jiménez, R. M. K. Calderón, M. S. Rodríguez-Morgade, D. M. Guldi, and T. Torres, Chem. Sci. **4**, 1064 (2013).
[202] J. R. Pinzón, D. C. Gasca, S. G. Sankaranarayanan, G. Bottari, T. Torres, D. M. Guldi, and L. Echegoyen, J. Am. Chem. Soc. **131**, 7727 (2009).
[203] J. L. Segura, H. Herrera, and P. Bäuerle, J. Mater. Chem. **22**, 8717 (2012).
[204] C. A. Wijesinghe, M. E. El-Khouly, M. E. Zandler, S. Fukuzumi, and F. D'Souza, Chem. – Eur. J. **19**, 9629 (2013).
[205] E. Fron, L. Puhl, I. Oesterling, C. Li, K. Müllen, F. C. De Schryver, J. Hofkens, and T. Vosch, ChemPhysChem **12**, 595 (2011).
[206] M. A. Oar, W. R. Dichtel, J. M. Serin, J. M. J. Fréchet, J. E. Rogers, J. E. Slagle, P. A. Fleitz, L.-S. Tan, T. Y. Ohulchanskyy, and P. N. Prasad, Chem. Mater. **18**, 3682 (2006).
[207] W. R. Dichtel, S. Hecht, and J. M. J. Fréchet, Org. Lett. **7**, 4451 (2005).
[208] R. Hildner, U. Lemmer, U. Scherf, M. van Heel, and J. Köhler, Adv. Mater. **19**, 1978 (2007).
[209] T. Adachi, G. Lakhwani, M. C. Traub, R. J. Ono, C. W. Bielawski, P. F. Barbara, and D. A. Vanden Bout, J. Phys. Chem. B **116**, 9866 (2012).
[210] A. Thiessen, J. Vogelsang, T. Adachi, F. Steiner, D. V. Bout, and J. M. Lupton, Proc. Natl. Acad. Sci. **110**, E3550 (2013).
[211] E. Fron, A. Deres, S. Rocha, G. Zhou, K. Müllen, F. C. De Schryver, M. Sliwa, H. Uji-i, J. Hofkens, and T. Vosch, J. Phys. Chem. B **114**, 1277 (2010).
[212] E. Lang, A. Sorokin, M. Drechsler, Y. V. Malyukin, and J. Köhler, Nano Lett. **5**, 2635 (2005).
[213] X. Zhang, D. Görl, and F. Würthner, Chem. Commun. **49**, 8178 (2013).
[214] C. Röger, Y. Miloslavina, D. Brunner, A. R. Holzwarth, and F. Würthner, J. Am. Chem. Soc. **130**, 5929 (2008).
[215] W. Zhang, W. Jin, T. Fukushima, A. Saeki, S. Seki, and T. Aida, Science **334**, 340 (2011).
[216] D. Hellwinkel and M. Melan, Chem. Ber. **104**, 1001 (1971).
[217] D. Hellwinkel and M. Melan, Chem. Ber. **107**, 616 (1974).
[218] S. Wang, M. Kivala, I. Lieberwirth, K. Kirchhoff, X. Feng, W. Pisula, and K. Müllen, ChemPhysChem **12**, 1648 (2011).
[219] M. Bieri, S. Blankenburg, M. Kivala, C. A. Pignedoli, P. Ruffieux, K. Müllen, and R. Fasel, Chem. Commun. **47**, 10239 (2011).
[220] N. S. Makarov, S. Mukhopadhyay, K. Yesudas, J.-L. Brédas, J. W. Perry, A. Pron, M. Kivala, and K. Müllen, J. Phys. Chem. A **116**, 3781 (2012).
[221] K. Do, D. Kim, N. Cho, S. Paek, K. Song, and J. Ko, Org. Lett. **14**, 222 (2011).

[222] S. Paek, N. Cho, S. Cho, J. K. Lee, and J. Ko, Org. Lett. **14**, 6326 (2012).
[223] C. Liu, Y. Li, Y. Zhang, C. Yang, H. Wu, J. Qin, and Y. Cao, Chem. – Eur. J. **18**, 6928 (2012).
[224] Z. Fang, V. Chellappan, R. D. Webster, L. Ke, T. Zhang, B. Liu, and Y.-H. Lai, J. Mater. Chem. **22**, 15397 (2012).
[225] H. Zhang, S. Wang, Y. Li, B. Zhang, C. Du, X. Wan, and Y. Chen, Tetrahedron **65**, 4455 (2009).
[226] M. S. Alexiou, V. Tychopoulos, S. Ghorbanian, J. H. P. Tyman, R. G. Brown, and P. I. Brittain, J. Chem. Soc. Perkin Trans. 2 837 (1990).

List of Publications

Author

1. S. R. Beyer, S. Ullrich, S. Kudera, A. T. Gardiner, R. J. Cogdell and J. Köhler, "Hybrid Nanostructures for Enhanced Light-Harvesting: Plasmon Induced Increase in Fluorescence from Individual Photosynthetic Pigment-Protein Complexes", *Nano Letters*, **11**, 4897-4901 (2011).
2. A. T. Haedler*, S. R. Beyer*, N. Hammer, R. Hildner, M. Kivala, J. Köhler and H.-W. Schmidt, "Synthesis and Photophysical Properties of Multichromophoric Carbonyl-Bridged Triarylamines", *Chemistry - A European Journal*, **20**, 11708-11718 (2014).
3. S. R. Beyer*, L. Müller*, J. Southall, R. J. Cogdell, G. M. Ullmann and J. Köhler, "The Open, the Closed, and the Empty: Time-Resolved Fluorescence Spectroscopy and Computational Analysis of RC-LH1 Complexes from *Rhodopseudomonas palustris*", *The Journal of Physical Chemistry B*, **119**, 1362-1373 (2015)

*) These authors contributed equally to this work

Co-Author (not covered in this thesis)

1. M. Schörner, S. R. Beyer, J. Southall, R. J. Cogdell and J. Köhler, "Multi-Level, Multi-Timescale Fluorescence Intermittency of Photosynthetic LH2 Complexes Revealing Memory Effects in Conformational Switching", *manuscript in preparation*

Acknowledgements

There are a few things that can only be said in your mother tongue…

Ausnahmsweis amol mechert ich gern vom iblichn Schema obweign und na wichdigsdna Leidna zuollererscht dankn: Meina Eldern, maner Schwesder, meina zwa Großmüdder, meina beidn Bodn, meina viln Ongl und Dandn. Schbrich meina riesichn und wunderborn Familie! Ich dank eich fir eiern Righold und eier Underschdüdsung. Fir Ohrn, die immer offn worn – worschd, ob sa himmelhochjauchdsnda Begeisderung oder blanka Wud hern mussdn. Fir oll die aufbauendn und monchmol ah mahnendn Worde. Und fir euer finandsielle Underschdüdsung, die – grod in die ledsden anderdholb Johr – einiches einfocher und manches erschd meeglich gmachd hod. So a zugschdeggder Schein machd fei am Monadsend ganz schee wos aus. Kurzum, ich glaab ned, dass die Dogdorerberd ohne eich endschdand wär. Deswegn bleibt mer eigendlich nur zu sogn: Danke, danke, danke!

And now back to the usual style…

I thank my "Doktorvater" Jürgen Köhler, who offered me the chance to continue exploring the secrets of purple bacteria a few years ago and taught me how to tackle a scientific problem. I also thank my cooperation partners from the workgroups of Richard J. Cogdell, Matthias Ullmann, Hans-Werner Schmidt and Stefan Kudera without whom these projects could not have come into being. Special thanks go to my good friends Lars Müller and Andi Haedler. It is a rare honour to do science with someone you have already known for so long and with whom you have shared an essential part of your way. I enjoyed it. A lot!

Thanks to all the members of EP IV and the GRK1640. It's been a great time with all of you. No matter if you're a pre-grad, a Ph.D.-student a post-doc, part of the technical or organisational staff: You are awesome! May there always be plenty of cake for you

during the coffee breaks. Thanks also, to those at the workgroup, I did the most science with: Mario and Kevin, Abey, Martti and Richard. You all taught me a lot and I had a lot of fun digging through the haystack with you.

Last but not least, I want to thank my friends, my wonderful flatmates and my Taekwondo colleagues (especially Moritz for proof-reading the manuscript). You made the time outside the university really worthwhile. I hope to see you around now and then.

Erklärung

Hiermit erkläre ich, dass ich die vorliegende Arbeit selbstständig verfasst und keine anderen außer die von mir angegebenen Quellen und Hilfsmittel benutzt habe.

Ich erkläre, dass ich keine früheren Promotionsversuche unternommen habe. Die vorgelegte Abhandlung wurde weder in gleicher noch in ähnlicher Form einer anderen Prüfungsbehörde zur Erlangung eines akademischen Grades vorgelegt.

Des Weiteren erkläre ich, dass ich Hilfe von gewerblichen Promotionsberatern bzw. -vermittlern oder ähnlichen Dienstleistern weder in Anspruch genommen habe, noch künftig in Anspruch nehmen werde.

(Erklärungen gemäß der „Promotionsordnung der Bayreuther Graduiertenschule für Mathematik und Naturwissenschaften / Bayreuth Graduate School of Mathematical and Natural Sciences (BayNAT)“ in der Fassung vom 15. Oktober 2009)

Bayreuth, den 23. 4. 2015

Sebastian R. Beyer